AD-769 764

SYNTHESIS OF COMPOUND SEMICONDUCTING MATERIALS AND DEVICE APPLICATIONS

STANFORD UNIVERSITY

PREPARED FOR
ADVANCED RESEARCH PROJECTS AGENCY

JUNE 1973

Final Report

July 1, 1972 - June 30, 1973

Sponsored by
Advanced Research Projects Agency
ARPA Order No. 1644/2

Program Code Number: P2D10

Contractor: Stanford University

Grant No. DAHC15 71-G-6

Principal Investigator: D. A. Stevenson

Co-Investigators:
R. H. Bube
R. S. Feigelson
G. S. Kino
B. L. Mattes
W. D. Nix
R. K. Route
W. A. Tiller

Effective Date of Grant: July 1, 1972

Grant Expiration Date: June 30, 1973

Grant Title: Synthesis of Compound Semiconducting Materials and Device Applications

Center for Materials Research
Stanford University
Stanford, California 94305
(415) 321-2300, Ext. 4118

CMR 73-9

TABLE OF CONTENTS

I.	INTRODUCTION	1
II.	EPITAXIAL CRYSTAL GROWTH	3
III.	DEVICE APPLICATIONS OF GaAs	21
IV.	RELATIONS BETWEEN DISLOCATIONS AND MECHANICAL PROPERTIES AND THE PRODUCTION AND CHARACTERIZATION OF DEFECT STRUCTURES IN COMPOUND SEMICONDUCTORS	33
V.	SCIENTIFIC ASPECTS OF GALLIUM ARSENIDE CRYSTAL PREPARATION	46
VI.	THE SYNTHESIS, CHARACTERIZATION AND DEVICE APPLICATION OF GALLIUM NITRIDE: PREPARATION OF GaN LIGHT-EMITTING DIODES	54

I. Introduction

The present program concerns the synthesis of compound semiconducting materials, with particular emphasis on their use in microwave and acoustic devices. The program is divided into three major sections: thin film epitaxial growth of III-V compounds; the design, fabrication and evaluation of microwave and acoustic devices; and fundamental studies of crystal synthesis and properties.

The devices of primary interest are of the planar microwave and acoustical type, employing thin films of GaAs as the active layer. The choice of GaAs was made based on its unique properties: exceptionally high carrier mobility, a moderately large band gap, the Gunn effect and piezoelectric response. These planar devices require high quality active layers of GaAs, with particularly strict requirements on film thickness, surface smoothness, carrier density, and mobility in the film. The layers intended for microwave devices are grown by the liquid phase epitaxial technique. In addition, a study of electroluminescence in GaN light emitting diodes has evolved as a result of exploratory research on the growth of nitrides, originally undertaken in conjunction with their potential use in microwave devices.

In the period covered by this report, there have been three major activities relating to the materials synthesis and device fabrication: growth of GaAs layers by liquid phase epitaxy, with carrier densities in the 10^{14} - 10^{15} range and 300/77°K mobilities above 7000/50,000, thicknesses in the 0.5μm to 30μm range, and optically smooth surfaces; analysis of the complex exchange reactions in the crystal growth zone, with specific reference to the possible contamination of GaAs layers by

container materials during the growth process; and a study of heteroepitaxial growth of GaAs on oxide substrates. Research on microwave devices has been concerned with the design and evaluation of the following devices: a traveling space charge wave GaAs amplifier; and acoustic devices, including linear acoustic amplifiers and non linear interactions of acoustic waves. The fundamental studies of crystal synthesis and properties have included the following topics: relations between dislocations and mechanical properties and the production and characterization of defect structures in compound semiconductors; analysis of the interfacial parameters that govern the growth of GaAs; and the synthesis and characterization of GaN layers. As mentioned above this last topic has evolved into a study of electroluminescence in this material. A description of progress in these respective areas is given below.

II. EPITAXIAL CRYSTAL GROWTH

R. S. Feigelson, B. L. Mattes, R. K. Route and P. Pettit

A. PROGRAM OBJECTIVE

The objective of the epitaxial crystal growth program was the preparation of high quality, uniform and reproducible epitaxial layers of GaAs for the microwave device applications program. The device program required layers (not obtainable commercially) that have carrier densities in the low 10^{14} cm^{-3} to 10^{15} cm^{-3} range, 300/77°K mobilities above 7000/50,000 cm^2/V-sec, thicknesses in the .5 μm to 30 μm range, and optically smooth surfaces. All of these requirements have been met and recently exceeded by liquid phase epitaxial techniques.

To meet this objective, considerable effort was devoted to the development of new methods of growth, the study of variables that influence growth and purity, techniques to prepare and handle materials involved in growth, and methods to evaluate the growth and its properties. In addition, the epitaxial crystal growth program was coordinated with the materials studies and device applications programs to interact on problems of mutual concern.

The most recent objective of this program was to grow higher purity layers of GaAs by control of chemical reactions within the growth system. In addition, the growth of GaAs on BeO substrates by liquid phase epitaxial techniques was also attempted.

The progress of the epitaxial crystal growth effort, to be discussed below, has met all of the initial and final objectives of the program. However, because of the recent success in improving the purity and overall quality of the GaAs epitaxial layers, further research should be carried

out to develop optimal control on the incorporation of impurities into the growth. In addition, heteroepitaxial growth of GaAs on oxide substrates appears to be possible by liquid phase techniques and should be pursued to develop cheaper materials for solid-state electronic devices.

B. PROGRESS

1. Achievements

During the term of this grant numerous objectives and new developments were achieved in the GaAs epitaxial crystal growth effort. Over 640 GaAs layers have been grown for both growth studies and device applications. The most recent achievements are:

(a) The incorporation of carbon, oxygen and silicon, that form electrically active centers in the layers, has been reproducibly controlled during growth by means of chemical reactions between the graphite growth cell, fused-quartz reactor tube and purified hydrogen to yield low 10^{14} cm^{-3} carrier densities with 8000/80,000 cm^2/V-sec mobilities at 300/77°K.

(b) Reproducible and improved electrical properties have been obtained in layers grown in a reactor system consisting of a high purity alumina tube, pyrolytic boron nitride crucible and purified hydrogen. Similar results have also been obtained when purified argon was used in place of hydrogen in a fused-quartz and graphite system.

(c) Epitaxial layers have been reproducibly grown with nd (carrier density x thickness) products in the low 10^{-11} cm^{-2} range for the traveling-wave Gunn amplifier. The layers had optically smooth surfaces and were uniform in thickness in the 1 μm to 10 μm range.

(d) Heteroepitaxial growths of GaAs on berylium oxide substrates by liquid phase techniques have shown high density nucleation of hillocks on both the prismatic and basal plane orientations. Nucleation of uniform coherent layers appears to be limited by the development of a suitable substrate surface preparation.

(e) Growth studies have shown that surface terraces on all substrate orientations are restricted to the types of hillocks that can be formed with (100) and (111) planes and that growth proceeds by attachment to only (100) surfaces.

Previous achievements in this program are listed below:

(a) A temperature gradient cell, to stabilize the liquid-solid interface during nucleation and growth, has been developed that produces layers with optically smooth surfaces and uniform thicknesses from .2 μm to 50 μm on any substrate orientation.

(b) Substrate preparation and handling procedures have been developed to provide defect free surfaces to grow high quality layers under both hydrogen and argon atmospheres.

(c) A nucleation and growth model has been developed that quantitatively relates the width of surface terraces to a temperature gradient normal to the substrate and the heat of formation.

(d) n^+ contacts have been grown on low carrier density layers to make excellent ohmic contacts.

(e) A method was developed to analyze Schottky barrier measurements for layers on semi-insulating substrates. The method of analysis is applicable to all capacitance voltage measurements, independent of substrate type, layer thickness and carrier density, frequency, and electrode diameter, unless the layer is completely depleted.

This program has demonstrated the potential of the liquid phase method to grow reproducible high quality layers of epitaxial GaAs. The principal contributions to this program arose from detailed studies of the gro process that show (1) a temperature gradient normal to the substrate helps to increase the density of nucleation sites, thus yielding extremely smooth uniformly thick layers; and (2) chemical reactions within the growth system contribute to the amount and type of impurities introduced into the growth and the activation of electrically active centers, thus affecting the carrier density and their mobility in the layer. These results are generally applicable to the growth of most III-V compounds. The details of the growths and the most recent achievements are described below.

2. Substrate Preparation and Handling

Substrate wafers with saw cut surfaces are cemented to a stainless steel plate and chem-mechanically polished.[1] No intermediate mechanical grinding or polishing is used, to prevent further deep structural damage in the substrate. A 20% NaClO solution is slowly siphoned onto a rotating Geoscience "Polytex Supreme" pad. About 2 to 3 mils are removed from both sides of the substrates to insure against saw damage and warpage. When these surfaces are carefully cleaned and handled defect free growths are obtained, except for intrinsic growth morphologies.

To prepare these surfaces for growth, the substrates are cleaned immediately before each growth. The following procedures are used:

(a) Degrease with acetone, trichloroethylene, acetone rinse in a teflon beaker.

(b) Wash with an "Aquet" soaked swab on filter paper and then thoroughly rinse with DI water in teflon beaker.

(c) Manipulate substrate with a quartz tweezer that grasps only the edges and prevents further mechanical contact with the substrate surfaces until it is loaded into the growth cell.

(d) Degrease with acetone, trichloroethylene, acetone, methanol and isopropyl alcohol rinse in quartz beaker.

(e) Boil in concentrated HCl and then rinse in DI water.

(f) Rinse thoroughly in doubly quartz distilled DI water.

(g) Repeat (d).

(h) Boil in isopropyl alcohol.

(i) Drain off hot isopropyl alcohol to leave the substrate dry and ready to load into the growth cell.

This procedure had to be modified for growths made under an argon atmosphere. Apparently the water rinse in (e) and (f) oxidizes the surface and without a hydrogen atmosphere in the growth system the oxide is not reduced. Therefore, by replacing the DI water with methanol in (e) and skipping (f) - (g), suitably cleaned surfaces are obtained. However, care must be taken to keep the substrate completely submerged under solution after the HCl boil to prevent oxidation. This procedure also produces suitably cleaned surfaces for hydrogen atmosphere growths too.

3. Growth Method

The liquid phase epitaxial (LPE) method of growth has met all the requirements for producing reliable high quality GaAs layers. In this program significant modifications were made to the horizontal tilt process, Fig. II-1.[2,3] A high purity graphite cell, Fig. II-2, was developed to induce a temperature gradient normal to the solid-liquid interface during growth. The cell operates in a homogeneous temperature region

in the furnace. The temperature gradient is induced by removing heat from a liquid Ga reservoir underneath the growth cell. The heat is drawn out by forcing He gas through a quartz heat transfer tube immersed in the liquid Ga reservoir. The liquid Ga reservoir serves two purposes: (1) it maintains good thermal contact between the quartz heat transfer tube and the graphite growth cell, and (2) it improves the temperature uniformity over the plane of the growth region. The tilting technique is used to saturate the liquid Ga with As and to roll the As-saturated Ga onto the substrate for growth. The temperature gradient is induced during warm-up to insure that the As-saturated Ga and substrate remain at the same temperature.

The temperature gradient used for most growth conditions was approximately 5°C/cm to 10°C/cm. The furnace was cooled at rates from 300°C/hr to 3000°C/hr, dependent on the saturation temperature and the substrate orientation. For growths below 600°C on (100) substrates the lower cooling rates were used in order to establish good nucleation and growth. The thickness of the epitaxial layer was controlled by the amount of As dissolved in the Ga at the saturation temperature, Fig. II-3. This technique provided layer thickness control from .2 μm at 500°C to 20 μm at 700°C, for a 5g Ga melt and a 1 cm^2 substrate.

4. Chemical Reactions in the Growth System

We have found several new approaches to the control of the sources and incorporation of unwanted impurities and the activation of electrically active centers in the growth of epitaxial GaAs. It is known, and we have found, that the concentration of residual impurities in "high purity" epitaxial GaAs exceeds that of the electrically active centers by 3 to 4

orders of magnitude.[4,5] Materials with 10^{13} cm^{-3} to 10^{15} cm^{-3} net electrically active centers have a total residual impurity content between 10^{17} cm^{-3} and 10^{18} cm^{-3}, as measured by mass spectrometry. The typical residual impurities--carbon, nitrogen, oxygen and silicon--cannot be accounted for on the basis of the 6-9's Ga and As materials or the scrupulously cleaned and leak tight growth systems. These impurities, however, are common to the components of the growth system: (1) carbon--graphite boats and hydrocarbon solvents; (2) nitrogen--exposure to air and system leaks; (3) oxygen--impure hydrogen, leaks and oxides; e.g., Ga_2O and fused quartz; and (4) silicon--fused quartz.

We believe that the source for these impurities can be related to the following series of chemical reactions that occur between fused quartz, graphite and hydrogen above 500°C:

(a) High purity hydrogen reduces fused quartz

$$H_2(g) + SiO_2(s) = SiO(g) + H_2O(g),$$

(b) Water vapor oxidizes graphite

$$H_2O(g) + C(s) = CO(g) + H_2(g),$$

(c) Carbon monoxide reduces silicon monoxide

$$CO(g) + SiO(g) = Si(s) + CO_2(g)$$

(d) Graphite reduces carbon dioxide

$$C(s) + CO_2(g) = 2CO(g),$$

and (e) Liquid Ga dissolves the silicon, and carbon and oxygen from the carbon monoxide. In addition, it is important to note that the kinetics of these reactions can be significantly changed with temperature, time and hydrogen flow rate to change the relative amounts of the gaseous species in the growth region. The total standard free energy change for

the above series of reactions, related to the quilibrium state, is given by

$$G_T^\circ = 117{,}000 - 78.3T, \text{ (cal/mole)}.$$

The actual reactions in the growth system are further compounded by (1) vaporization of Ga_2O and its reaction with fused quartz; (2) sublimation of As from the GaAs substrates; and (3) the diffusion of impurities out of the graphite and fused quartz.

To substantiate reactions between the growth system components and their affect on the electrical properties several changes were made in:

(1) The growth conditions, by varying

(a) Bakeout temperature

(b) Period of bakeout

(c) Saturation temperature

(d) Hydrogen flow rate

(e) Cooling rate

(f) Substrate orientation

and (2) The growth system components, by utilizing

(a) High density and pyrolytic graphite, fused quartz and purified hydrogen

(b) Pyrolytic boron nitride, fused quartz and purified hydrogen

(c) High density graphite, fused quartz and purified argon

(d) Pyrolytic boron nitride, high purity alumina and purified hydrogen.

Before these changes were made, two horizontal tilt growth systems were thoroughly cleaned and He-leak checked to better than 10^{-12} atm-cc/sec. Each system had a separate hydrogen purifier. Under identical growth

conditions and system components, as described above, layers with very nearly the same electrical properties were obtained. Therefore, with confidence in the overall integrity and operation of the growth systems, the above changes were systematically made.

The period of bakeout and the bakeout temperature of the growth system containing the GaAs source and Ga melt made the most significant changes in the electrical properties, as shown in Fig. II-4 and Table II-4. The saturation temperature had a similar effect; however, its effect appears to be equivalent to a short term bakeout, Fig. II-5 and Table II-2. For bakeout temperatures at and above 750°C the layers became p-type irrespective of the saturation temperature. However, for lower temperature bakeouts and saturation temperatures above 750°C, n-type layers were obtained, but above 800°C they also became p-type. The changes in electrical properties with a change in growth conditions were recoverable if the source and melt were given an extended bakeout of several days for bakeout temperatures below 650°C, and 15 hours at 800°C. Without a bakeout in between each growth, the properties of the layers were generally degraded after two or three runs, Growth Nos. 520-528, Table II-2. Improved properties could again be obtained with an extended bakeout. It should be noted that melt-back of the substrate surface was not permitted, in order to insure that impurities were not added to the melt via the substrate. For a continuous series of growths at one bakeout and saturation temperature, the electrical properties asymptotically improved, generally leveling off after 100 hours of accumulated bakeout time, Fig. II-4(a). Once the properties have remained relatively constant, an increased saturation temperature will increase the number of acceptors, N_A, Fig. II-4(b). The hydrogen flow rate was held at .6 l/min for most

of the growths. However for lower flow rates the electrical properties were generally degraded, Table II-2. The cooling rate in general had no discernable effect on the electrical properties unless the surface features indicated poor nucleation on the substrate. However, if the melt had an accumulated bakeout time greater than 100 hours, slower cooling rates tended to improve the mobility and lower the compensation, Growth No. 612 from Table II-4.

From this study on growth condition changes, a marked change in electrical properties is observed between growths on (111)B and (100) substrate surfaces, Fig. II-5 and Table I-1. Layers on (111)B substrates have 5 times the carrier density in the range 10^{15} cm^{-3} compared to layers on (100) substrates grown from the same melt under identical conditions. In addition, the compensation between donors and acceptors is considerably larger for the (100) orientation, Table II-1. It remains to be determined, however, whether the total residual impurity density in the layer is the same for both orientations or whether these impurities are partially excluded by segregation at the liquid-solid interface. There are two possibilities for this behavior: (1) the activation of impurities to electrically active centers is related to the difference in the bonding or attachment at the liquid-solid interface for different orientations; and (2) the decreased segregation of impurities is related to a higher growth velocity in the [100] direction, respectively. Since a similar behavior is observed in epitaxial vapor phase growths, the former is probably correct. Thus there is also a strong correlation between the kinetics of the growth process and the concentration of electrically active impurities.

Analytically, the changes in growth conditions can be correlated with the degree of completion of each of the above reactions. The net reaction, allowing for completion under equilibrium, is given by

$$SiO_2(s) + 2C(s) = Si(s) + 2CO(g)$$
$$\rightarrow Si(1 \text{ in } Ga) + 2C(1 \text{ in } Ga)$$
$$+ 2O(1 \text{ in } Ga).$$

Note that hydrogen does not enter explicitly in this reaction. For varying hydrogen flows, the equilibrium for reaction (a) may not be achieved and/or $H_2O(g)$, $CO(g)$, $SiO(g)$ and $CO_2(g)$ may be physically depleted in the reaction region of the growth system where C, O and Si would be introduced into the Ga melt. Indeed, for growth cells covered with a lid, slower recovery periods for bakeouts and/or lower total ionized impurity densities, $N_A + N_D$, appear to be obtained. For a vapor system, one might also infer that the effect of the $AsCl_3$ mole fraction on total ionized impurity density may be similarly related since this fraction is dependent on the H_2 flow rate.[6]

To definitively establish the above reactions, further research is required to measure the reactant products in the growth system under the above growth conditions. This could be achieved with a time-of-flight or residual gas mass spectrometer. A detailed study of these reactions would lead to optimal growth conditions to reduce sources of impurities and their incorporation into the growth. In addition, when the background of residual impurities is reduced several orders of magnitude, identification of the electrically active centers by photoluminescence and other techniques would be possible. Eventually, with more stringent device requirements, the total background impurities will have to be

reduced since it is the dissociation of electrically inactive impurity complexes that create problems when the layers have to be annealed for electrical contacts and ion implantation.

To eliminate and/or reduce the above reactants, less ractive components in the growth system were used. The properties obtained from these changes are shown in Tables II-3, II-5 and II-6. When graphite was eliminated from the fused quartz and hydrogen growth system and pyrolytic BN was used instead, the compensation ratio, N_A/N_D, was reduced 10% to 20% and the electrical property dependence on bakeout and saturation temperatures was considerably less than that shown in Fig. II-5. However, with these changes in system components, time did not permit a systematic study of changes in growth conditions. When purified argon (argon passed through Ti sponge at 850°C) was used in a graphite and fused quartz system in place of hydrogen, impressive improvements were observed in the mobilities, 9000/105,000 cm^2/V-sec at 300/77°K, Table II-5. When high purity alumina (99.8%) and pyrolytic BN were used with hydrogen in a growth system, eliminating graphite and fused quartz, even better electrical properties were obtained. In this system, initial growths with new Ga and GaAs source gave 77°K mobilities in excess of 80,000 cm^2/V-sec, Table II-6. However, on subsequent growths after a 700°C bakeout for 15 hours, the layers became p-type and had to be back doped with Sn to become n-type. Considerably more research is required on the component changes in the growth system to establish the ultimate electrical properties that can be achieved. Another observation of note is that these component changes led to better layer property reproducibility. Hence, lowering the reactivity of the growth system components and the subsequent improvements in electrical properties lends further credence to the

possibility that graphite, fused quartz and hydrogen do indeed react to introduce impurities into the growth at temperatures ranging from 500°C to 850°C.

5. Electrical Property Evaluation

The carrier density and mobility of each layer were evaluated by the van der Pauw technique at 300°K and 77°K. To form electrical contacts, four indium dots were pressed onto the layer's edge in the general form of a square array, and then the layer was annealed at 400°C for 4 min under vacuum. Any nonohmic behavior in the contacts generally indicated a p-type layer or surface states. Exceptionally large f-factors in the van der Pauw measurements not accounted for by the electrode geometry, indicated a nonuniform carrier density in the layer. Point contact diodes were also used to supplement these observations.

Schottky barriers were used to determine the carrier density profile through the thickness of the layer. In an early phase of this program a Schottky barrier analysis technique was developed for measurements made on layers grown on semi-insulating substrates. The technique involves an extrapolation of the total measured capacitance to determine the effective shunt capacitance, C_0, across the barrier at an infinite reverse bias. Utilizing C_0 to determine the actual barrier capacitance gave excellent agreement with the van der Pauw carrier density determination. The technique, however, can also be used for layers on n^+ substrates. The value of C_0 is exceptionally large for thin layers, low frequencies, large diameter barrier electrodes and high carrier densities. The reason for this anomaly is still not understood. It is presently believed to be related to capacitive effects of surface states that may predominate over

the actual shunt capacitance with the above conditions.

To determine the acceptor and donor carrier densities given in this report, the free carrier density, $n \sim N_D - N_A$, and mobility at 77°K were compared against the theoretical calculations of Rode and Knight.[7] Their theoretical data for a single level center have been extrapolated and replotted to show the Hall mobility as a function of compensation, N_A/N_D, for fixed carrier densities, Fig. II-6. The general experimental data of Wolfe and many others appear to consistently give a fixed compensation between .5 to .9.[6,8] This indicates to us that there is a very high level of background impurities, both active and inactive electrically, in epitaxial GaAs layers that effectively limits the mobilities of the carriers.

6. Nucleation, Hillocks and Surface Terraces

Extensive observations made on over 640 growths have shown a consistent set of epitaxial growth morphologies that are uniquely related to the substrate orientation. The basic observations are:

(1) Nucleation hillocks or individually nucleated growths on the substrate, obtained by decanting the Ga melt off the substrate during growth, form a regular array that parallels the surface terraces.

(2) Only (100) and (111) planes are exposed on hillocks and surface terraces during growth for all substrate orientations.

(3) In general one (100) plane per nucleation hillock advances very rapidly on the substrate plane. The remaining (100) planes are pinned by (111) planes and/or by themselves along <100> edge directions.

(4) Surface terraces are formed by nucleation hillocks that grow essentially along the plane of the substrate either by extending in one direction and then joining with others or in two directions to form platelets that grow together and then overlap.

(5) All coherent epitaxial layers have surfaces made up of parallel linear terraces provided the substrate surface is defect free and flat and the layer is grown under a uniformly thick Ga melt with only a temperature gradient normal to the surface.

(6) Exaggerated hillock formations appear to be only formed wher the substrate surface is (a) oxidized or stained, (b) structurally damaged or (c) grown under extreme nonequilibrium conditions.

Based on observations (1) and (5), a model for terrace growth was previously proposed that relates the terrace width or separation, Δx, to a thermal fluctuation, ΔT, by

$$\Delta x = -\Delta T/(G - S),$$

where G is the temperature gradient normal to the interface and S is determined by the amount of supercooling as the interface advances along the liquidus curve.[2] The thermal fluctuation is due to the heat of formation from a nucleation hillock spread over a diffuse liquid-solid interface region. Nucleation hillocks that form between neighboring hillocks spaced Δx apart will be melted back. Since growth proceeds essentially in one direction, by (3) and (4), random nucleation hillocks will coalesce into long chains, determined by the substrate orientation.

The common types of surface terraces observed are shown in Figs. II-7 - II-10. The terrace orientations are related to the orientation of the substrate and the type of nucleation hillock that can form. Typical hillocks observed on these orientations are also shown. The shift in terrace orientation is also demonstrated in Figs. II-7 and II-9 as the substrate is rotated about [100], [110] and [112] directions for the (100) and (111) principal planes. Experimentally, the orientations of the substrates could be determined to within 0.5°. With this error of uncertainty, all layers exhibited a consistent terrace type and orientation with respect to the substrate orientation.

From these observations, it is speculated that the (111) plane is actually made up of (100) planes interlocked on [100] edges, Fig. II-11(a). This would account for the lower growth velocities in the [111] directions and the curvelinear surfaces that can be generated in many other directions. Preliminary electron microscope replicas show that there is considerable structure on curvelinear and (111) planes as compared to (100) planes for both hillocks and terraces, Fig. II-11(b). It should be noted that considerable surface detail is blanketed under a 20Å to 40Å oxide layer. However, there is a remarkable similarity between Figs. II-11(a) and II-11(b).

The conclusion that the (100) plane is the principal plane for atomic attachment during growth is based totally on observation. Independently, theoretical calculations have shown that the (100) plane possesses the highest interfacial liquid-solid energy density.[9] Therefore, atomic attachment to the (100) interface will tend to minimize this energy by exposing a (111) surface that possesses the lowest liquid-solid interfacial energy.

Misleading interpretations on directional growth velocities can be drawn from one-dimensional velocities simply averaged normal to the substrate. There are obvious discrepancies between these observations and vapor phase epitaxial (VPE) growths.[10] However, in VPE one must consider the vapor-solid interfacial energy density which may differ from that of the liquid-solid interface. But it is interesting to note that VPE surface "textures" are observed and that some of the surface "textures" strongly resemble LPE nucleation hillocks and terraces.[6,10,11]

7. Heteroepitaxial Growth of GaAs on BeO Substrates

Heteroepitaxial layers of GaAs on BeO substrates would be of great technological interest because of the extremely high thermal conductivity, optical transparency and electrical insulation BeO provides. Since the nucleation of GaAs on an oxidized surface is difficult to initiate and control by standard LPE techniques, the heteroepitaxial growth of GaAs on BeO appeared to be possible by our temperature gradient liquid phase method where nucleation can be more easily controlled. Growths were first attempted on the faceted faces of synthetically grown BeO. Nucleation appeared to be limited to peripheral areas where the As-saturated Ga melt would contact the BeO surface, Fig. II-11(a). To overcome this problem several fluxes--Sn, In, Bi, and Al--were added to the Ga to help wet the BeO surface. None of these fluxes appeared to help except fo a small amount of Al, less than 1 % by volume. A rough saw cut surface on the BeO was then tried without a flux. In this case spontaneous nucleation resulted, Fig. II-11(b).

There appears to be some preferential ordering of the hillocks in Fig. II-11(a). It is of interest to note that all of the hillocks formed are bounded by (100) and (111) planes, similar to the results observed

for uniform nucleation on GaAs substrates. Since some ordering and spontaneous nucleation on BeO has now been demonstrated by LPE techniques, further research on substrate orientations and surface preparation may allow the growth of uniform coherent heteroepitaxial layers of GaAs on this material.

REFERENCES

II-1. Final Report, "Synthesis of Compound Semiconducting Materials and Device Applications", AD-727 803, ARPA Contract No. DAHC15-70-G-12, Stanford University, July 1, 1970-June 30, 1971.

II-2. Final Report, "Synthesis of Compound Semiconducting Materials and Device Applications", AD-746 882, ARPA Contract No. DAHC15-71-G-9, Stanford University, July 1, 1971-June 30, 1972.

II-3. B. L. Mattes and R. K. Route, J. Crystal Growth 16, 219 (1972).

II-4. C. M. Wolfe, G. E. Stillman and E. B. Owens, J. Electrochem. Soc. 117, 129 (1970).

II-5. Semi-Annual Technical Report, "Synthesis of Compound Semiconducting Materials and Device Applications", AD-755 947, ARPA Contract No. DAHC15-72-G-6, Stanford University, July 1, 1972-December 31, 1972.

II-6. J. V. DiLorenzo, J. Crystal Growth 17, 189 (1972).

II-7. D. L. Rode and S. Knight, Phys. Rev. B3, 2534 (1971).

II-8. C. M. Wolfe and G. E. Stillman, Proc. 1970 Symp. on GaAs, Aachen, Germany, p. 3.

II-9. Hyo-Sup Kim, "Solid-Liquid Interfaces in the Ga-As System", Ph.D. Thesis, Dept. Materials Science, Stanford University, SU-DMS-73-T-45, March, 1973.

II-10. D. W. Shaw, Proc. 1968 Symp. on GaAs, Dallas, Texas, p. 50.

II-11. D. W. Shaw, J. Crystal Growth 12, 249 (1972).

FIGURE CAPTIONS

Figure II-1. Horizontal tilt system with temperature gradient cell in place.

Figure II-2. Details of the temperature gradient cell.

Figure II-3. Epitaxial layer thickness as a function of the saturation temperature. The atom fraction of As required to saturate liquid Ga (after Hall) is used to calculate the layer thickness assuming that all the GaAs comes out of solution onto the substrate.

Figure II-4. The effect of accumulated bakeout time of the growth system and Ga and GaAs source on free carrier density, n, donor density, N_D, acceptor density, N_A, and total carrier density, N_D+N_A, for Growth Nos. 597-618. The bakeout and saturation temperatures, cooling rates, etc., are given in Table II-4.

Figure II-5. The effect of saturation temperature on the free carrier density, n, and total carrier density, N_D+N_A, for growths on (100) and (111)B substrate orientations, Growth Nos. 477-513 in Table II-1. Note that N_D+N_A increases sharply at 800°C and that above this temperature the layers become p-type for both orientations.

Figure II-6. The free carrier mobility vs. compensation, N_A/N_D, for fixed free carrier densities at 77°K. These curves were extrapolated from the theoretical results of Rode and Knight.

Figure II-7. Schematic orientation relationships between nucleation hillocks and substrates rotated about a [100] axis. The shaded and unshaded hillock surfaces are (100) and (111) planes, respectively. The orientation of surface terraces parallel these hillocks as illustrated in (b). For slight misorientations, as illustrated by (c), the terrace will change direction by an angle γ, given by $\tan \gamma = \tan \beta / \tan \alpha$.

Figure II-8. Characteristic nucleation hillocks and surface terraces observed on (100) substrates, (a) and (b), and (110) substrates, (c). The hillocks and terraces are principally bounded by (100) and (111) planes. The angles correspond to the schematic orientations of the substrates shown in Fig. II-7. The terrace orientations shown are for a (100) plane rotated (a) slightly about a [110] axis, (b) slightly about a [100] axis and (c) 45° about a [100] axis.

Figure II-9. Schematic orientation relationships between nucleation hillocks and substrates rotated about a $[\bar{1}10]$ axis. The

shaded and unshaded hillock surfaces are (100) and (111) planes, respectively. The nucleation hillocks in (a), (b) and (d) parallel the (100) and the (110) prismatic hillocks. For a rotation about a [$\bar{1}\bar{1}$2] axis, (c), the nucleation hillocks coalesce together into extended platelets along that axis.

Figure II-10. Characteristic nucleation hillocks and surface terraces observed on (a) (i13), (b) and (c) (111), and (d) (122) oriented substrates. The hillocks and terraces are principally bounded by (100) and (111) planes. The hillocks and terraces correspond to the schematic orientations of the substrates shown in Fig. II-9. The terrace orientations shown are for a (111) plane rotated (a) about a [110] axis to a (1i3) plane, (b) slightly about a [112] axis and (d) about a [110] axis to a (122) plane.

Figure II-11. (a) A (111) plane made up of (100) planes interlocked on [100] edges. (b) An electron micrograph of a replica taken from a terrace edge for a growth on a (111)B substrate, Growth No. 39. Details of the actual terrace edge are blanketed by a 20Å to 40Å oxide layer. Note the remarkable similarity between the shaded (100) planes in (a) and the protruding planes in (b).

Figure II-12. Heteroepitaxial growths of LPE GaAs on BeO substrates. (a) Nucleated hillocks oriented about a region wetted by the Ga melt on an As grown prismatic surface. (b) Spontaneous nucleation of hillocks on a rough saw-cut basal surface.

TABLE II-1

EPITAXIAL GaAs GROWTH CONDITIONS AND PROPERTIES FROM A GRAPHITE, FUSED QUARTZ AND HYDROGEN SYSTEM

(STARTED WITH NEW Ga AND GaAs SOURCE; USED NO TEMPERATURE GRADIENT)

GROWTH NO. (CONSECUTIVE GROWTHS)	SUBSTRATE ORIENTATION	BAKEOUT TEMP. (PERIOD) / SATURATION TEMP. (COOLING RATE) {°C(hr)/°C(°C/sec)}	HYDROGEN FLOW RATE (ℓ/min)	MOBILITY @ 77°K (cm^2/V-sec)	CARRIER DENSITY @ 77°K (cm^{-3})	$\frac{N_A}{N_D}$ @ 77°K	$N_D + N_A$ @ 77°K (cm^{-3})	THICKNESS (μm)
477	(111)B	628(42)/628(.44)	0.5	12,600	1.1×10^{16}	.58	4.1×10^{16}	8.9
478	(111)B	628(17)/628(.54)	0.4	21,400	4.7×10^{15}	.58	1.8×10^{16}	8.1
480	(111)B	628(16)/628(.77)	0.4	16,000	8.2×10^{15}	.55	2.8×10^{16}	7.0
481	(111)B	600(16)/776(.31)	0.4	23,500	4.1×10^{15}	.60	1.6×10^{16}	47
485	(111)B	600(88)/778(.28)	0.4	32,600	2.6×10^{15}	.59	1.0×10^{16}	44
490	(111)B	600(16)/725(.42)	0.4	29,300	3.3×10^{15}	.58	1.2×10^{16}	25
491	(111)B	600(16)/805(.18)	0.4	26,300	3.1×10^{15}	.63	1.4×10^{16}	44
493	(111)B	600(64)/794(.11)	0.4	29,500	1.3×10^{15}	.75	9.1×10^{15}	50
496	(100)	600(17)/800(.53)	0.4	42,100	9.6×10^{14}	.72	5.9×10^{15}	48
497	(111)B	600(16)/796(.52)	0.4	32,300	1.6×10^{15}	.70	9.1×10^{15}	51
499	(100)	600(15)/800(.10)	0.4	47,500	2.0×10^{14}	.89	3.4×10^{15}	70
501	(111)B	600(15)/775(1.0)	0.4	27,000	2.6×10^{15}	.65	1.2×10^{16}	22
504	(100)	600(66)/799(.37)	0.4	51,300	3.4×10^{14}	.83	3.7×10^{15}	68
505	(100)	600(16)/784(.23)	0.4	59,700	4.0×10^{14}	.76	2.9×10^{15}	47
507	(100)	600(16)/693(.25)	0.4	43,300	8.4×10^{14}	.73	5.4×10^{15}	15
509	(100)	600(16)/797(.16)	0.4	49,700	5.8×10^{14}	.75	4.1×10^{15}	58
511	(100)	None/745(.20)	0.4	56,800	5.1×10^{14}	.73	3.3×10^{15}	47
513	(100)	None/633(.15)	0.4	28,000	1.9×10^{15}	.71	1.1×10^{16}	7.5

TABLE VI-2

EPITAXIAL GaAs GROWTH CONDITIONS AND PROPERTIES FROM A GRAPHITE, FUSED QUARTZ AND HYDROGEN SYSTEM

(STARTED WITH NEW Ga AND GaAs SOURCE; USED NO TEMPERATURE GRADIENT)

GROWTH NO. (CONSECUTIVE GROWTHS)	SUBSTRATE ORIENTATION	BAKEOUT TEMP. (PERIOD) / SATURATION TEMP. (COOLING RATE) {°C(hr)/°C(°C/sec)}	HYDROGEN FLOW RATE (ℓ/min)	MOBILITIES @ 300/77°K (cm^2/V-sec)	CARRIER DENSITIES @ 300/77°K (cm^{-3})	$\frac{N_A}{N_D}$ @ 77°K	$N_D + N_A$ @ 77°K (cm^{-3})	THICKNESS (μm)
518	(100)	None/797(.22)	0.4	7,150/38,700	$1.8/1.5 \times 10^{15}$	.65	7.1×10^{15}	73
520	(100)	756(1)/797(.26)	0.4	7,730/47,300	$11/9.2 \times 10^{14}$	.69	5.0×10^{15}	82
522	(100)	585(1)/797(.22)	0.4	7,600/45,700	$11/9.3 \times 10^{14}$	.70	5.3×10^{15}	64
525	(100)	585(1)/840(.38)	0.4	7,460/40,200	$7.4/5.8 \times 10^{14}$	.81	5.5×10^{15}	72
526	(100)	585(1)/836(.71)	0.4	7,100/39,300	$6.0/4.9 \times 10^{14}$	.81	5.3×10^{15}	64
528	(100)	585(1)/633(.54)	0.4	5,550/33,100	$3.1/2.7 \times 10^{15}$	.56	9.6×10^{15}	3.6
531	(100)	585(18)/797(.26)	0.4	6,670/46,600	$6.0/4.0 \times 10^{14}$	.83	4.3×10^{15}	46
532	(100)	585(65)/793(.29)	0.4	8,910/57,200	$2.3/2.0 \times 10^{14}$	.86	2.7×10^{15}	40
536	(100)	585(17)/798(.38)	0.8	7,540/58,500	$1.9/1.6 \times 10^{14}$	.88	2.5×10^{15}	41
537	(100)	585(17)/763(.37)	0.8	8,470/65,200	$1.9/1.7 \times 10^{14}$	.85	2.1×10^{15}	26
539	(100)	585(42)/796(.31)	0.8	-/65,000	$-/1.3 \times 10^{14}$	.89	2.2×10^{15}	35
541	(100)	585(89)/797(.33)	0.1	5,860/41,900	$4.3/3.5 \times 10^{14}$	.87	5.0×10^{15}	38
542	(100)	585(2) /789(.36)	0.1	6,500/38,900	$11/9.2 \times 10^{14}$	.75	6.4×10^{15}	32
543	(100)	647(16)/796(.45)	0.5	7,430/54,100	$2.7/2.4 \times 10^{14}$	.85	3.0×10^{15}	37
544	(100)	647(17)/797(.36)	0.5	8,380/60,000	$1.7/1.6 \times 10^{14}$	.88	2.5×10^{15}	29
545	(100)	585(27)+695(38)/797(.33)	0.5	P - TYPE		-	-	36

TABLE II-2 (CONTINUED)

EPITAXIAL GaAs GROWTH CONDITIONS AND PROPERTIES FROM A GRAPHITE, FUSED QUARTZ AND HYDROGEN SYSTEM
(STARTED WITH NEW Ga AND GaAs SOURCE; USED NO TEMPERATURE GRADIENT)

GROWTH NO. (CONSECUTIVE GROWTHS)	SUBSTRATE ORIENTATION	BAKEOUT TEMP. (PERIOD) / SATURATION TEMP. (COOLING RATE) [°C(hr)/°C(°C/sec)]	HYDROGEN FLOW RATE (ℓ/min)	MOBILITIES @ 300/77°K (cm^2/V-sec)	CARRIER DENSITIES @ 300/77°K (cm^{-3})	$\frac{N_A}{N_D}$ @ 77°K	$N_D + N_A$ @ 77°K (cm^{-3})	THICKNESS (μm)
546	(100)	694(15)/797(.40)	0.5	P -	TYPE	-	-	-1
548	(100)	578(17)/797(.29)	0.5	P -	TYPE	-	-	38
549	(111)B	577(18)/797(.33)	0.5	6,870/44,300	$3.7/3.0 \times 10^{14}$	.87	4.3×10^{15}	45
551	(111)B	695(16)/800(.33)	0.5	6,700/40,000	$2.3/1.8 \times 10^{14}$	.92	4.3×10^{15}	52
Added 5-9's Sn to melt								
552	(100)	695(28)/798(.45)	0.5	8,250/46,200	$5.4/4.7 \times 10^{14}$	.80	4.2×10^{15}	44
553	(100)	696(18)/797(.19)	0.5	8,210/47,800	$4.1/3.5 \times 10^{14}$	.84	4.0×10^{15}	46
555	(100)	796(18)/798(.32)	0.5	7,470/38,600	$4.2/3.3 \times 10^{14}$	.89	5.7×10^{15}	53
556	(100)	796(18)/799(.43)	0.5	P -	TYPE	-	-	59
558	(100)	689(16)/698(.23)	0.5	5,970/40,300	$3.3/2.8 \times 10^{14}$	.89	4.8×10^{15}	12
559	(100)	696(54)/800(.22)	0.5	6,270/34,700	$2.0/1.4 \times 10^{14}$	.95	5.5×10^{15}	56

TABLE II-3

EPITAXIAL GaAs GROWTH CONDITIONS AND PROPERTIES FROM A PYROLYTIC BORON NITRIDE, FUSED QUARTZ AND HYDROGEN SYSTEM
(STARTED WITH NEW Ga AND GaAs SOURCE; USED NO TEMPERATURE GRADIENT)

GROWTH NO. (CONSECUTIVE GROWTHS)	SUBSTRATE ORIENTATION	BAKEOUT TEMP. (PERIOD) / SATURATION TEMP. (COOLING RATE) [°C(hr)/°C(°C/sec)]	HYDROGEN FLOW RATE (ℓ/min)	MOBILITIES @ 300/77°K (cm^2/V-sec)	CARRIER DENSITIES @ 300/77°K (cm^{-3})	N_A / N_D @ 77°K	$N_D + N_A$ @ 77°K (cm^{-3})	THICKNESS (μm)
560	(100)	796(18)/587(.24)	0.5	1290/11,200	$9.2/10 \times 10^{14}$	.94	3.2×10^{16}	2.7
561	(100)	583(64)/799(.36)	0.5	6690/49,600	$1.8/1.6 \times 10^{15}$	.55	5.5×10^{15}	26
562	(100)	582(16)/692(.26)	0.5	7740/77,200	$2.6/2.6 \times 10^{14}$	.75	1.8×10^{15}	13
563	(100)	584(16)/702(.45)	0.5	6900/85,300	$1.8/2.0 \times 10^{14}$	.76	1.4×10^{15}	16
564	(100)	584(16)/749(.22)	0.5	8600/79,900	$2.9/2.9 \times 10^{14}$	.66	1.4×10^{15}	30
565	(100)	None/751(.31)	0.5	8360/81,400	$3.6/3.4 \times 10^{14}$	.68	1.8×10^{15}	30
New Ga and GaAs Source								
566	(100)	583(65)/746(.26)	0.5	6450/47,100	$1.6/1.4 \times 10^{15}$	.59	5.4×10^{15}	26
567	(100)	584(17)/745(.42)	0.5	7060/55,200	$11/9.4 \times 10^{14}$	.63	4.1×10^{15}	21
568	(100)	699(17)/750(.33)	0.5	8040/81,000	$1.8/1.7 \times 10^{14}$	.81	1.6×10^{15}	32
Boron Nitride boat with above Ga and GaAs source transferred to another fused quartz and hydrogen system								
569	(100)	700(16)/753(.08)	0.4	6800/78,000	$8.2/6.3 \times 10^{13}$	.92	1.5×10^{15}	34
570	(100)	700(16)/756(.13)	0.5	P - TYPE		-	-	28
571	(100)	600(64)/757(.12)	0.5	8050/87,500	$8.2/8.5 \times 10^{13}$	.87	1.2×10^{15}	26
572	(110)	600(16)/738(.13)	0.5	COARSE HILLOCKS				26
573	(100)	600(22)/759(.14)	0.5	7000/81,000	$5.6/5.5 \times 10^{13}$	.93	1.5×10^{15}	31
574	(100)	600(63)/711(.14)	0.5	6320/92,000	$3.0/1.9 \times 10^{14}$	.74	1.3×10^{15}	14
575	(110)	600(15)/711(.14)	0.5	COARSE HILLOCKS				18
576	(100)	600(15)/711(.12)	0.5	6700/66,500	$5.8/5.2 \times 10^{14}$	.68	2.7×10^{15}	14

TABLE II-4

EPITAXIAL GaAs GROWTH CONDITIONS AND PROPERTIES FROM A GRAPHITE, FUSED QUARTZ AND HYDROGEN SYSTEM
(STARTED WITH NEW Ga AND GaAs SOURCE; USED A 5°C/CM TEMPERATURE GRADIENT)

GROWTH NO. (CONSECUTIVE GROWTHS)	SUBSTRATE ORIENTATION	BAKEOUT TEMP. (PERIOD) / SATURATION TEMP. (COOLING RATE) {°C(hr)/°C(°C/sec)}	HYDROGEN FLOW RATE (l/min)	MOBILITIES @ 300/77°K (cm^2/V-sec)	CARRIER DENSITIES @ 300/77°K (cm^{-3})	$\frac{N_A}{N_D}$ @ 77°K	$N_D + N_A$ @ 77°K (cm^{-3})	THICKNESS (μm)
597	(100)	595(16)/751(.16)	0.6	6,280/23,100	4.8/4.3 x 10^{15}	.58	1.6 x 10^{16}	31
598	(100)	595(17)/751(.36)	0.6	7,060/35,800	2.2/1.8 x 10^{15}	.63	7.9 x 10^{15}	27
600	(100)	594(65)/752(.45)	0.6	7,690/45,600	12/8.7 x 10^{14}	.71	5.1 x 10^{15}	23
601	(100)	593(17)/750(.29)	0.6	7,070/44,200	8.5/7.6 x 10^{14}	.75	5.3 x 10^{15}	29
603	(100)	593(18)/741(.33)	0.6	7,430/49,500	8.3/7.0 x 10^{14}	.72	4.3 x 10^{15}	21
604	(100)	594(18)/579(.23)	0.6	DEPLETED	LAYER	-	-	0.9
605	(100)	595(18)/701(.30)	0.6	4,950/42,900	5.9/7.9 x 10^{14}	.75	5.5 x 10^{15}	3.0
607	(100)	595(18)/622(.34)	0.6	7,160/42,500	2.2/2.1 x 10^{15}	.53	6.7 x 10^{15}	3.3
609	(110)	594(18)/755(.17)	0.6	7,810/46,200	1.9/1.7 x 10^{15}	.54	5.7 x 10^{15}	20
610	(100)	666(17)/753(.38)	0.6	7,150/41,100	12/9.3 x 10^{14}	.73	6.0 x 10^{15}	25
611	(100)	595(66)/619(.30)	0.6	- /41,600	- /6.3 x 10^{14}	.78	5.1 x 10^{15}	2.9
612	(100)	595(15)/635(.15)	0.6	8,570/80,000	3.3/5.0 x 10^{14}	.59	1.9 x 10^{15}	4.8
614	(100)	593(18)/649(.35)	0.6	4,930/43,300	7.5/8.1 x 10^{14}	.74	5.4 x 10^{15}	6.3
615	(100)	666(16)/649(.23)	0.6	- /71,100	- /3.1 x 10^{14}	.75	2.2 x 10^{15}	6.9
616	(100)	664(16)/649(.23)	0.6	6,500/71,400	3.1/3.1 x 10^{14}	.75	2.2 x 10^{15}	6.5
618	(100)	665(88)/650(.26)	0.6	7,580/61,400	3.2/5.9 x 10^{14}	.67	4.3 x 10^{15}	5.4

TABLE II-5

EPITAXIAL GaAs GROWTH CONDITIONS AND PROPERTIES FROM A GRAPHITE, FUSED QUARTZ AND ARGON SYSTEM
(STARTED WITH Ga AND GaAs SOURCE FROM GROWTH NO. 618, TABLE II-4;
USED A 5°C/CM TEMPERATURE GRADIENT)

GROWTH NO. (CONSECUTIVE GROWTHS)	SUBSTRATE ORIENTATION	BAKEOUT TEMP. (PERIOD) / SATURATION TEMP. (COOLING RATE) {°C(hr)/°C(°C/sec)}	ARGON FLOW RATE (ℓ/min)	MOBILITIES @ 300/77°K (cm^2/V-sec)	CARRIER DENSITIES @ 300/77°K (cm^{-3})	$\frac{N_A}{N_D}$ @ 77°K	$N_D + N_A$ @ 77°K (cm^{-3})	THICKNESS (μm)
619	(100)	666(17)/649(.16)	0.7	-/27,000	-/3.5 x 10^{14}	.93	9.6 x 10^{15}	7.1
621	(100)	666(18)/649(.17)	0.7	6,700/37,000	1.9/1.6 x 10^{15}	.65	7.4 x 10^{15}	6.2
622	(100)	667(20)/723(.36)	0.7	7,030/37,500	1.8/1.5 x 10^{15}	.65	7.1 x 10^{15}	13
623	(100)	712(63)/726(.45)	0.7	8,020/50,900	1.4/1.2 x 10^{15}	.63	5.2 x 10^{15}	15
624	(100)	715(16)/722(.31)	0.7	6,300/40,700	1.5/1.2 x 10^{15}	.69	6.6 x 10^{15}	17
625	(100)	774(16)/721(.26)	0.7	8,800/67,300	8.2/7.0 x 10^{14}	.60	2.8 x 10^{15}	13
627	(100)	774(16)/747(.53)	0.7	7,080/54,800	9.1/7.7 x 10^{14}	.68	4.0 x 10^{15}	14
629	(100)	826(18)/723(.20)	0.7	3,430/105,000	1.7/1.4 x 10^{14}	.76	1.0 x 10^{15}	15
631	(100)	715(1)/721(.28)	0.7	9,130/68,700	3.4/3.2 x 10^{14}	.53	1.0 x 10^{15}	15
632	(100)	715(1)/723(.32)	0.7	8,300/67,000	5.2/5.6 x 10^{14}	.65	2.6 x 10^{15}	18

TABLE II-6

EPITAXIAL GaAs GROWTH CONDITIONS AND PROPERTIES FROM A PYROLYTIC BORON NITRIDE, 99.8% ALUMINA AND HYDROGEN SYSTEM
(STARTED WITH Ga AND GaAs SOURCE FROM GROWTH NO. 576, TABLE II-3; USED NO TEMPERATURE GRADIENT)

GROWTH NO. (CONSECUTIVE GROWTHS)	SUBSTRATE ORIENTATION	BAKEOUT TEMP. (PERIOD) / SATURATION TEMP. (COOLING RATE) [°C(hr)/°C(°C/sec)]	HYDROGEN FLOW RATE BAKEOUT / SATURATION (ℓ/min)	MOBILITIES @ 300/77°K (cm^2/V-sec)	CARRIER DENSITIES @ 300/77°K (cm^{-3})	$\frac{N_A}{N_D}$ @ 77°K	$N_D + N_A$ @ 77°K (cm^{-3})	THICKNESS (μm)
585	(100)	700(19)/700(.03)	.01/.8	P - TYPE	-	-		19
New Ga and GaAs source								
589	(100)	700(15)/700(.03)	.02/.8	6,950/75,000	$2.1/1.9 \times 10^{14}$	.80	1.7×10^{15}	22
593	(100)	700(63)/700(.03)	.03/.8	P - TYPE	-	-		26
596	(100)	600(15)/700(.03)	.2/.8	P - TYPE	-	-		17
Added 6-9's Sn to melt								
599	(100)	600(15)/700(.03)	.2/.8	5,420/45,800	$5.6/4.6 \times 10^{14}$	.82	4.6×10^{15}	20
602	(100)	600(15)/700(.03)	.8/.8	2,090/27,600	$10/4.0 \times 10^{14}$	.92	9.6×10^{15}	19
606	(100)	600(39)/700(.03)	.8/.3	4,130/30,800	$4.5/4.8 \times 10^{14}$	.89	8.2×10^{15}	22
608	(100)	700(18)/700(.03)	.8/.8	4,830/33,200	$2.9/2.2 \times 10^{14}$	.93	6.1×10^{15}	15
613	(100)	700(15)/700(.03)	.8/.6	5,280/46,500	$2.5/2.2 \times 10^{14}$	.89	3.8×10^{15}	20
617	(100)	700(15)/700(.03)	.8/.8	3,660/33,000	$2.9/3.0 \times 10^{14}$	.92	7.2×10^{15}	19
New Ga and GaAs source								
620	(100)	700(15)/700(.03)	.4/.8	9,300/89,800	$2.2/2.2 \times 10^{14}$	.73	1.4×10^{15}	16
626	(100)	700(48)/700(.03)	.4/.8	3,450/27,400	$8.9/7.6 \times 10^{14}$	.86	1.0×10^{16}	20
628	(100)	700(15)/700(.03)	.6/.1	P - TYPE	-	-		18
630	(100)	None/700(.03)	-/.8	P - TYPE	-	-		19
Added 6-9's Sn to melt								
633	(100)	700(15)/700(.03)	.8/.8	P - TYPE	-	-		20

TABLE II-6 (CONTINUED)

EPITAXIAL GaAs GROWTH CONDITIONS AND PROPERTIES FROM A PYROLYTIC BORON NITRIDE, 99.8% ALUMINA AND HYDROGEN SYSTEM

(STARTED WITH Ga AND GaAs SOURCE FROM GROWTH NO. 576, TABLE II-3; USED NO TEMPERATURE GRADIENT)

GROWTH NO. (CONSECUTIVE GROWTHS)	SUBSTRATE ORIENTATION	BAKEOUT TEMP. (PERIOD) / SATURATION TEMP. (COOLING RATE) [°C(hr)/°C(°C/sec)]	HYDROGEN FLOW RATE BAKEOUT / SATURATION (ℓ/min)	MOBILITIES @ 300/77°K (cm^2/V-sec)	CARRIER DENSITIES @ 300/77°K (cm^{-3})	$\frac{N_A}{N_D}$ @ 77°K	$N_D + N_A$ @ 77°K (cm^{-3})	THICKNESS (μm)
Added more Sn to melt								
635	(100)	700(15)/700(.03)	.8/.8	-/45,000	-/1.0 x 10^{14}	.96	4.9 x 10^{15}	15
637	(100)	700(63)/700(.03)	.6/.8	P - TYPE		-	-	22
Added more Sn to melt								
640	(100)	700(19)/700(.03)	.8/.9	P - TYPE		-	-	18
641	(100)	700(15)/700(.03)	.8/.8	4,820/62,400	1.8/1.8 x 10^{14}	.85	2.2 x 10^{15}	18
643	(100)	700(15)/700(.04)	.6/.8	P - TYPE		-	-	16

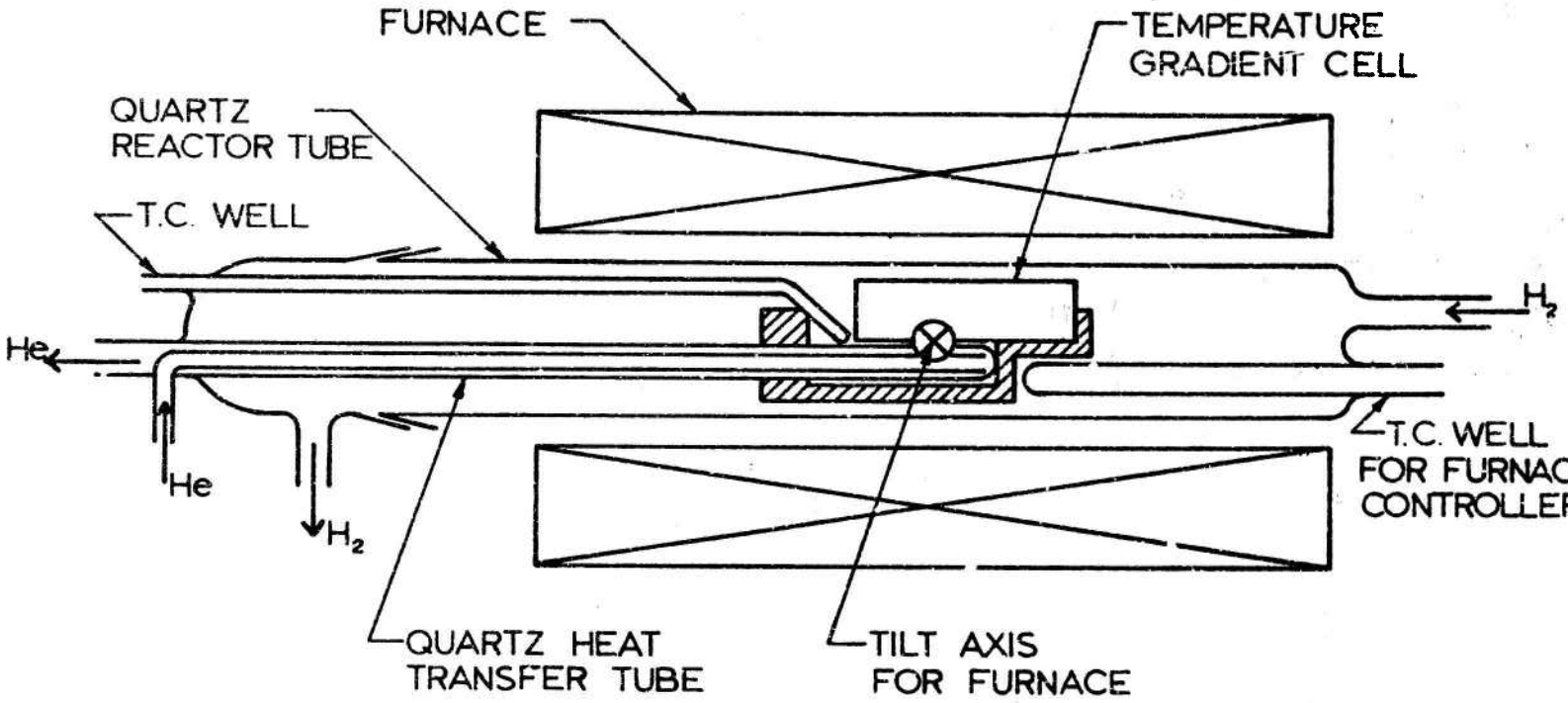

Figure II-1. Horizontal tilt system with temperature gradient cell.

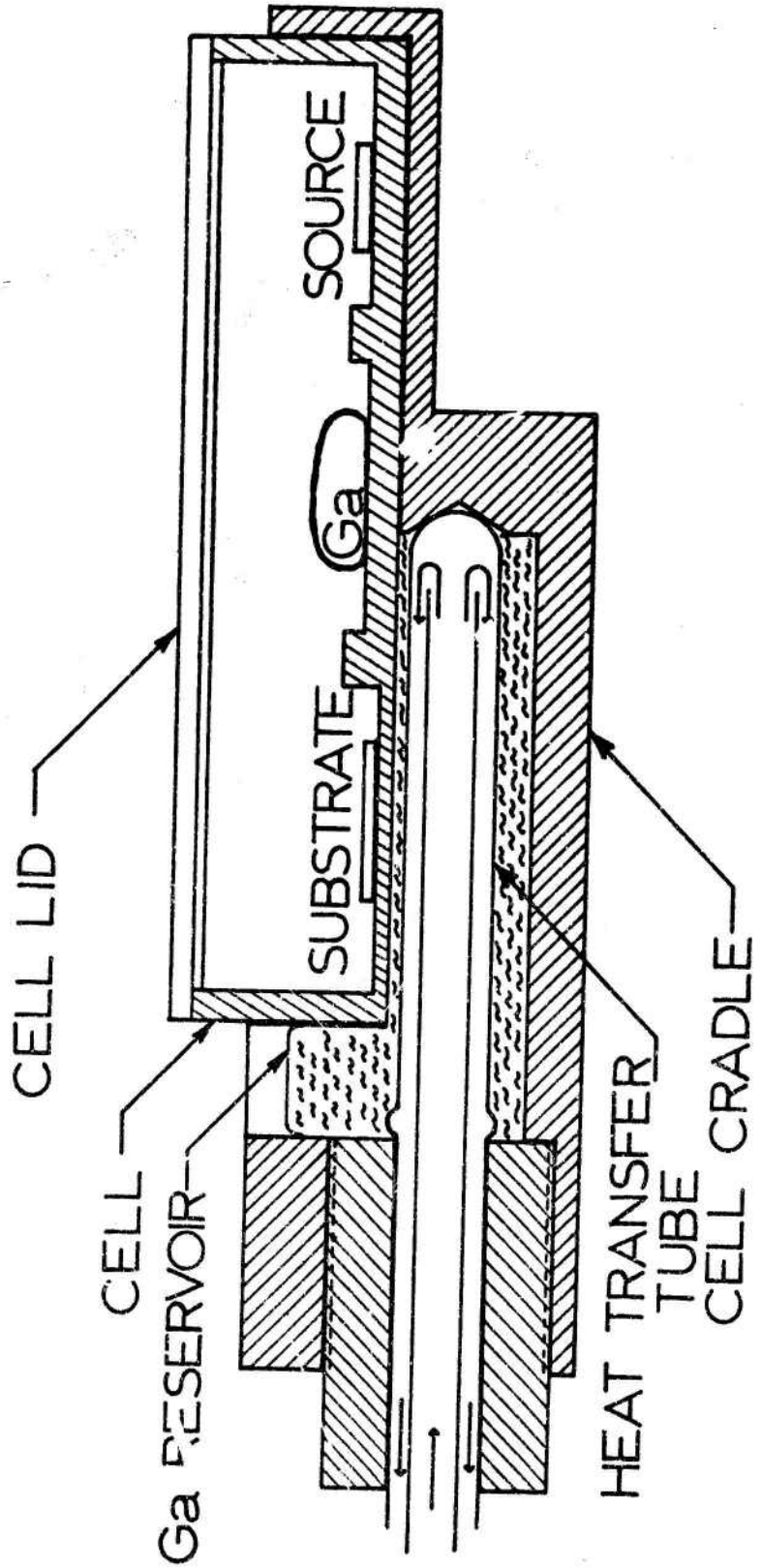

Figure II-2. Details of the temperature gradient cell.

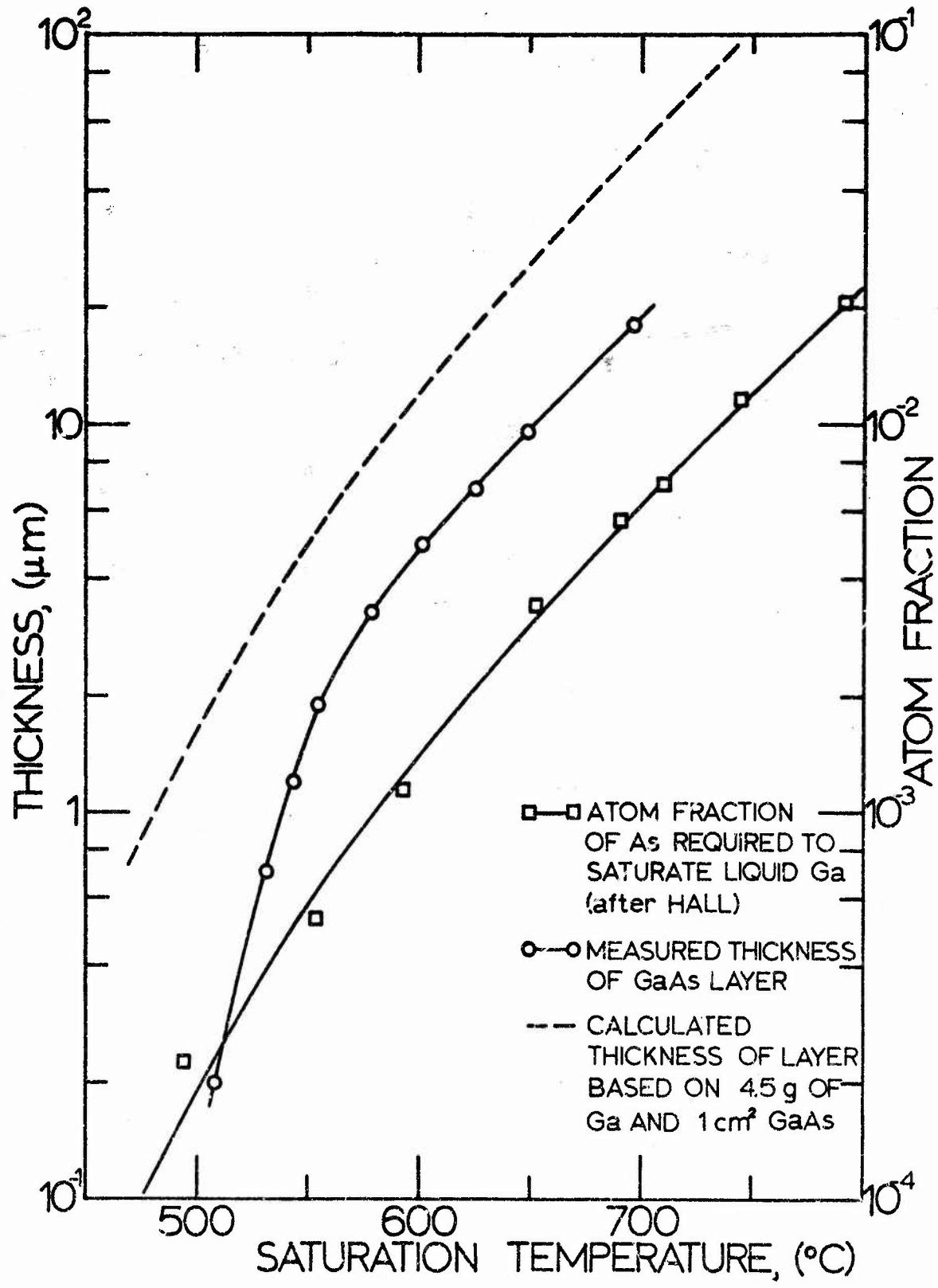

Figure II-3. Epitaxial layer thickness as a function of the saturation temperature. The atom fraction of As required to saturate liquid Ga (after Hall) is used to calculate the layer thickness assuming that all GaAs comes out of solution on to the substrate.

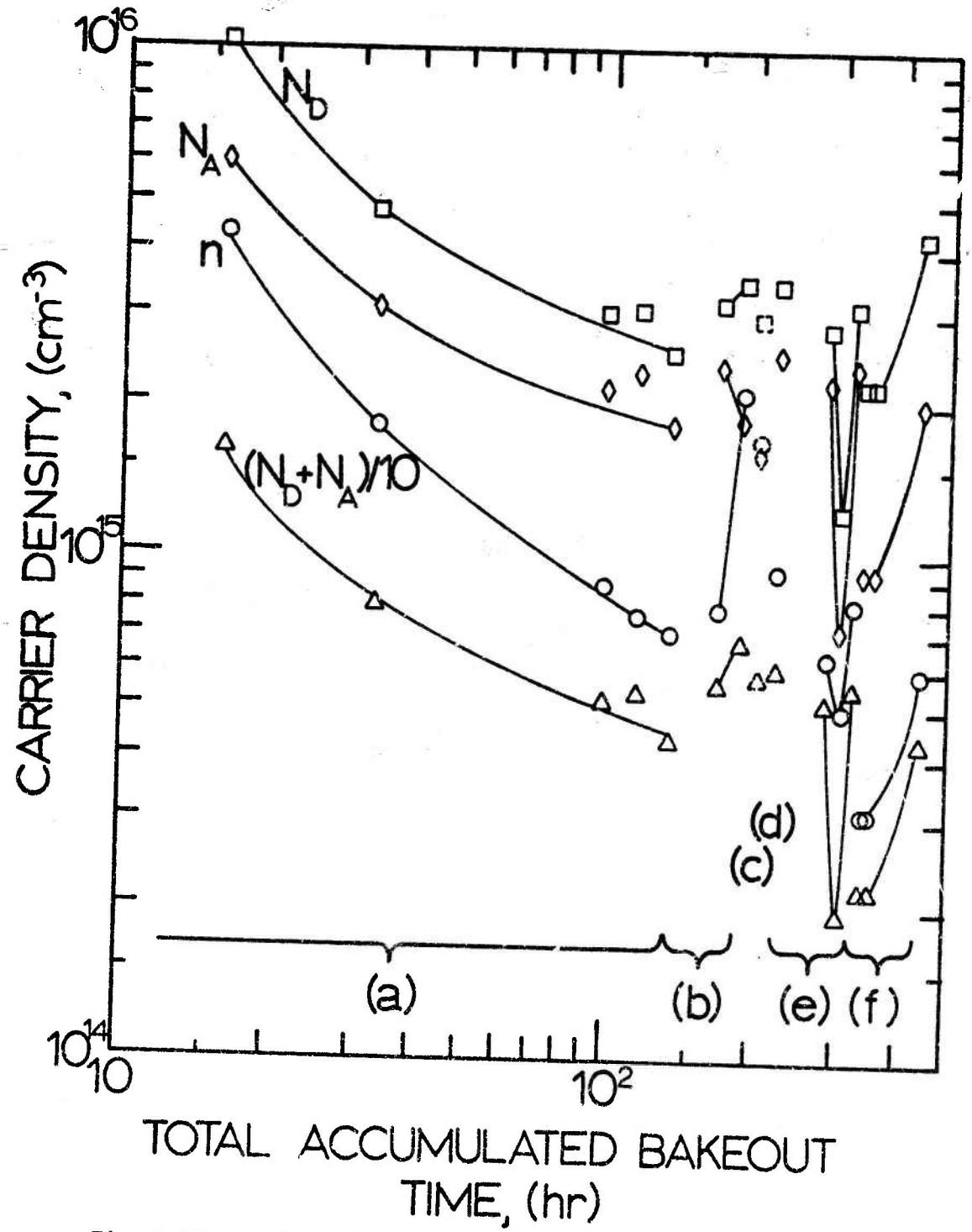

Figure II-4. The effect of accumulated bakeout time of the growth system and Ga and GaAs source on free carrier density, n, donor density, N_D, acceptor density, N_A, and total carrier density, N_D+N_A, for Growth Nos. 597-618. The bakeout and saturation temperatures, cooling rates, etc. are given in Table II-4.

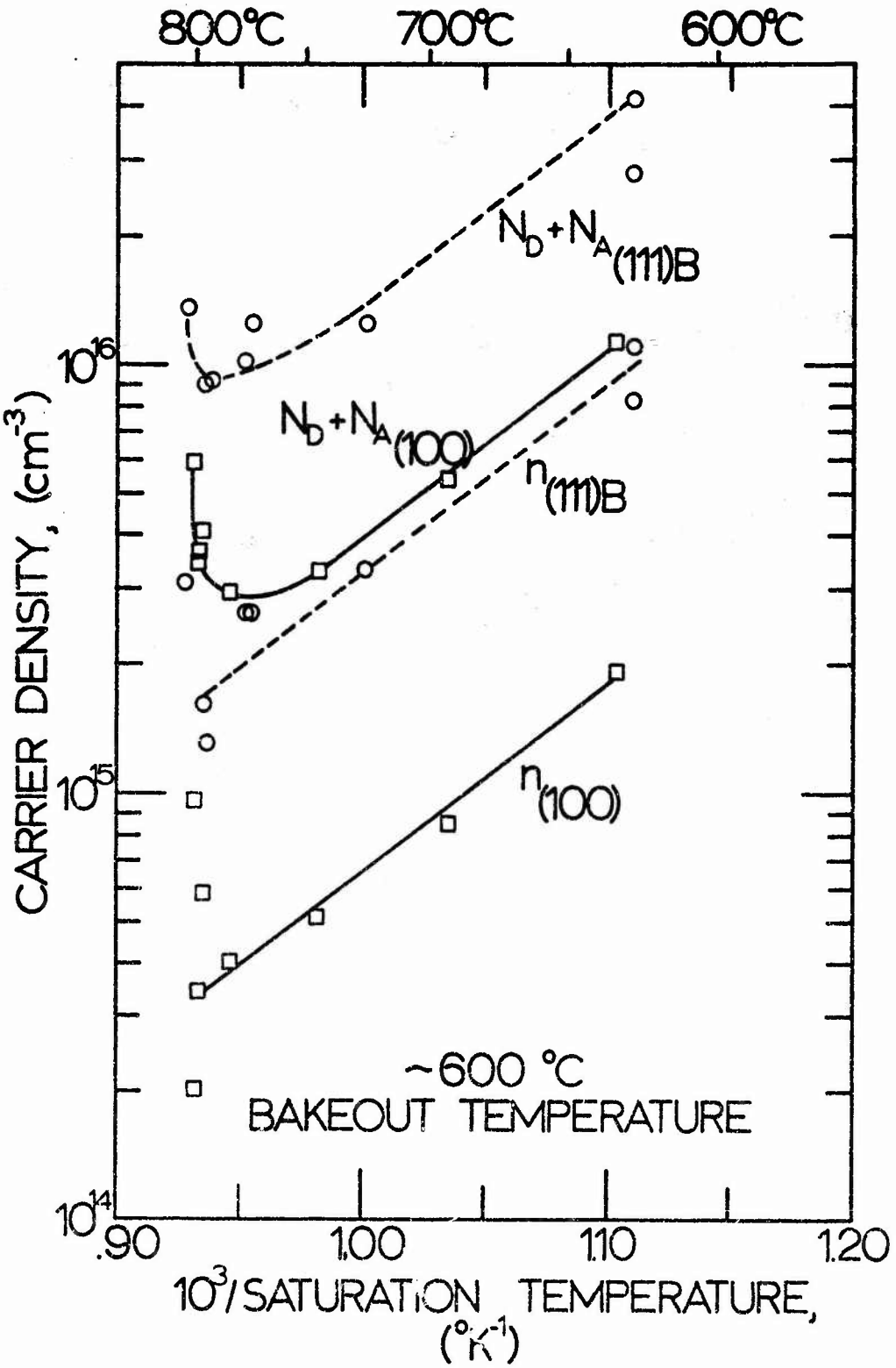

Figure II-5. The effect of saturation temperature on the free carrier density, n, and total carrier density, N_D+N_A, for growths on (100) and (111)B substrate orientations, Growth Nos. 477-513 in Table II-1. Note that N_D+N_A increases sharply at 800°C and that above this temperature the layers become p-type for both orientations

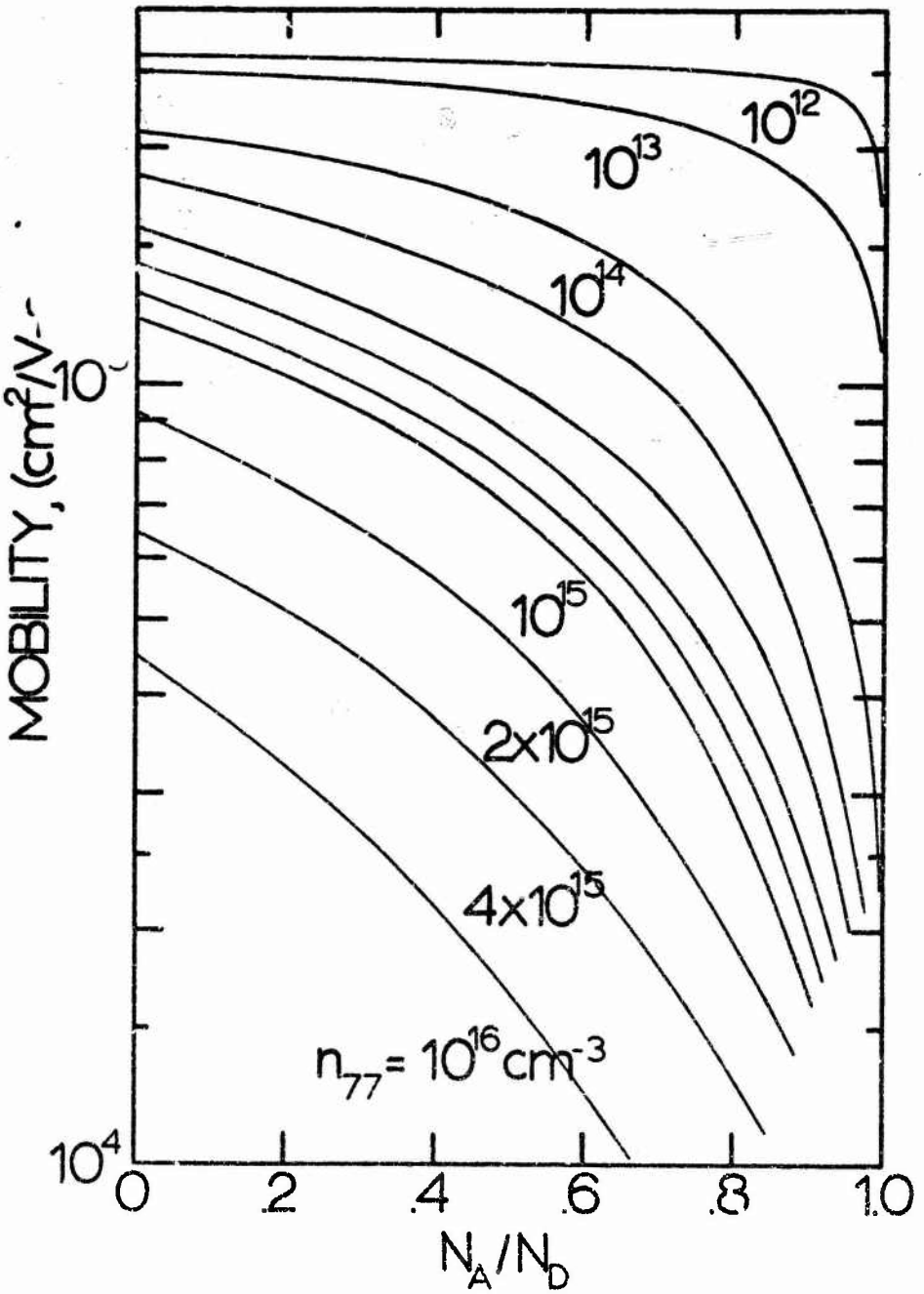

Figure II-6. The free carrier mobility vs. compensation, N_A/N_D, for fixed free carrier densities at 77°K. These curves were extrapolated from the theoretical results of Rode and Knight.

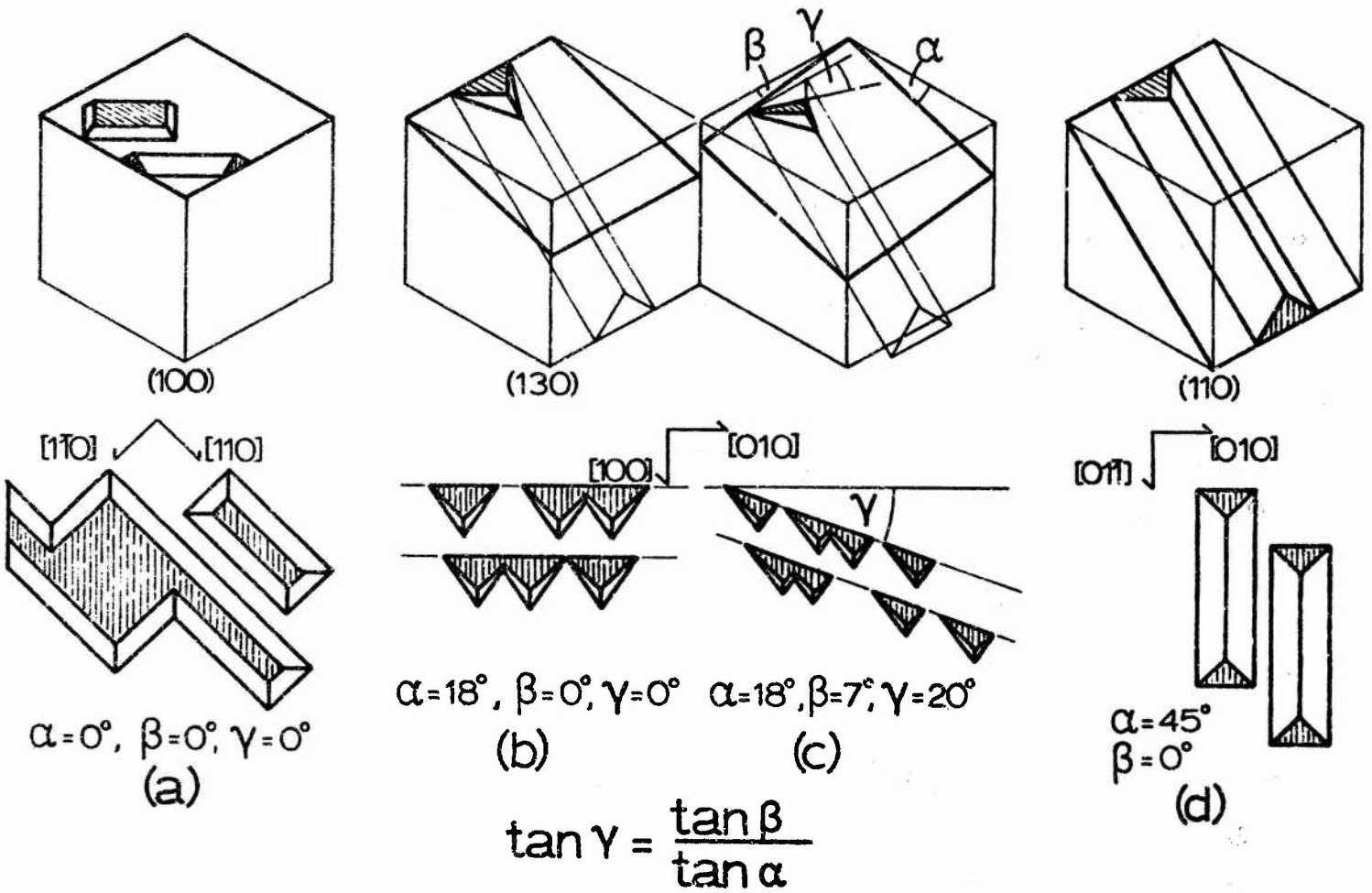

Figure II-7. Schematic orientation relationships between nucleation hillocks and substrates rotated about a [100] axis. The shaded and unshaded hillock surfaces are (100) and (111) planes, respectively. The orientation of surface terraces parallel these hillocks as illustrated in (b). For slight misorientations, as illustrated by (c), the terraces will change direction by an angle γ, given by $\tan\gamma = \tan\beta/\tan\alpha$.

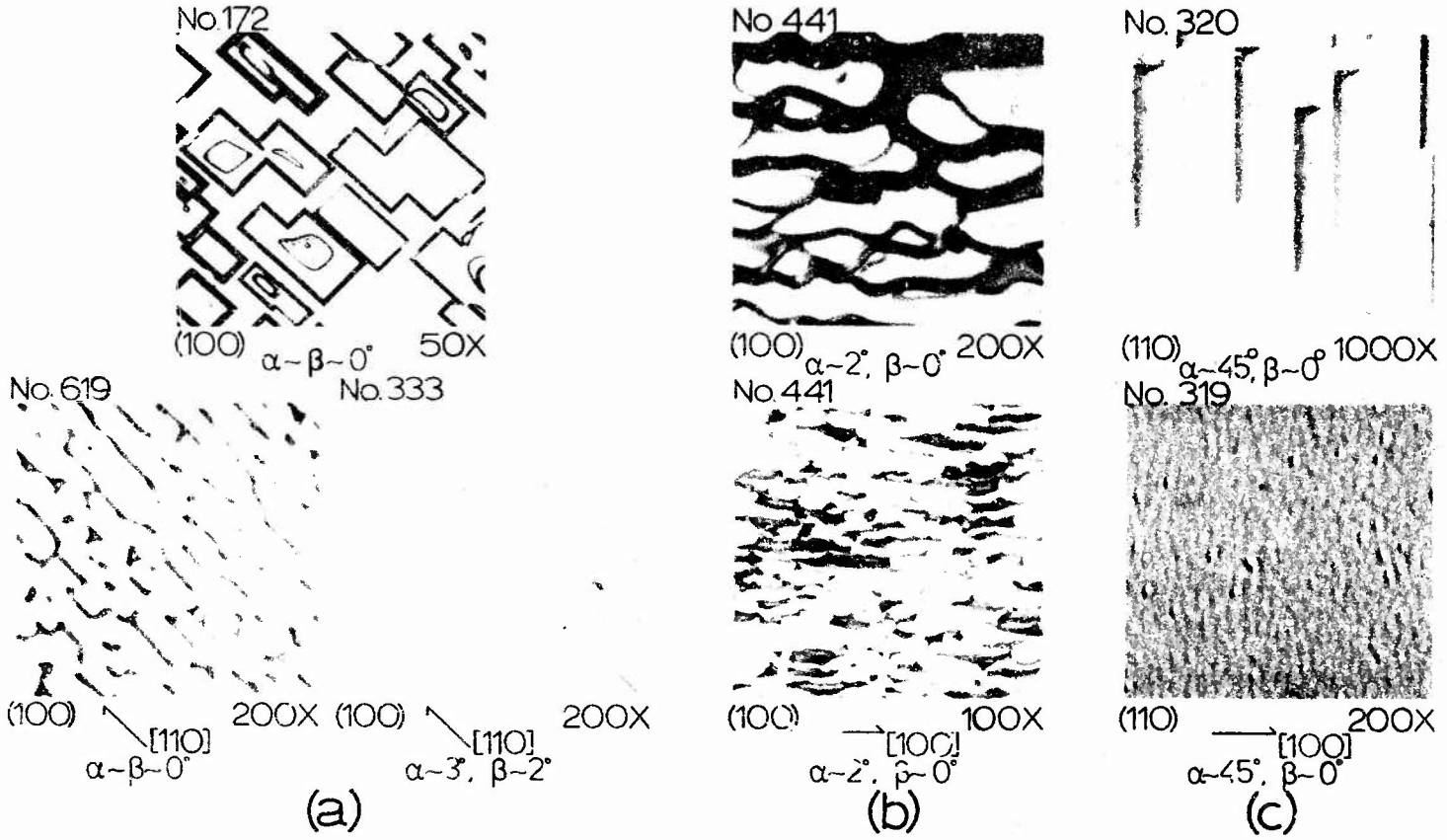

Figure II-8. Characteristic nucleation hillocks and surface terraces observed on (100) substrates, (a) and (b), and (110) substrates, (c). The hillocks and terraces are principally bounded by (100) and (111) planes. The angles correspond to the schematic orientations of the substrates shown in Fig. II-7. The terrace orientations shown are for a (100) plane rotated (a) slightly about a [110] axis, (b) slightly about a [100] axis and (c) 45° about a [100] axis.

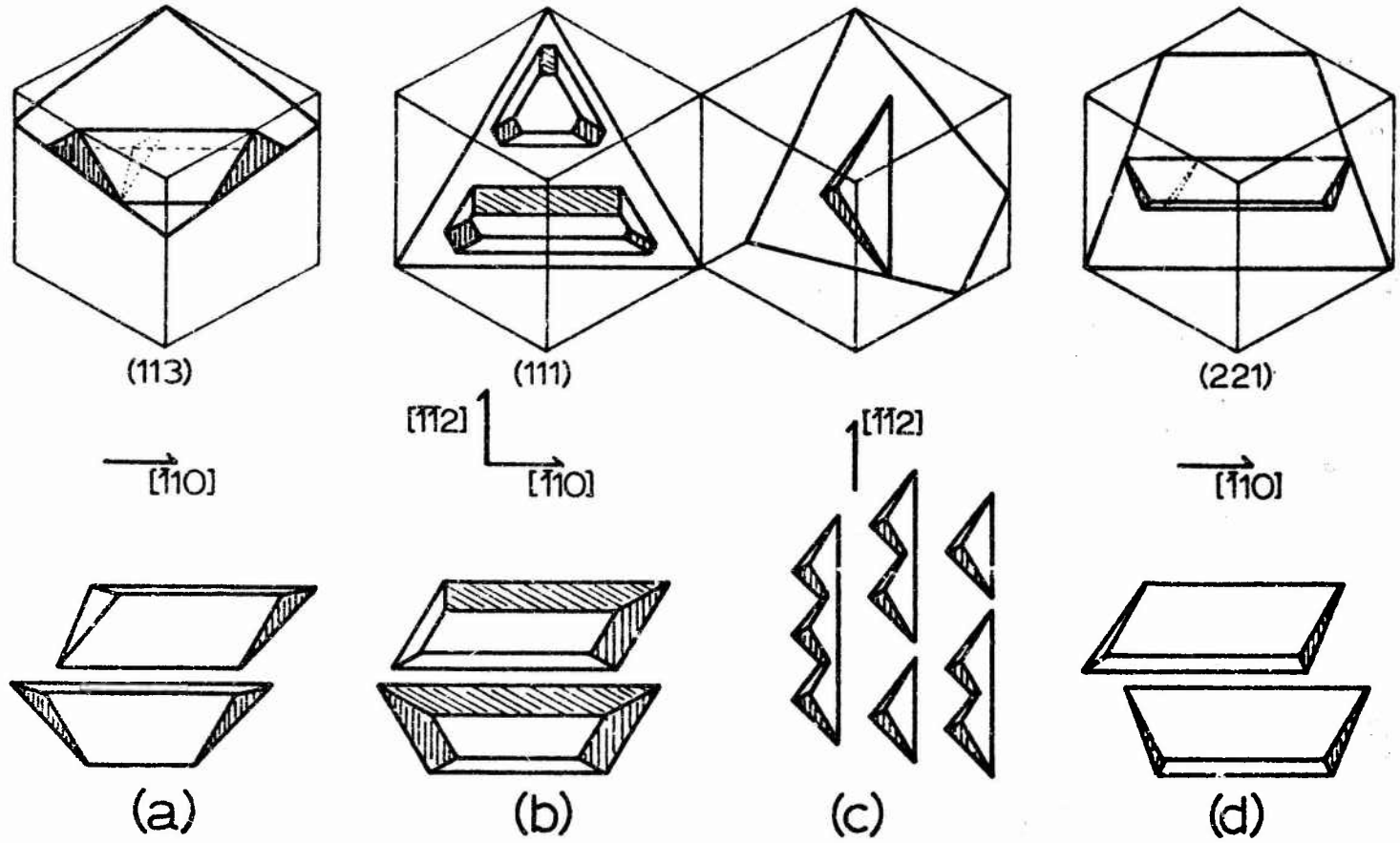

Figure II-9. Schematic orientation relationships between nucleation hillocks and substrates rotated about a [110] axis. The shaded and unshaded hillock surfaces are (100) and (111) planes, respectively. The nucleation hillocks in (a), (b) and (d) parallel the (100) and the (110) prismatic hillocks. For a rotation about a [$\bar{1}\bar{1}$2] axis, (c), the nucleation hillocks coalesce together into extended platelets along that axis.

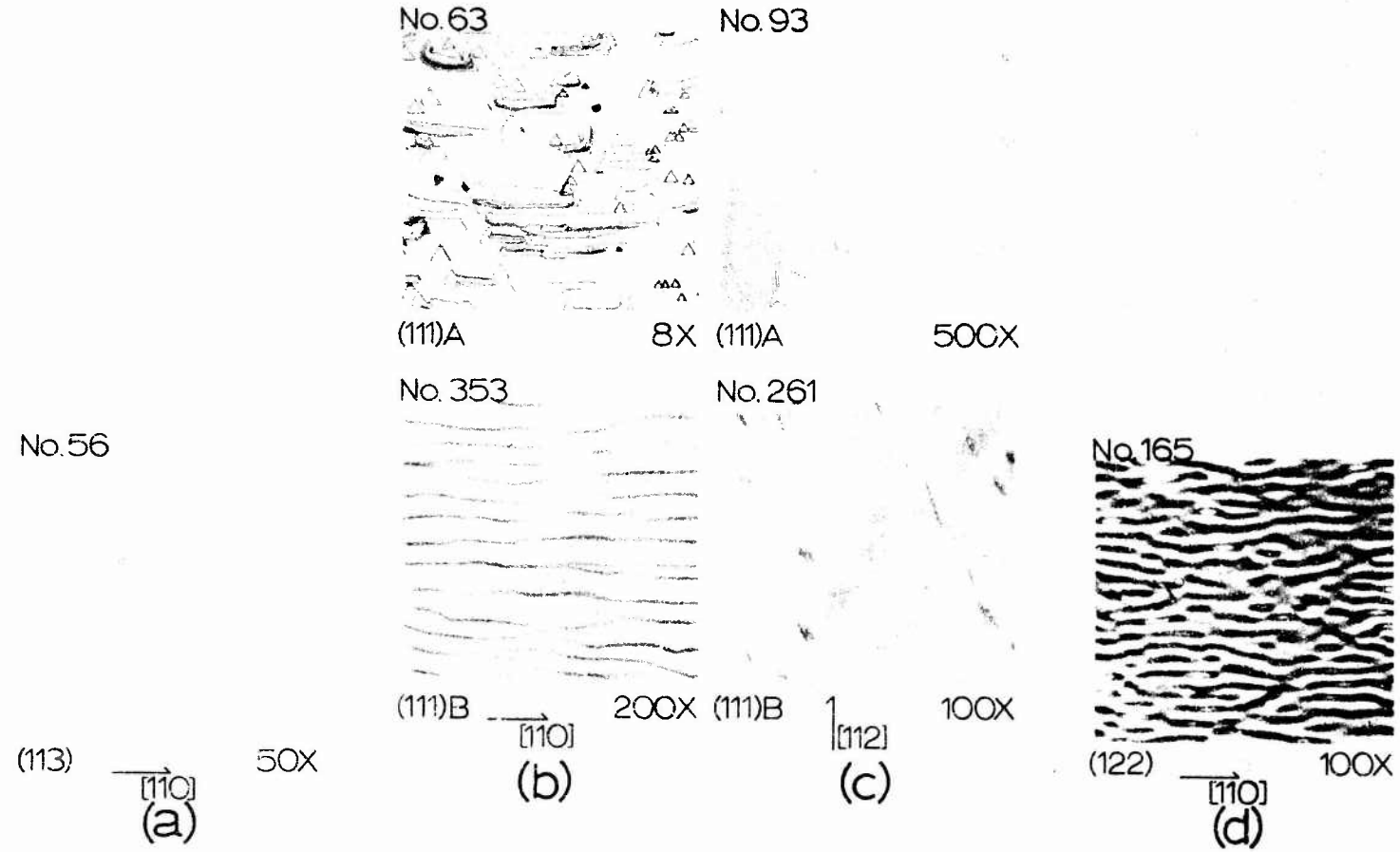

Figure II-10. Characteristic nucleation hillocks and surface terraces observed on (a) (113), (b) and (c) (111), and (d) (122) oriented substrates. The hillocks and terraces are principally bounded by (100) and (111) planes. The hillocks and terraces correspond to the schematic orientations of the substrates shown in Fig. II-9. The terrace orientations shown are for a (111) plane rotated (a) about a [110] axis to a (113) plane, (b) slightly about a [110] axis, (c) slightly about a [112] axis and (d) about a [110] axis to a (122) plane.

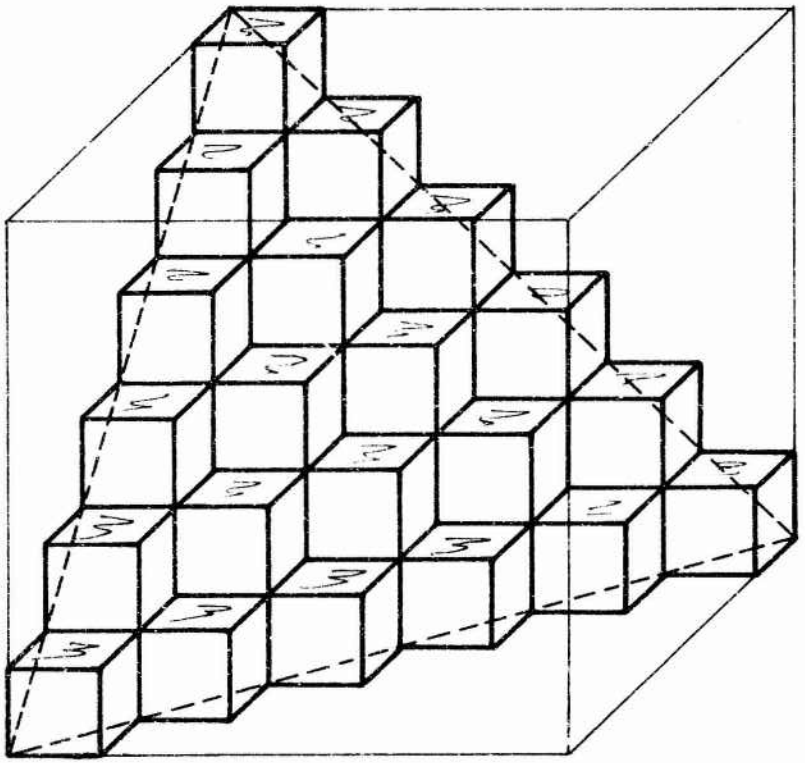

(a)

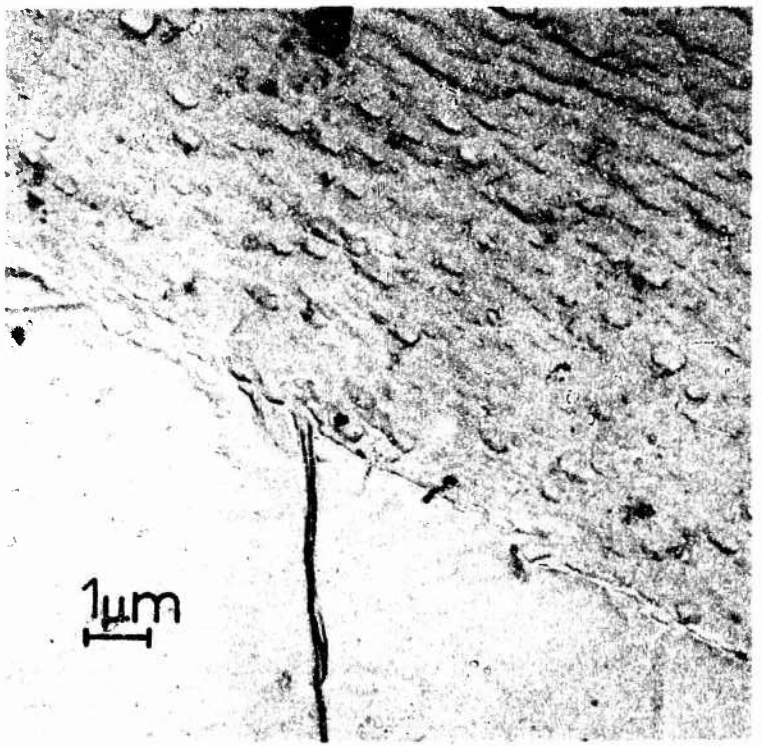

(b)

Figure II-11. (a) A(111) plane made up of (100) planes interlocked on [100] edges. (b) An electron micrograph of a replica taken from a terrace edge for a growth on a (111)B substrate, Growth No. 39. Details of the actual terrace edge are blanketed by a 20 Å to 40 Å oxide layer. Note the remarkable similarity between the shaded (100) planes in (a) and the protruding planes in (b).

(a)

(b)

Figure II-12. Heteroepitaxial growths of LPE GaAs on BeO substrates. (a) Nucleated hillocks oriented about a region wetted by the Ga melt on an as grown prismatic surface. (b) Spontaneous nucleation of hillocks on a rough saw-cut basal surface.

III. DEVICE APPLICATIONS OF GaAs

G. S. Kino, C. F. Quate, G. R. Bisio, S. Kofol, S. Ludvik, F. Grudkovski

I. THE TRAVELING SPACE CHARGE WAVE GaAs AMPLIFIER

A. INTRODUCTION

This project has been concerned with the design and testing of a GaAs traveling wave amplifier for use in the X-band range. The device which is shown in two forms in Figs. III-1 and III-9, respectively, consists of a thin film a few mircons thick of epitaxial GaAs, typically 30-100 μm long, deposited on a semi-insulating substrate. A drift field is applied to the GaAs by means of ohmic contacts. With the drift field above the Gunn threshold, growing carrier waves can propagate along the device.[1] If these waves are excited at one end of the device and detected at the other, broadband amplification can, in principle, be observed.

In order to design an efficient low noise device based on this principle, it is necessary to control the gain so that it is not too large; otherwise the device will oscillate rather than amplify. This is done by choosing the thickness of the semiconductor in accordance with the criteria of Kino and Robson,[2] so that $nd < 2 \times 10^{11}$ cm^{-2}, where d is the thickness of the semiconductor, and n its carrier density. More detailed numerical computations, taking into account the effect of a metal film deposited on top of an insulating layer on the semiconductor have been carried out by Weil[3] and used in our design. Typically the results led us to the conclusion that the material required should be 2 μm thick with a carrier density of approximately 10^{15} cm^{-3} (1 ohm-cm), although there is some choice on n and d, for it is the nd product which

mainly determines the gain per unit length.

A second problem is associated with coupling in and out of the device. We have worked with several possible designs for this purpose. In the simplest form of the device, which looks just like an FET, a grounded gate insulated from the semiconductor by an SiO_2 layer a few thousand Ångstroms thick is deposited between the source and the drain contacts, and the rf signal is applied to the source, and taken out of the drain. This form of the device, gives very weak excitation, and provides insufficient control over the dc field distribution within the device.

Our more recent designs involve the use of a Schottky-barrier contact as the input electrode, and sometimes the use of a similar Schottky-barrier contact for the output electrode, with or without a grounded gate insulated from the semiconductor between the input and output electrodes. The purpose of this grounded gate is in part to control the gain, but more importantly, to shield the input from the output electrodes. Because of the large number of surface states present, the insulated gate has very little effect on the dc fields within the semiconductor.

The Schottky-barrier input electrode has a further important purpose, the control of the dc field within the device. Normally, with no such electrodes present, the field distribution within the device is such that the field within the first one-third to one-half of the device length is below threshold, and carrier waves are attenuated in this region. Consequently, an input signal introduced through the source contact will be rapidly attenuated. If a separate rf input contact is used, it must be located in a region where the field is above threshold. If it is located too far along into this region, further troubles with noise will be

experienced because now noise signals generated in the device will grow for a longer distance than the input signal, the noise amplification will therefore be larger, and the device will be noisy. If, on the other hand, the Schottky-barrier input electrode is located near the source, and its dc potential is controlled so as to lower the current through the device, or equivalently to give a high field at the drain end of the Schottky-barrier (running it as an FET in the saturated current condition) the field through the rest of the device can be kept above the threshold value, and nearly uniform through the device.

In this report we describe our work on devices based on these principles. We have calculated dc field distributions, the input and output impedances of these devices, and conditions for low noise. After carrying out initial experiments on these devices with excellent quality material produced at Stanford, our later experimental results were not successful because we were not able to obtain or produce suitable semiconductor material. So we did not continue the project. However, more recently suitable material is being made at Stanford, which would be suitable for this application.

In our first experiments we used high quality material produced in the [illegible] laboratory at Stanford, Since that time, there had been difficulties in producing the same high quality material. Thus we found it necessary to buy material from Varian Associates. After considerable effort, this material also proved unsuitable. One basic problem was that it was difficult to make good contact to the thin layers used. Eventually poor contacts were made to this material by Varian Associates, and independently, by Hewlett-Packard. We then found problems with trapping in the interface layer between the semiconductor and semi-insulating substrate

which gave the effects of a layer of much higher resistivity than should have been the case. Thus the material proved unsuitable for this application.

B. THE INITIAL EXPERIMENTS

A first batch of GaAs traveling wave amplifiers with Schottky-barrier input gates was designed and fabricated; their configuration is shown in Fig. III-1. A picture of one of the amplifiers is shown in Fig. III-2. The fabrication sequence is indicated in Fig. III-3. The ohmic contacts were fabricated by depositing an alloy of Ag, In, Ge (90:5:5), forming a layer at least 1500Å thick. The contacts were then alloyed in an H_2 atmosphere for 4-5 minutes. The gap between the ohmic contacts was 35 μm; the Schottky-barrier input gate was 5 μm long and had a very small pad to reduce the capacitive coupling to the ground. The grounded gate was 15 μm long with an SiO_2 layer underneath it 5000Å thick. The n-type epitaxial film was grown on a <111> B semi-insulating substrate, 5-10 μm thick and had a nominal but somewhat nonuniform carrier density of 7×10^{14} cm^{-3} so $nd \approx 3.5 - 7 \times 10^{11}$ cm^{-2}. This material was provided by the Center for Materials Research, Stanford.

A typical I-V characteristic, taken between source and drain with the input gate floating, is shown in Fig. III-4. Incoherent oscillations were present at voltages slightly higher than the threshold voltage. All of the devices were tested from 2 to 10 GHz with the circuit shown in Fig. III-5. All devices tended to oscillate, although the theory by Weil[3] did not predict an oscillatory behavior with the values of the parameters chosen.

In this first device the capacitive coupling from input to output was relatively large, due to poor shielding, so that the input-output loss of the device with no drift field applied was only of the order of 13 dB. However, although we could observe a change in output level of a few dBs at 7.5 GHz when the drift field was raised above threshold, it appeared that the coupling of the input signal into the device was extremely weak, and that changes in the external circuitry had very little effect on the oscillations present, which were broadband in the 7-12 GHz range.

1. Investigation of Higher Order Transverse Modes

It will be noted that the theory of Weil indicates that the maximum growth rate should be such that the total gain should be insufficient to give rise to oscillations or saturation on internal noise, despite the relatively large nd product used. We therefore wondered if there could be difficulties due to the presence of higher order transverse modes, with a highly nonuniform distribution of fields over the cross section of the semiconductor. These modes might have rates of growth larger than the fundamental mode considered in the theory, and would couple weakly to the external circuit.

To simplify the analysis we considered a symmetrical device, i.e., a semiconductor slab embedded in a dielectric medium, as illustrated in Fig. III-6, and used the Kino and Robson[2,4] analysis, which neglects diffusion effects, to derive the dispersion relation of the symmetrical space charge wave. The dependence of the wave vector β on the frequency ω was found by tracing the roots of the dispersion equation with a computer. At high frequencies when $\beta_e a = (\omega/v_0)a \gg 1$, where $\beta_e = \omega/v_0$, v_0

is the drift velocity of the carriers, and d = 2a is the thickness of the semiconductor. The numerical results indicate that $\mathrm{Re}(\beta) \gtrsim \beta_e$, $\mathrm{Im}(\beta) \gtrsim \beta_{cz} = (qn\mu_z/\varepsilon v_0)$ and $\mathrm{Re}(\beta_y) \gtrsim (2m + 1)(\pi/2a)$ and $\mathrm{Im}(\beta_y) \gtrsim 0$. The fundamental mode (m = 0) does not have a low frequency cutoff, but the m^{th} higher order mode has a low frequency cutoff approximately where $\beta_y = 2m(\pi/2a)$. The spatial distribution of the rf potential is sketched in Fig. III-7 for the first three modes. Figure III-8 shows $\mathrm{Im}(\beta_z a)$ vs $(\beta_e a)$ for the first three modes for the case $|\beta_{cz}|a = 2$, which is in the range of interest ($nd \gtrsim 2 \times 10^{11}$), $\mu_z = 2000$ cm/V-sec and $\varepsilon' = \varepsilon$.

In our computations the growth rate of the higher order modes always turned out to be less than that of the fundamental mode, but quite close to it (about 10% less at high frequencies). The stability was also analyzed in terms of higher order longitudinal modes, i.e., higher order roots of the impedance of the device.[5] Once again, the fundamental mode appeared to be the most important one.

At all events, although the theory always indicated that the growth rate of the fundamental mode was higher than that of the higher order modes, it did tend to indicate that if semiconductor layers of the order of 10 μm thick were used, the growth rates of the higher order transverse modes could be comparable to the fundamental. It therefore seemed wise to design much thinner devices with a somewhat lower nd product, so that the cutoff frequency of the higher order modes, determined by $\omega a/v_0$ = constant would be decreased so they could not propagate in the frequency range of interest.

C. SECOND DESIGN OF THE AMPLIFIER

A new design of the amplifier was then carried out. The main features of the new design are: reduced epi-layer thickness of 1 - 3 m; a reduced value of the nd product to 2-3 x 10^{11} cm^{-2}; input and output Schottky-barrier gates. A Schottky-barrier ohmic contact extension was also used to control the dc field distribution; there was also mesa etching around the active device, so that bigger input and output gate bonding pads could be placed on the semi-insulating substrate and yet have a small capacity to ground. Later we concluded that it would be better, for low noise operating to use the input Schottky barrier to control the dc field rather than a Schottky barrier extension of the source or gate.

The configuration of the new design is shown in Fig. III-9. The thickness of the SiO_2 layer is 3000-6000 Å. The width of the device is 500-1000 μm and the other dimensions are shown in the blow-up of Fig. III-10 for the two sets of devices.

The device design is similar in its configuration to an insulated gate film transistor; the difference is that in this device the insulated gate is normally at rf ground, and the input and output rf signals are fed into two Schottky-barrier gates located near the dc source and drain electrodes. The Schottky-barrier extension at the source and drain electrodes gives further control over the dc field distribution. Some of the devices on the chip were intended to use a grounded insulated gate, others to have the insulated gate present. Also on the same chip there were intended to be simple diodes along which we expected to measure the dc potential profile with a moveable probe, which we had developed.

1. Fabrication of Devices

The mesa etching procedure was first investigated by using a <111>B orientation. We were able to obtain reasonable slopes for the mesa profile, so that the gate metalization did not suffer cracks crossing the mesa step. The feasibility of using a <100> orientation was then investigated, since it became easier to purchase material with this orientation. We were able to repeat the same kind of mesa etching technique on a <100> surface.

The construction of these devices was severely delayed owing to difficulties in obtaining the required epitaxial material. We bought epitaxial layers of n-GaAs grown on a semi-insulating Cr-doped GaAs substrate oriented <111>B, from Varian Associates. The thickness of the epitaxial layer was 1.7 μm and the carrier density was 1.5×10^{15} cm^{-3}. The dimensions of the sample were (1 x 2 cm), enough to make four sets of devices, each set having two series of twelve devices.

As we already described, we experienced great difficulties with the InGeAg and GeAu contacting processes, which had worked perfectly with Stanford material. Commercial material, normally deposited on n^+ substrates did not seem to be suitable for this application. Material which was made at Stanford, after we had ceased our major activity on this project, seemed to be much more suitable for the purpose. Some devices are presently being made this this material.

II. ACOUSTIC DEVICES

A. LINEAR ACOUSTIC AMPLIFIERS

We have studied the amplification characteristics of the Rayleigh and Bleustein waves in GaAs and have demonstrated the large gains available for the Bleustein wave because of its greater penetration depth. Emphasis has been placed on obtaining broadband terminal gain through the use of zinc oxide thin film transducers deposited on the sides of the prism configuration of Fig. III-11. Longitudinal bulk waves excited by the input transducer are converted to the Bleustein or shear mode at the prism boundary. Transducers have been fabricated on this structure with a conversion efficiency of 8 db and tuned bandwidth exceeding 100 MHz at the center frequency of 650 MHz.

The material we have worked with thus far has been O_2 doped bulk GaAs, which was heated to optimize the amplification characteristic. At 100°C with an average resistivity of 18 Ω-cm, we have observed a net terminal gain approaching 25 db at a pulsed drift voltage of 1.26 kv. A major problem encountered with the present bulk material has been the presence of large resistivity gradients along the length of the device. Such gradients are not uncommon in oxygen doped material and degrade the efficiency of the amplifier. By using a thick epitaxial layer on a semi-insulating substrate, we hope to eliminate this difficulty as well as to obtain cw operation.

B. NONLINEAR INTERACTIONS OF ACOUSTIC WAVES

In our previous report, we have demonstrated that the presence of carriers in GaAs greatly enhances the efficiency of acoustic wave signal

processing operations such as real time convolution. The nonlinearity has been shown to be on the order of 30 db greater than that available in strong piezoelectric materials such as $LiNbO_3$. Our recent efforts in improving the Rayleigh wave devices has been directed toward increasing the transducer efficiency. Previous interdigital structures deposited directly on the substrate have resulted in 20 to 25 db insertion loss per transducer. This is caused by the low piezoelectricity of the GaAs as well as the effect of electronic conduction in the epitaxial layer under the Schottky barrier electrodes of the transducer.

In order to increase the conversion efficiency and bandwidth, we are investigating ZnO overlay structures. Recent advances[6,7] in the excitation of Rayleigh waves on nonpiezoelectric substrates suggests the application of the technique to GaAs. Two transducer configurations of interest are shown in Fig. III-12. Theoretical analysis of these structures have been carried out using a computer program developed at Stanford. The results for a (001) oriented GaAs substrate with Rayleigh wave propagation along a <110> direction and c-axis oriented ZnO are shown in Fig. III-13. The parameter $\Delta v/v$ represents a measure of the transducer coupling efficiency. With increasing $\Delta v/v$, the required number of finger pairs of the transducer is reduced which in turn increases its bandwidth.

We have fabricated transducers on GaAs in the configuration of Fig. III-12(a) with a one port insertion loss of 12 db at 165 MHz. This would represent an overall device improvement on the order of 20 db.

C. NONLINEAR ACOUSTIC WAVE INTERACTIONS: TIME REVERSAL

The current interest in the performance of the function of time inversion through nonlinear interactions in piezoelectric crystals arises

mainly from two applications. Variable delay of a symmetric waveform may be achieved by delaying the recall pulse. The function of correlation of arbitrary waveforms may also be achieved by first time reversing a reference signal and then convolving with another signal. The fact that the latter goal is difficult to demonstrate in present parametric acoustic devices stems primarily from the low efficiencies available from elastic nonlinearities. Another difficulty arises from the presence of propagation loss in the delay line which causes an exponential weighing of the reversed signal relative to the input.

We have proposed a remedy for the latter problem by using the electronic nonlinearity in the Bleustein wave amplifier configuration of Fig. III-11. For time reversal, a space invariant second harmonic voltage of short duration applied across the ohmic contacts interacts with the fundamental input acoustic wave to produce a backward traveling acoustic wave at the fundamental frequency. By applying an amplifying drift field either before or after time reversing, the exponential weighing can be counteracted and control of distortion can be achieved. We have observed time reversal with loss compensation and variable delay with this configuration. The device was heated to optimize the interaction and pulsed drift fields applied to compensate for propagation losses. The essential features are shown in Fig. III-14. In Fig. III-14(a), variable delay of the input at 650 MHz (not shown) is achieved by delaying the drift field and time-reversing pulse at 1.3 GHz. Note that the reversed pulse is delayed by twice the differential delay of the recall pulse. In Fig. III-14(b) we show reversal of a short and long pulse sequence. In Fig. III-14(c), loss compensation is demonstrated for a long rectangular input. (For no drift field after reversal, only the

leading edge was observed.) The extra spikes in the photos are caused by feedthrough of the drift voltage and pulsing of the local oscillator.

The results are rudimentary at present mainly because of the resistivity gradient in the bulk O_2 doped material used. The inhomogeneity has the effect of distributing the applied voltage unequally along the device as well as altering the parameters of the interaction. By using epitaxial material provided by CMR, we hope to eliminate this difficulty.

The important features of the present interaction are that time reversal is possible with predicted efficiencies much greater than available in purely piezoelectric materials and with control of distortion.

REFERENCES

III-1. P. N. Robson, G. S. Kino and B. Fay, "Two-Port Microwave Amplification in Long Samples of Gallium Arsenide," IEEE Transactions on Electron Devices, ED-14, 9, 612-615 (September, 1967).

III-2. G. S. Kino and P. N. Robson, "The Effect of Small Transverse Dimensions on the Operation of Gunn Devices," Proc. IEEE 56, 11, 2056-2057 (November, 1968).

III-3. H. M. Weil, "Space Charge Wave Amplification in Thin Gallium Arsenide Films," Ph.D. Dissertation, W. W. Hansen Laboratories of Physics, Stanford University, Stanford, California.

III-4. G. S. Kino, "Carrier Waves in Semiconductors - I: Zero Temperature Theory," IEEE Trans. on Electron Devices, ED-17, 3, 178-192 (March, 1970).

III-5. W. Heinle and R. W. H. Engelmann, "Stability Criterion for Semiconductor Plates with Negative AC Mobility," Proc. IEEE 60, 7, 914 (July, 1972).

III-6. R. S. Wagers, P. Galle, D. K. Winslow and G. S. Kino, IEEE Ultrasonics Symposium (1972).

III-7. F. S. Hickernell, J. Appl. Phys., Vol. 44, No. 3, pp. 1061-1071 (1973).

FIGURE CAPTIONS

Figure III-1. Schematic top view of the GaAs amplifier with Schottky-barrier input gate.

Figure III-2. Picture of the amplifier (50X magnification).

Figure III-3. Fabrication sequence of the GaAs amplifier.

Figure III-4. I-V characteristic of the GaAs amplifier, taken between source and drain, with the input Schottky-barrier gate floating.

Figure III-5. RF testing circuit for the GaAs amplifier.

Figure III-6. Geometry used in the discussion of higher order modes.

Figure III-7. Spatial distribution of the rf potential.

Figure III-8. $Im(\beta_z)$ vs $\beta_e a$ for the first three modes (μ_z = 2000 cm^2/V-sec, $\varepsilon' = {}^{e}\varepsilon$).

Figure III-9. Schematic view of the GaAs amplifier with Schottky-barrier input and output gates. A--semi-insulating GaAs substrate; B--n-type GaAs epitaxial layer; C--ohmic contacts; D_1--Schottky-barrier contact extension; D_2--Schottky-barrier gates; E--insulating layer; F--insulated gate.

Figure III-10. Blow-up of the center section of the amplifier.

	I (μm)	II (μm)
ℓ_1	93	70
ℓ_2	85	65
ℓ_3	5	5
ℓ_4	5	5
ℓ_5	65	45
ℓ_6	56	36

Figure III-11. GaAs prism amplifier configuration.

Figure III-12. ZnO overlay transducer structures.

Figure III-13. $\Delta v/v$ vs kh ($k=2\pi/\lambda$) for ZnO overlay transducer structure on GaAs.

Figure III-14. Time reversal characteristics.

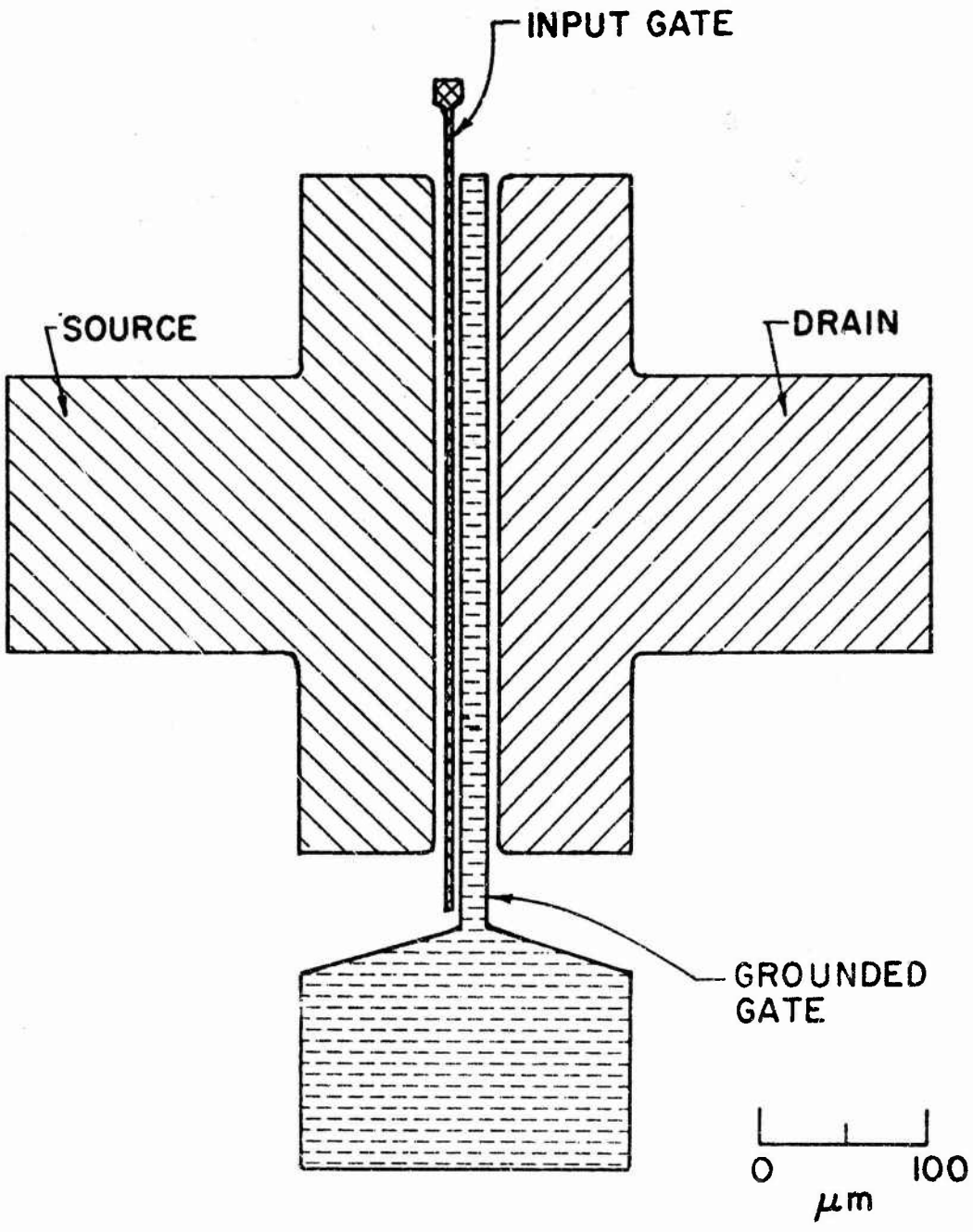

Figure III-1. Schematic top view of the GaAs amplifier with Schottky-barrier input gate.

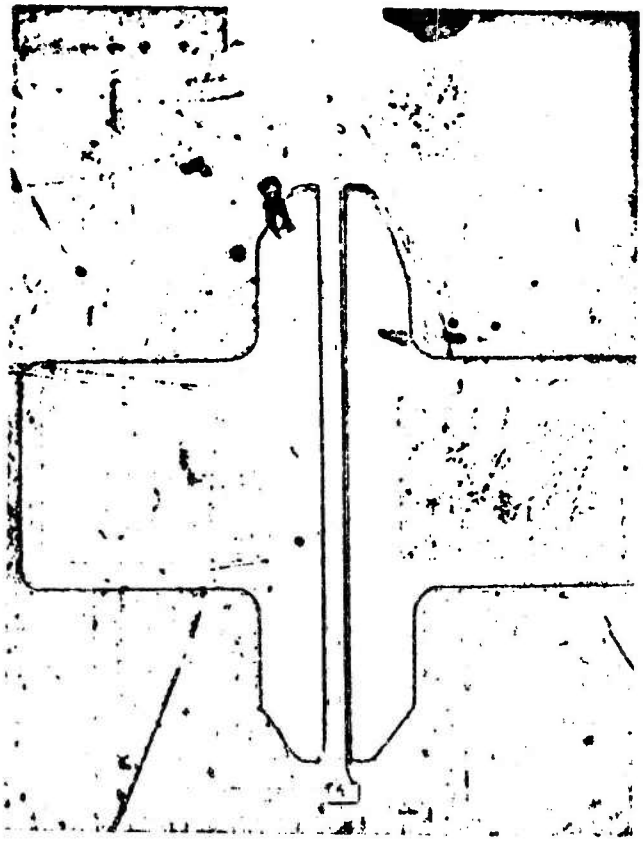

Figure III-2. Picture of the amplifier (50X magnification).

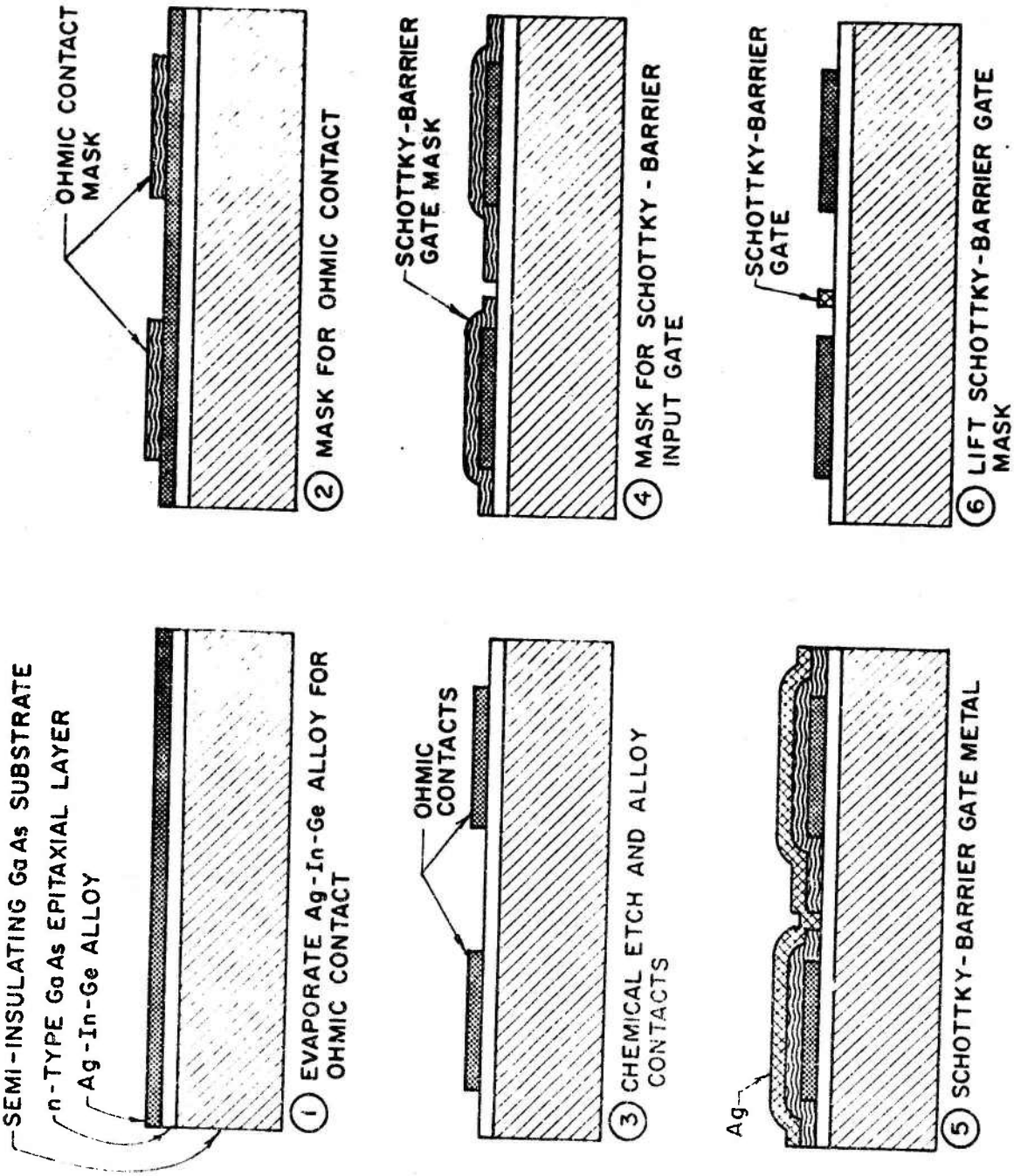

Figure III-3. Fabrication sequence of the GaAs amplifier.

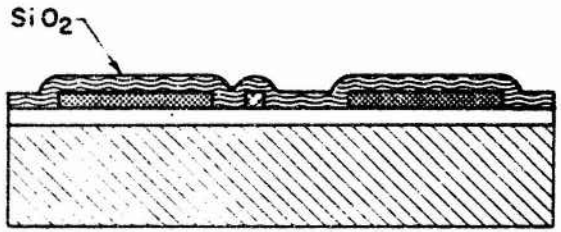

(7) RF-SPUTTER DEPOSITE SiO_2

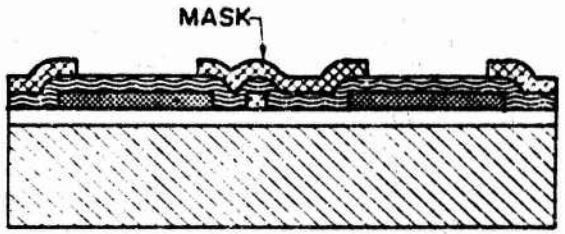

(8) MASK FOR ETCHING THROUGH SiO_2

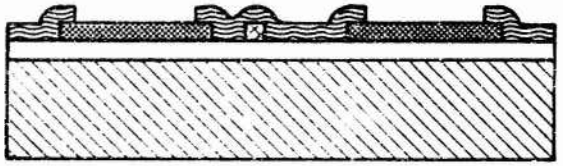

(9) ETCH THROUGH SiO_2

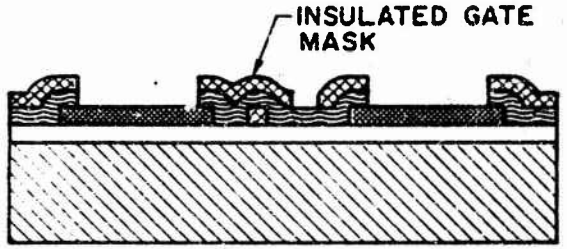

(10) MASK FOR INSULATED GATE

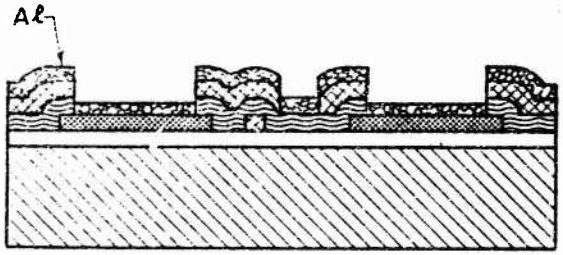

(11) EVAPORATE INSULATED GATE METAL

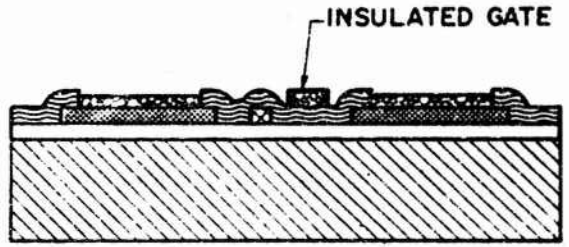

(12) LIFT INSULATED GATE MASK

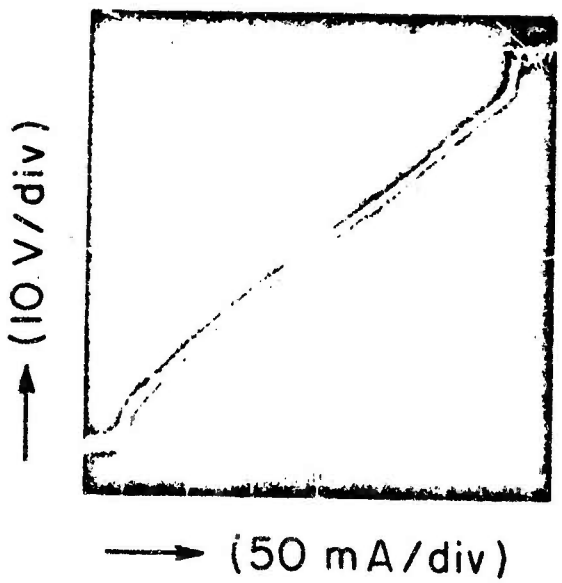

Figure III-4. I-V characteristic of the GaAs amplifier, taken between source and drain, with the input Schottky-barrier gate floating.

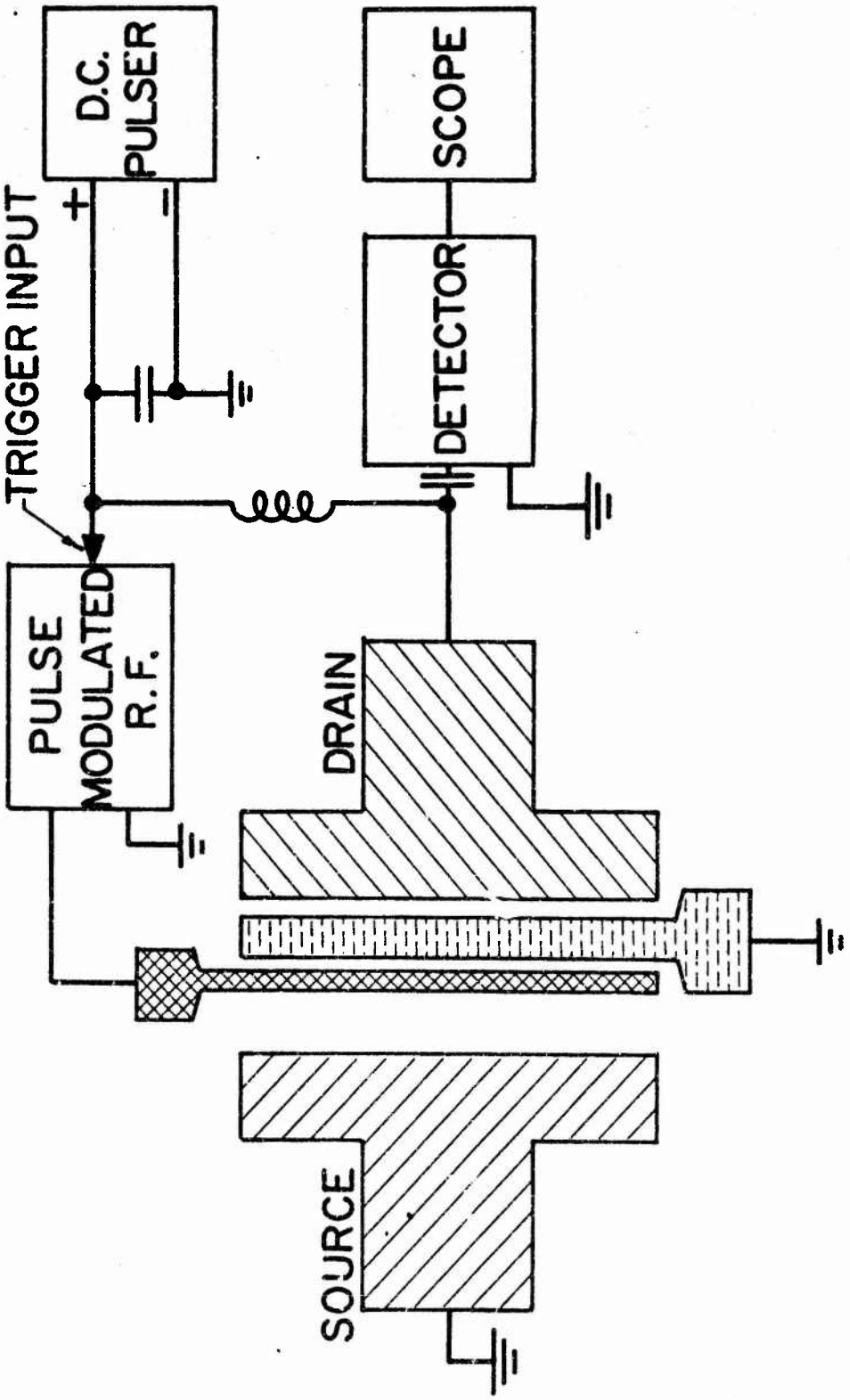

Figure III-5. RF testing circuit for the GaAs amplifier.

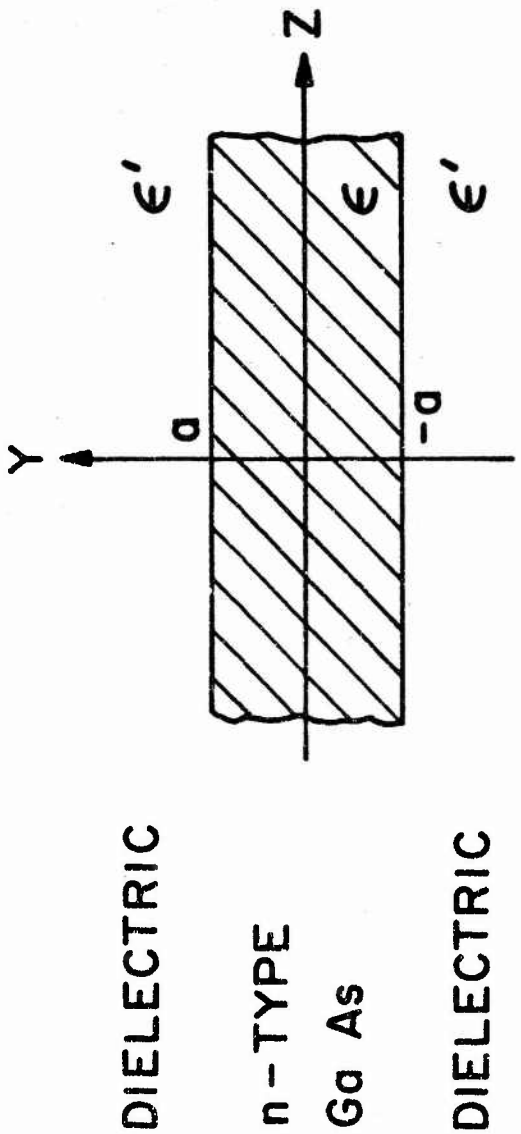

Figure III-6. Geometry used in the discussion of higher order modes.

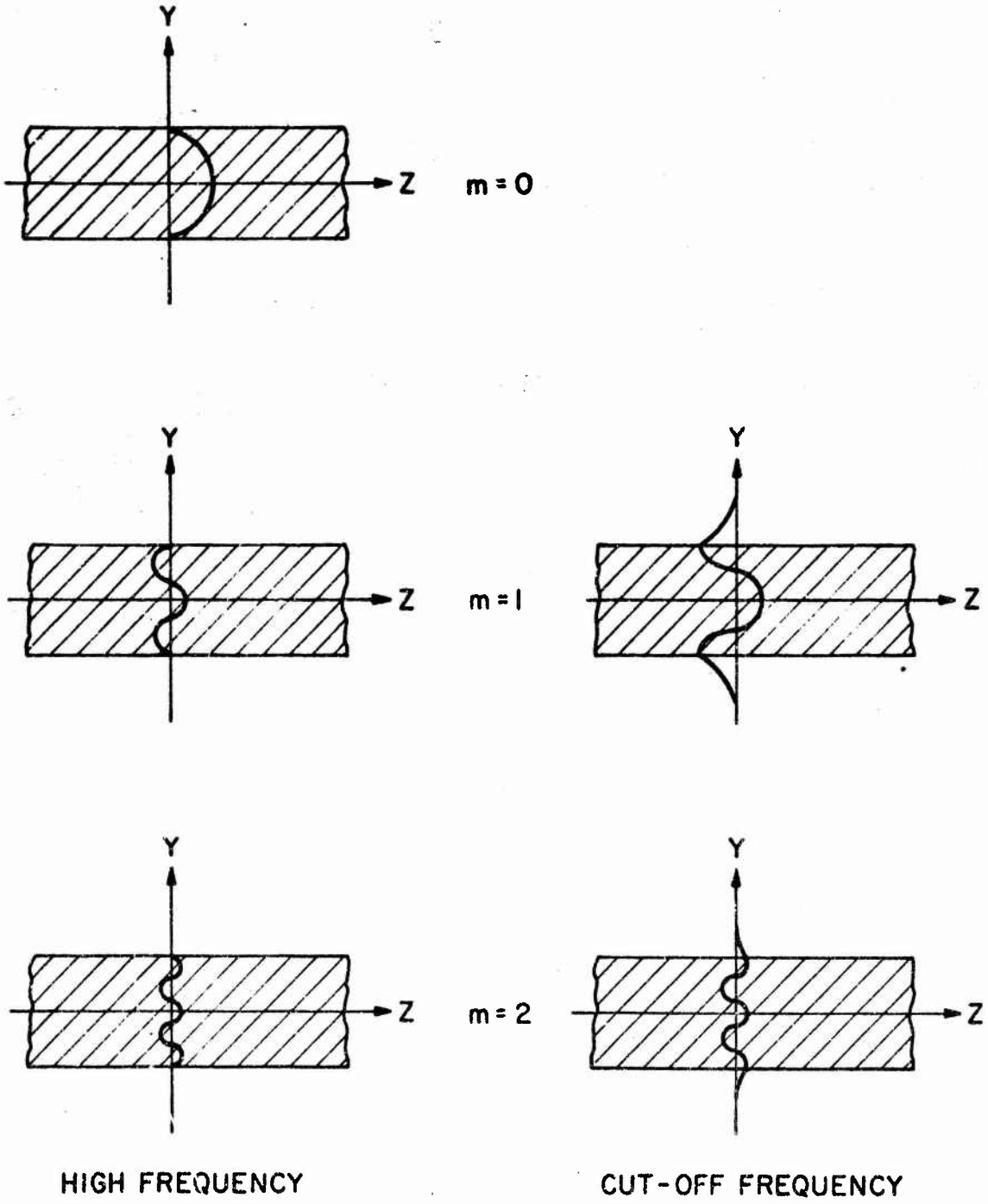

Figure III-7. Spatial distribution of the rf potential.

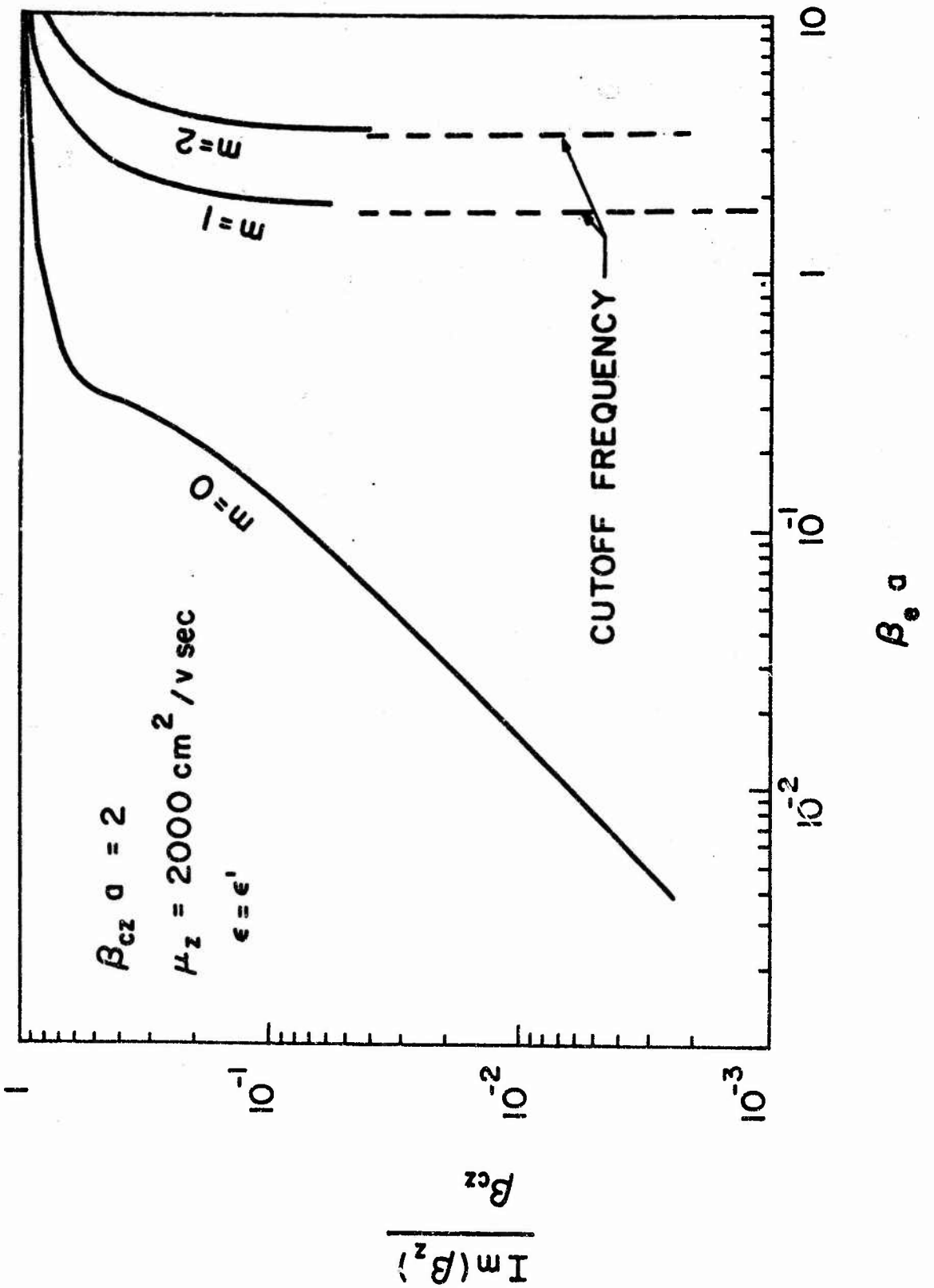

Figure III-8. $Im(\beta_z)$ vs $\beta_e a$ for the first three modes (μ_z = 2000 cm^2/V-sec, $\epsilon' = \epsilon_e \epsilon$).

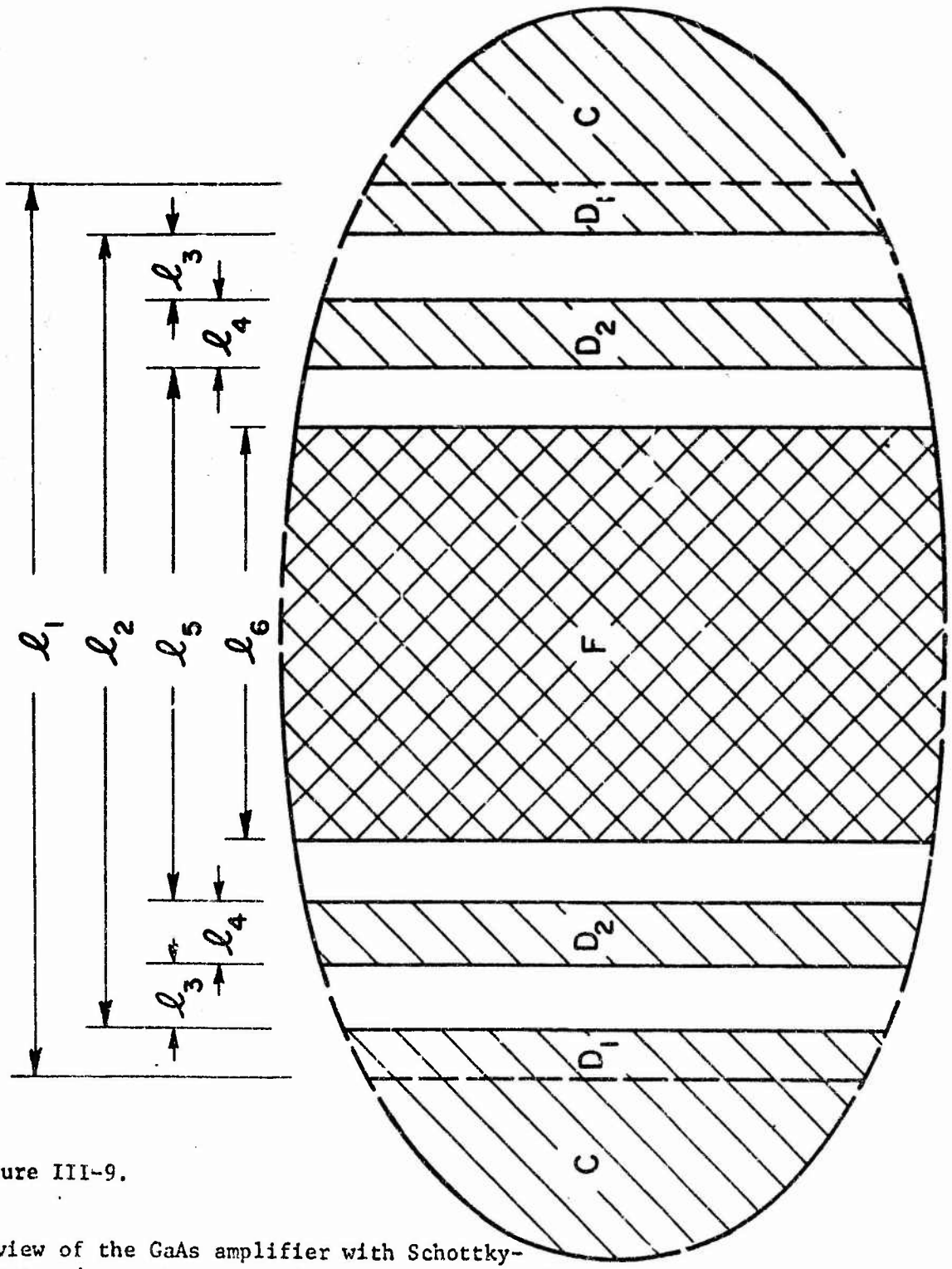

Figure III-9.

chematic view of the GaAs amplifier with Schottky-
arrier input and output gates. A--semi-insulating GaAs
ubstrate; B--n-type GaAs epitaxial layer; C--ohmic
ontacts; D_1--Schottky-barrier contact extension; D_2--
chottky-barrier gates; E--insulating layer; F--insulated
ate.

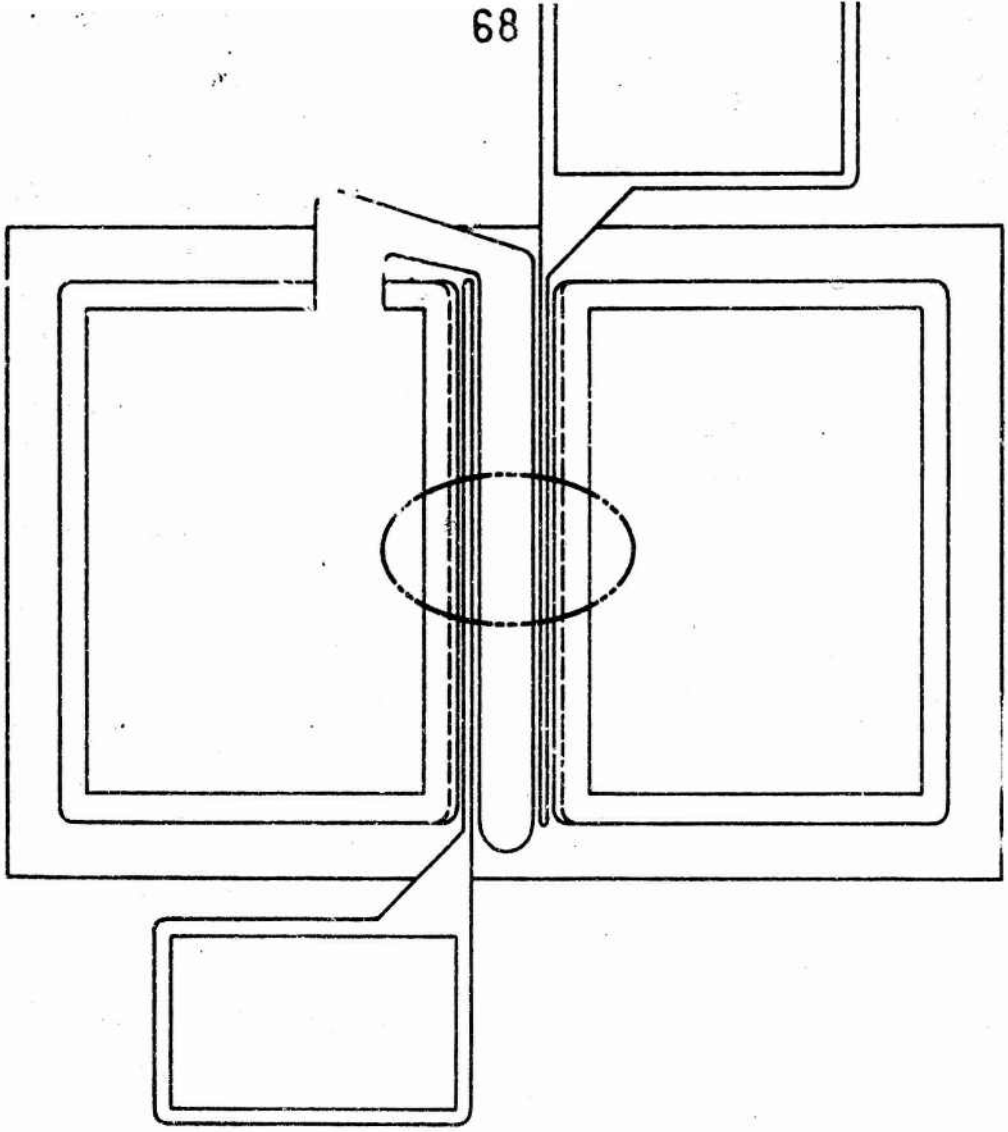

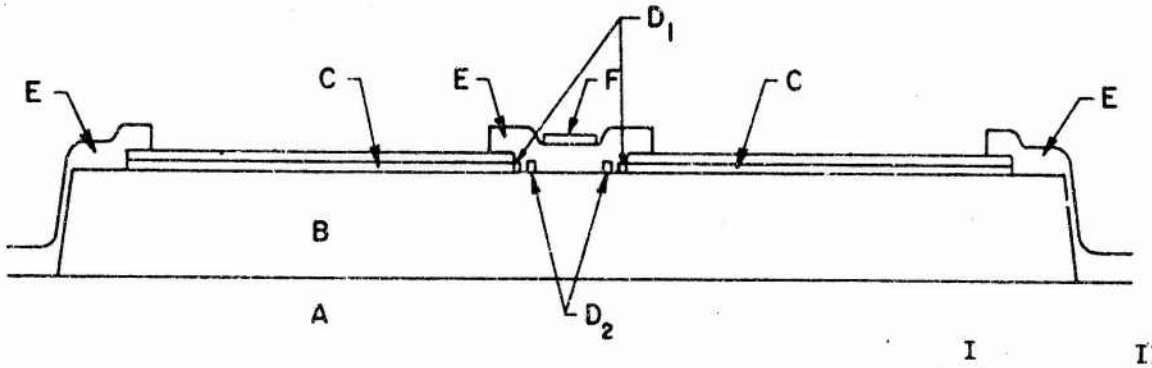

Figure III-10.

Blow-up of the center section of the amplifier.

	I (μm)	II (μm)
ℓ_1	93	70
ℓ_2	85	65
ℓ_3	5	5
ℓ_4	5	5
ℓ_5	65	45
ℓ_6	56	36

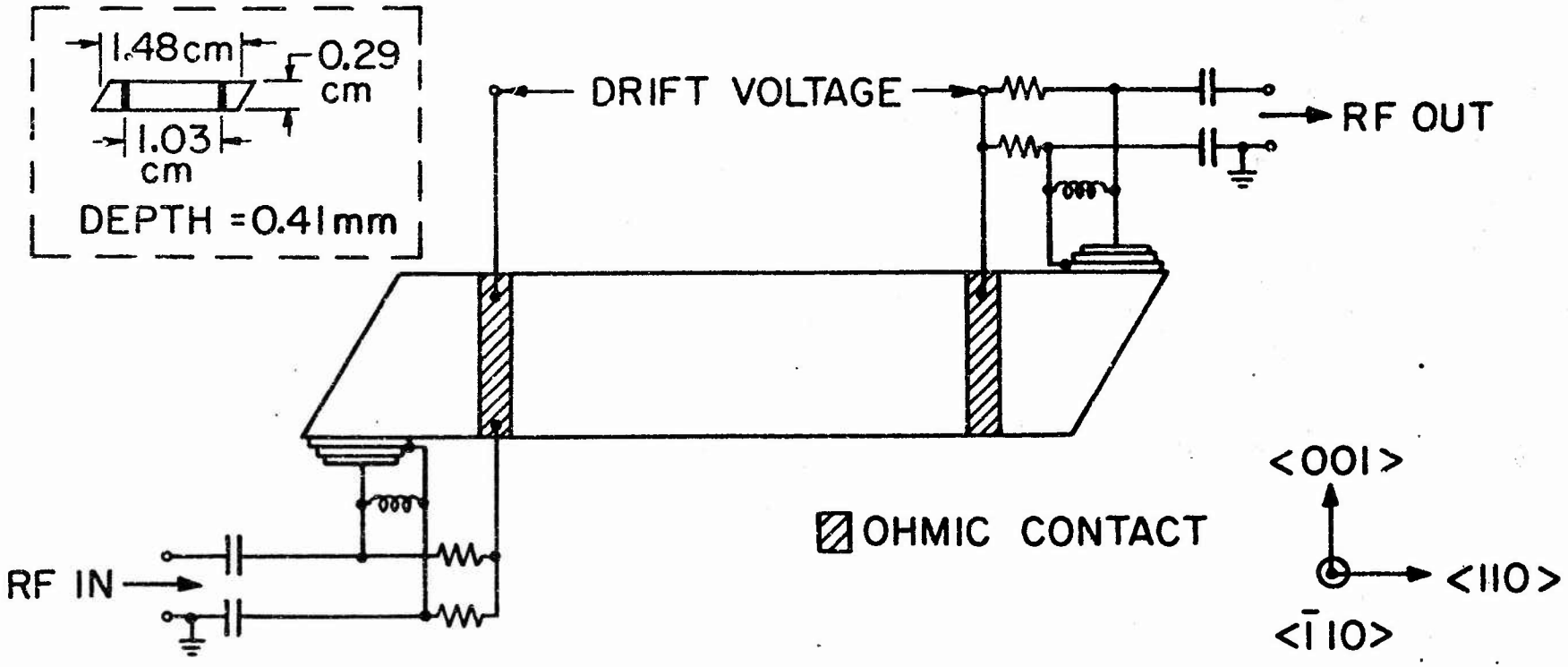

Figure III-11. GaAs prism amplifier configuration.

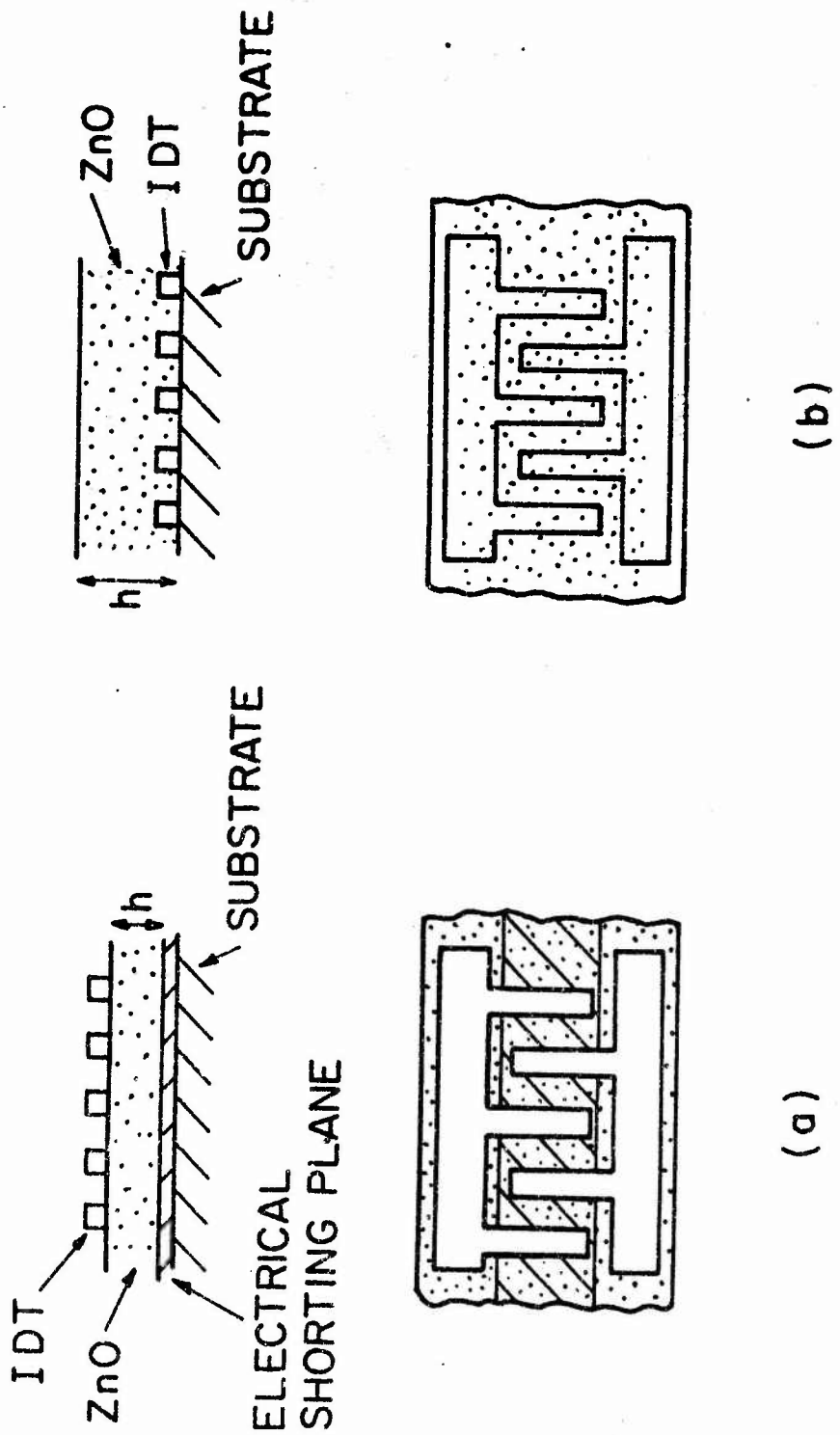

Figure III-12. ZnO overlay transducer structures.

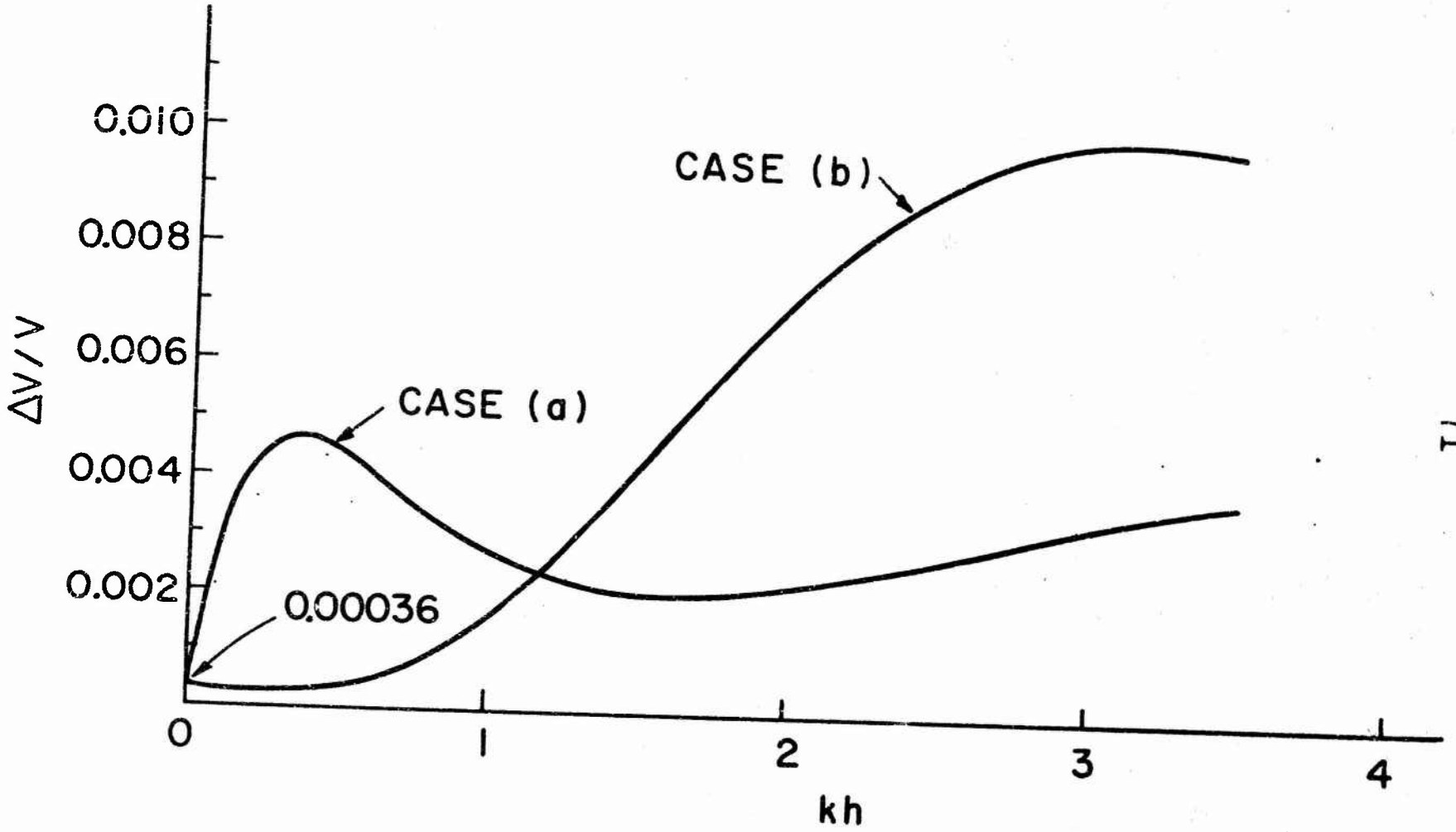

Figure III-13. Δv/v vs kh (k=2π/λ) for ZnO overlay transducer structure on GaAs.

RECALL PULSE (2ω)

REVERSED SIGNAL (ω)

2μsec

(a)

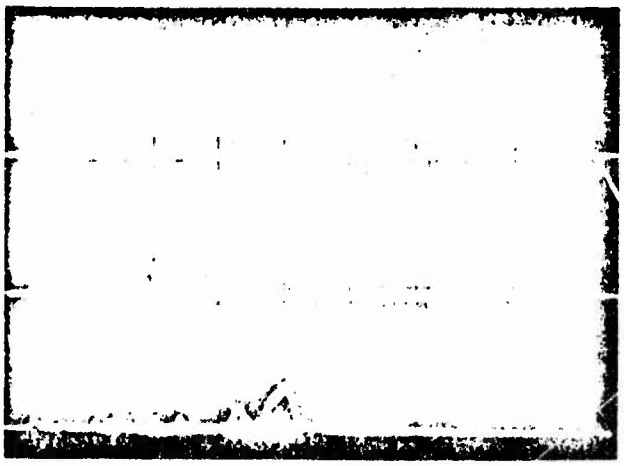

INPUT SIGNAL (ω)

RECALL PULSE (2ω)

REVERSED SIGNAL (ω)

(b)

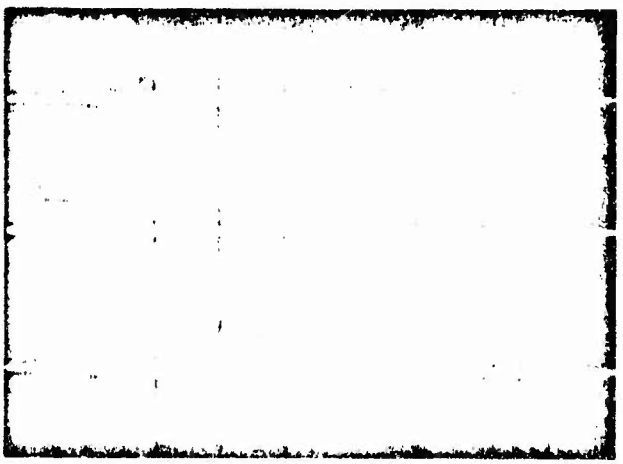

RECALL PULSE (2ω)

INPUT SIGNAL (ω)

REVERSED SIGNAL (ω)

(c)

Figure III-14. Time reversal characteristics.

IV. RELATIONS BETWEEN DISLOCATIONS AND MECHANICAL PROPERTIES AND THE PRODUCTION AND CHARACTERIZATION OF DEFECT STRUCTURES IN COMPOUND SEMICONDUCTORS

R. H. Bube, W. D. Nix and A. L. Lin

A. PROGRAM OBJECTIVE

The principal effect of dislocations in devices involves reduction of the minority carrier lifetime, which in turn causes degradation of semiconductor lasers, decreasing efficiency of Gunn diodes, etc. The electronic properties of dislocations in semiconductors have been worked out in detail only in germanium and silicon in the past two decades. Through the knowledge of the properties of dislocations, several devices such as the photoelectric frequency converter[1], the dislocation field-effect transistor[2] and the stress-strain transducer[3] have been made by intentionally introducing a dislocation plane in the elemental semiconductors. The development of III-V compound semiconductor devices has made increasingly desirable an understanding of the electronic properties of dislocations and methods of controlling dislocation arrangements in III-V compounds, especially GaAs. In order to avoid introducing further complexity into an already rather complex GaAs matrix, it seems desirable to use undoped GaAs in the study of dislocations. Unfortunately, the best bulk material of undoped GaAs presently available has a free carrier concentration of $10^{16}/cm^3$, while the dislocation density attainable through high temperature bending is of the order of $10^{17}/cm^2$, which at best produces $10^{14}/cm^3$ active centers. Therefore the effects due to dislocations are masked by those due to existing imperfections and free carriers in the As-grown sample.

Another possibility is to use high-resistivity GaAs in which the masking effect of free carriers can be greatly reduced. GaAs:Cr was

chosen because of its low carrier density and rather uniform dark resistivity from one ingot to another.

Our measurements of electrical conductivity, Hall and photo-Hall effect, photoconductivity and thermally stimulated conductivity indicate that the electrical properties in the bulk of GaAs:Cr are affected at least as much by the heating necessary to achieve bending as by the bending itself. The measured properties are controlled primarily by the imperfections present in the crystal rather than by deformation-induced dislocations, especially if complex centers exist. We did find, however, that the photoexcited carrier lifetime and Hall mobility were appreciably changed by heating and bending. To interpret these data more fully, we have concentrated on an understanding of the photoconductivity characteristics of high-resistivity GaAs itself.

The properties of high-resistivity GaAs are interesting not only from a basic point of view,but also from practical aspects of its use in devices, such as detectors for radioactive radiation, generation of microwave emission, and electro-optical modulation of CO_2 laser emission, etc., as well as in connection with its use as a substrate for epitaxial GaAs layers.

One of the major impressions received by surveying the literature and our own measurements on high-resistivity GaAs:O and GaAs:Cr is that mass spectrographic analysis of the crystals used, however, indicates only about 1.8 ppm of incorporated oxygen impurity. (Analysis also indicates 0.46 ppm of C, 0.27 ppm of Al, 0.15 ppm of N, 0.1 ppm of Na, 0.07 ppm of Cl, and 0.05 ppm of Si, etc.)

B. EXPERIMENTAL RESULTS

1. Dark Conductivity and Hall Effect

The activation energy measured from the temperature dependence of dark conductivity is 0.48 eV between 295° and 300°K. The Hall mobility is approximately independent of temperature in this range, but decreases with decreasing temperature below 295°K, a decrease which cannot be attributed to a simple two-carrier effect. The Fermi level location calculated from the Hall coefficient at 300°K is 0.58 eV below the bottom of the conduction band.

2. Photoconductivity Spectral Response

Figure IV-1 shows the spectral response curves for photoconductivity and photo-Hall mobility measured at 295° and 213°K. The curve at 213°K differs only slightly from that at 295°K.

The spectral response curve measured at 82°K is quite different. Figures IV-2(a) and IV-2(b) show the spectral response for photoconductivity and photo-Hall mobility as measured 3 min and 15 min after onset of photoexcitation (very long time constants are found over part of the spectral range) in two different ways: (1) measuring from high to low photon energy of a previously heated and cooled (in the dark), and (2) measuring from low to high photon energy on a previously heated and cooled (in the dark) crystal. The results can be interpreted to indicate two states for the crystal: a higher sensitivity n-type state (except for the range between 1.0 and 1.3 eV) which is encountered at high energies when measuring from high-to-low photon energies, and is encountered at low energies when measuring from low-to-high photon energies, i.e., over that portion of the spectral range encountered before exposing

the sample to wavelengths in the 1.0-1.3 eV range; and a lower sensitivity p-type state to which the higher sensitivity n-type state is reduced by exposure to 1.0-1.3 eV photons. The photoconductivity in the p-type state is about two orders of magnitude smaller than that in the n-type state.

3. Photoconductivity vs Temperature

Curves 1, 2 and 3 in Figs. IV-3(a) and IV-3(b) show the temperature dependence of photoconductivity and photo-Hall mobility for intrinsic excitation (at the photoconductivity maximum). Curve 1 represents the crystal in its high-sensitivity state. The effective activation energy for low-temperature photoconductivity is 0.066 eV. Curves 2 and 3 represent the crystal in a low-sensitivity state induced by exposure for one hour at 82°K to 1.08 and 1.18 eV radiation, respectively. This quenching process is very persistent at low temperatures, and the low-sensitivity quenched state remains unchanged long after the removal of the quenching radiation. Upon heating, however, Figs. IV-3(a) and IV-3(b) show a rapid and dramatic recovery from the low-sensitivity quenched state to the high-sensitivity state when the temperature exceeds 105°K, which is completed by 125°K. Reference to the thermally stimulated current data in Table IV-1 shows that this is also exactly the temperature range in which the emptying of a 0.23 eV trap occurs in GaAs:O; data for GaAs:Cr indicate quite similar behavior. It appears that the persistent low-temperature, low-sensitivity quenched state is due to a large density of photoexcited holes, corresponding to electrons trapped in the electron traps, transferred to fast-recombination centers by the quenching radiation.

Curve 4 shows the temperature variation of photoconductivity and photo-Hall mobility for simultaneous intrinsic and extrinsic (1.18 ev) excitation. Both curves 3 and 4 have the same characteristics. The decrease in photoconductivity between curve 3 and curve 4 in the temperature range 125° to 225°K is due to a fast quenching process described below.

4. Optical Quenching of Photoconductivity

Figures IV-4(a) and IV-4(b) show optical quenching spectra and the transient behavior of optical quenching for GaAs:O at 82°K and 213°K, i.e., below and above the critical temperature for the persistent quenching effect. At room temperature under the same experimental conditions, there is no observable optical quenching for the entire spectrum range.

At 82°K, the onset of optical quenching is at 0.5 eV with an abrupt increase at about 0.77 eV. In the spectral range from 0.5 to 0.65 eV and from 0.8 to 1.0 eV, the quenching light produces only quenching of the photocurrent without any associated excitation. Between 0.73 and 0.77 eV, there is a small excitation of photocurrent after abrupt quenching. The quenching and recovery processes in these spectral regions are relatively fast. When the quenching photon energy exceeds 1.03 eV, however, three processes are found: (1) a fast excitation, (2) a fast quenching, and (3) a slow and very large quenching, corresponding to the persistent effects described above.

5. Thermally Stimulated Conductivity

The results of thermally stimulated conductivity measurements after intrinsic excitation at 82°K are summarized in Table IV-1. Our previous data on GaAs:Cr, those of Haisty, measured on "undoped" high-resistivity

GaAs, and those of Blanc, et al., measured on Cu-diffused high-resistivity GaAs, are also shown in the same table. The agreement between the peaks found by us and those reported by Haisty is very close, indicating a characteristic materials property. Estimate of the trap depths indicates that they probably all lie between 0.19 and 0.42 eV. Thermally stimulated Hall measurements indicate these traps are all electron traps. Preliminary considerations indicate that this trap family may result from a pair-complex defect (e.g., Si-O) with different pair spacings giving rise to the different trap depths.

6. Discussion

A proposed model of localized extrinsic energy levels, corresponding to the results obtained for GaAs:O, is shown in Fig. IV-5. Levels a-f are electron traps determined from the peaks of thermally stimulated current shown in Table IV-1. Levels 1, 2 and 3 are acceptor-type imperfections. In thermal equilibrium, level 1 is partially occupied, and both levels 2 and 3 are completely occupied. The dark conductivity near room temperature is determined by the thermal excitation of electrons from level 1; the activation energy of the dark conductivity gives a distance between level 1 and the conduction band of 0.48 eV (at 0°K) for our GaAs:O crystal. The low-energy photoconductivity threshold at about 0.68 eV at 295° and 213°K in Fig. IV-1, and at about 0.74 eV at 82°K in Fig. IV-2 corresponds to transitions of type II. The slight structure at about 1.0 eV at 295° and 213°K may be caused by transitions of type V.

From the optical quenching spectrum of Fig. IV-4(a) and the corresponding transient behavior of Fig. IV-4(b), we find a 0.5 eV threshold at 82°K, which produces quenching of photocurrent only, and is due to

transitions of type I. The abrupt quenching followed by a small excitation of photocurrent in the spectral range from 0.73 to 0.77 eV corresponds to a competition between transitions of type I and II. The sharp increase of quenching at about 0.77 eV shows that transition III has become dominant. Above 0.99 eV, the fast excitation is due to transition V; above 1.13 eV, the following slow quenching is caused by transition IV. At 213°K, under our experimental condition, it is assumed that level 1 lies above its corresponding hole demarcation level, and we see the quenching process of type IV transitions after the excitation transitions of type V and type II. At 213°K, persistent quenching is absent because of the thermal instability of the trapped electrons. The evidence for the interpretations of our proposed model is summarized in Table IV-II.

The photo-Hall data also indicate that a complete model for the photoconductivity behavior probably should include the possibility of local inhomogeneity effects, i.e., optical quenching proceeds to different stages of completeness and at different rates in different regions of the crystal, due to local fluctuations in level densities.

C. PROGRESS: HIGH-RESISTIVITY GaAs:Cr

1. Materials

All samples of GaAs:Cr were grown by the sealed Czochralski technique and were purchased from Bell and Howell Co. Although the material has been doped intentionally only with Cr (3.5 ppm), it has been found by mass spectrographic analysis that 25 ppm of Al, 2.4 ppm of O, 2.0 ppm of Na, 1.4 ppm of S, 1.3 ppm of C, and 0.5 ppm of Si, etc., also exist in the same sample.

2. Experimental Results

2.1 Dark Conductivity and Hall Effect

The activation energy for the variation of dark conductivity with temperature for the As-grown GaAs:Cr sample is 0.68±0.01 eV. As in the GaAs:O sample, the Hall mobility is constant over the temperature range from 280° to 330°K and then decreases with decreasing temperature below this range. The location of the Fermi level for this sample at 300°K, calculated from the Hall coefficient, is 0.605 eV.

2.2 Photoconductivity Spectral Response

The spectral response of photoconductivity and Hall mobility are given in Fig. IV-6 for measurements at 295° and 213°K. A nonsteady-state spectral response at 82°K, measured 3 min and 15 min after photoexcitation in two different ways as described above for GaAs:O, are shown in Figs. IV-7(a) and IV-7(b). Although not as pronounced as for GaAs:O, the data for GaAs:Cr again show a high-sensitivity state and a low-sensitivity state, but now both states are n-type and the photon energy range which causes the low-sensitivity state extends from 1.0 to 1.44 eV. The photoconductivity minimum at 1.1 eV at 82°K in Fig. IV-7(a) is actually dominated by hole conductivity in steady state, but is still n-type under the nonsteady-state experimental conditions described above. Intrinsic photoexcitation produces a maximum at 1.42 eV at 295°K, 1.43 eV at 213°K, and 1.48 ± 0.03 eV at 82°K; extrinsic photoexcitation produces a broad maximum at about 0.88 eV at both 295° and 213°K,which splits into two peaks (one at 0.77 and the other at 0.87 eV) at 82°K.

2.3 Photoconductivity vs Temperature

The temperature dependence of photoconductivity for intrinsic photoexcitation and the associated photo-Hall mobility are given in Figs. IV-8(a) and IV-8(b). The upper curve represents the crystal in its high-sensitivity state. The lower curve represents the variation of photoconductivity in a low-sensitivity state induced by exposure to 1.08 eV radiation for one hour at 82°K. It shows again the similarity between high-resistivity GaAs:C and GaAs:Cr; a rapid and dramatic recovery from the low-sensitivity quenched state to the high-sensitivity state occurs upon heating within the temperature range from 105° to 125°K.

2.4 Optical Quenching of Photoconductivity

Figures IV-9(a) and IV-9(b) show the optical quenching spectra for photocurrent and the related transient behavior at 295°, 213° and 82°K. At 295°K, the quenching spectrum has a low-energy threshold at about 0.72 eV and a sharp increase at 0.88 eV. Both excitation and quenching of photocurrent occur over the whole quenching spectrum range. At 213°K, the onset of optical quenching is at about 0.92 eV. Again both excitation and quenching of photocurrent are observed in all transient curves. At 82°K, quenching starts at 0.5 eV and there is no excitation after the fast quenching of photocurrent is observed. From 0.785-0.81 eV we see a small excitation, followed by quenching, and then by a large excitation of photocurrent. In this situation, we calculated the percent quenching as the ratio of the difference between the maximum excited current and minimum quenched current with the secondary radiation on, and maximum excited current. From 0.81 to 0.92 eV, both the initial small excitation and quenching effect disappear, and only a large increase of photocurrent

is observed. Above 0.92 eV, quenching after the excitation of photocurrent is observed again. Both quenching and recovery are fast, except between 1.08 and 1.3 eV, the range of the slow quenching process as found in the GaAs:O crystal.

3. Discussion

To facilitate discussion of the results, an energy-level model is proposed which consistently describes the results presented in the above section. This model is also given in Fig. IV-5. The imperfection levels identified in the GaAs:O crystal, such as levels b-f and 1-3, appear also to exist in the GaAs:Cr sample. This is not surprising since the residual impurities in the GaAs:Cr crystal, especially oxygen as determined by mass spectrographic analysis, are also present in the GaAs:O crystal.

The dark Fermi level at room temperature is at 0.605 eV below the conduction band; hence both levels 1 and B are partially occupied, and levels 2, 3 and A are completely occupied. Both the thermal-ionization energy derived from the temperature dependence of the Hall coefficient (0.68 ± 0.01 eV) and the optical ionization energy derived from the low-energy threshold for the extrinsic photoconductivity (about 0.68 eV at 295°K, 0.7 eV at 213°K, and 0.74 eV at 82°K) indicate the energy separation between level 2 and/or level A and the conduction band. Because level 2 and level A are very close to each other in energy, and because the effect of thermal fluctuations is large at high temperature, it is difficult to distinguish transitions of type II from those of type VI through the photoexcited current. Only at low temperature, are they observed separately in the spectral response of photoconductivity. As shown in Figs. IV-6 and IV-7(a), two peaks are observed in the 0.7 - 1.0 eV

region at 82°K, while there is only one peak at 295° and 213°K. The small peak at about 0.77 eV is clearer for some of the GaAs:Cr samples cut from the same ingot. Although not reported in every GaAs:Cr crystal[7,8], this small peak has also been found by other investigators.[9,10]. We believe that this small peak is due to the residual imperfections found in most of high-resistivity GaAs crystals. The long wavelength edge of the extrinsic photoconductivity spectrum corresponds to transitions from level 2 to the conduction band. The decrease of photoconductivity (Fig. IV-7(a)) and photo-Hall mobility (Fig. IV-7(b)) on the high photon energy side of the small peak can be explained in terms of a competition between transitions from the valence band to level 2 and those from level 2 to the conduction band. The dramatic increase of photoconductivity at about 0.8 eV is caused by a strong transition from level A to the conduction band (transition VI); hence the related photo-Hall mobility also increases simultaneously. The rapid decrease of photoconductivity and photo-Hall mobility at about 0.87 eV is due to strong excitation of electrons from the valence band to level B, leaving free holes in the valence band which decrease electron lifetime and increase hole lifetime. Since this sharp peak is also found at room temperature for the GaAs:Cr crystal but not for the GaAs:O crystal, it seems that both levels A and B are related to the presence of Cr. At 295° and 213°K, the increase of photoconductivity and Hall mobility again at about 1.02 eV indicates that transitions of type I are dominant then.

All the transitions from these five imperfection centers to either conduction band or valence band can also be discerned in the optical quenching spectra of Figs. IV-9(a) and IV-9(b). At 82°K, a threshold at about 0.5 eV indicates transitions of type I. Quenching without excitation

of photocurrent occurs in the range from 0.5 to 0.7 eV. As the photon energy increases, transitions of both type I and type II occur, resulting in quenching (type I) followed by excitation (type II) of photocurrent in the 0.73-0.78 eV region. At 0.8 eV, there is excitation (type II) followed by quenching (type III; type I and VII transitions can be neglected) and then an excitation (type VI) of photocurrent. In the range from 0.82 to 0.92 eV, transitions of type VI actually dominate all others. From 0.92 to 1.08 eV, we find first excitation (type VI) and then quenching (type VIII) of photocurrent. At about 1.08 eV, there is again a slow quenching (type IV) as for the GaAs:O crystal, after a fast excitation (types VI and V) and a fast quenching (type VIII) of photocurrent. The quenching spectrum at room temperature (which is not observed in the GaAs:O crystal under the same experimental condition) also shows the existence of level A (from the onset of the quenching spectrum at about 0.72 eV) and level B (from the abrupt increase of quenching at about 0.88 eV). At 213°K, only the strong quenching process (type VIII) can be easily observed in Fig. IV-9(a). All the transitions observed in different measurements according to the model of the GaAs:Cr crystal are summarized in Table IV-II.

D. CONCLUSIONS

The photoelectronic properties of high-resistivity n-type GaAs:O and GaAs:Cr single crystals have been carefully investigated in detail. The results can be described consistently by a three-level model for GaAs:O and a five-level model for GaAs:Cr (the same levels as in GaAs:O, plus two others typical of Cr). A qualitative interpretation of the effects of heating and of bending GaAs:Cr has been given in a previous

report. Quantitative investigation of the electronic properties of dislocations requires purer GaAs single crystals than currently available.

REFERENCES

IV-1. H. F. Matare', Advances in Electronics, Proceed. of the XIIIth International Scientific Congress of Electronics, Rome, Italy, 1966, Vol. 1.

IV-2. H. F. Matare', Direct Current Journal (British), Vol. 6, No. 5, 1 (1961).

IV-3. C. S. Smith, Phys. Rev., 9, 42 (1954).

IV-4. E. Omelianovski, unpublished results.

IV-5. A. D. Jonath, unpublished results.

IV-6. Supplied through the kindness of Warren O. Groves.

IV-7. G. A. Allen, Brit. J. Appl. Phys., Ser. 2, 1, 593 (1968).

IV-8. N. M. Kolchanova, D. N. Nasledov, M. A. Mirdzhalilova, and V. Yu. Ibragimov, Sov. Phys.-Semicond. 4, 294 (1970).

IV-9. R. F. Broom, J. Appl. Phys. 38, 3483 (1967).

IV-10. G. P. Peka and Yu. I. Karkhanin, Sov. Phys.-Semicond. 6, 261 (1972).

TABLE IV-I

Peak Temperatures of Reported TSC Maxima for High-Resistivity GaAs, °K

Haisty[a]	Blanc, et al.[b]	Present Work on GaAs:O	Present Work on GaAs:Cr	Approximate Trap Depth From $E_t = 23\ kT_m$, eV
95		91		0.19
115	107, 111	116	116	0.23
142	131, 136	133	138	0.28
160	156,160,162, 166,168	160	158	0.31
193		190	189	0.38
208		203	212	0.42

[a] On "undoped semi-insulating" GaAs. R. W. Haisty, Appl. Phys. Letters, 10, 31 (1967).

[b] On high-resistivity Cu-diffused GaAs. J. Blanc, R. H. Bube and H. E. MacDonald, J. Appl. Phys. 32, 1666 (1961).

TABLE IV-II

Types of Evidence for Imperfection Levels in High-resistivity GaAs:O and GaAs:Cr by Photoconductivity Measurements, eV

(Number in parentheses indicates transition according to model of Figure IV-5)

Material	Level	TSC	Spectral Response			Optical Quenching Spectra		
			295°K	213°K	82°K	295°K	213°K	82°K
GaAs:O	a,b,c	0.19,0.23,0.28						
	d,e,f,	0.31,0.38,0.42						
	1							
	2		0.68(II)	0.68(II)	0.74(II)		1.0(IV)	1.03(IV)
	3		1.0(V)	1.0(V)				0.77(III)
								0.5(I)
GaAs:Cr	b,c	0.23,0.28,						
	d,e,f	0.31,0.38,042						
	1							
	2		0.68(II)	0.7(II)	0.74(II), 0.77(III)			1.08(IV)
	3		1.02(V)	1.02(V)				0.5(I)
	A				0.8(VI)	0.72(VII)		0.8(VI)
	B		0.88(VIII)	0.88(VIII)	0.87(VIII)	0.88(VIII)	0.92(VIII)	0.92(VIII)

FIGURE CAPTIONS

Figure IV-1 Photoconductivity spectral response and variation of photo-Hall mobility with photon energy at 295° and 213°K for GaAs:O crystal.

Figure IV-2(a) Photoconductivity spectral response curves at 82°K for GaAs:O crystal: measured from high to low photon energies, reading after 3 min (o), and after 15 min (Δ); measured from low to high photon energies, reading after 3 min (●), and after 15 min (▲).

Figure IV-2(b) Photo-Hall mobility vs. photon energy for GaAs:O crystal at 82°K: measured from high to low photon energies, reading after 3 min (o), and after 15 min (Δ); measured from low to high photon energies, reading after 3 min (●), and after 15 min (▲).

Figure IV-3(a) Temperature dependence of photoconductivity for GaAs:O crystal, for intrinsic photoexcitation (Δ); for intrinsic photoexcitation after quenching 1 hr with 1.08 eV (o) or 1.18 eV (□) at 82°K, measured while warming; and for simultaneous intrinsic and extrinsic (1.18 eV) photo-excited (▽).

Figure IV-3(b) Temperature dependence of photo-Hall mobility in GaAs:O crystal, for intrinsic photoexcitation (Δ); for intrinsic photoexcitation after quenching 1 hr with 1.08 eV (o) or 1.18 eV (□) at 82°K, measured while warming, corresponding to curves of Fig. IV-3(a); and for simultaneous intrinsic and extrinsic (1.18 eV) photoexcitation (▽).

Figure IV-4(a) Optical quenching spectra for GaAs:O crystal at 213°K and at 82°K.

Figure IV-4(b) Transient curves of optical quenching for various photon energies of secondary radiation for GaAs:O crystal excited by 1.48 eV primary radiation.

Figure IV-5 Proposed energy level schemes for high-resistivity GaAs:O and GaAs:Cr.

Figure IV-6 Photoconductivity spectral response and variation of photo-Hall mobility with photon energy at 295° and 213°K for GaAs:Cr crystal.

Figure IV-7(a) Photoconductivity spectral response curves at 82°K for GaAs:Cr crystal: measured from high to low photon energies, reading after 3 min (o), and after 15 min (Δ); measured from low to high photon energies, reading after 3 min (●), and after 15 min (▲).

Figure IV-7(b) Photo-Hall mobility vs. photon energy for GaAs:Cr crystal at 82°K: measured from high to low photon energies, reading after 3 min (o), and after 15 min (Δ); measured from low to high photon energies, reading after 3 min (•), and after 15 min (▲).

Figure IV-8(a) Temperature dependence of photoconductivity for GaAs:Cr crystal, for intrinsic photoexcitation (Δ); and for intrinsic photoexcitation after quenching with 1.08 eV photons for 1 hr at 82°K (o), measured while warming.

Figure IV-8(b) Temperature dependence of photo-Hall mobility for GaAs:Cr crystal, for intrinsic photoexcitation (Δ); and for intrinsic photoexcitation after quenching with 1.08 eV photons for 1 hr at 82°K (o), measured while warming, corresponding to curves of Figure IV-8(a).

Figure IV-9(a) Optical quenching spectra for GaAs:Cr crystal at 295°, 213° and 82°K.

Figure IV-9(b) Transient curves of optical quenching by various photon energies of secondary radiation for GaAs:Cr crystal excited by 1.48 eV primary radiation.

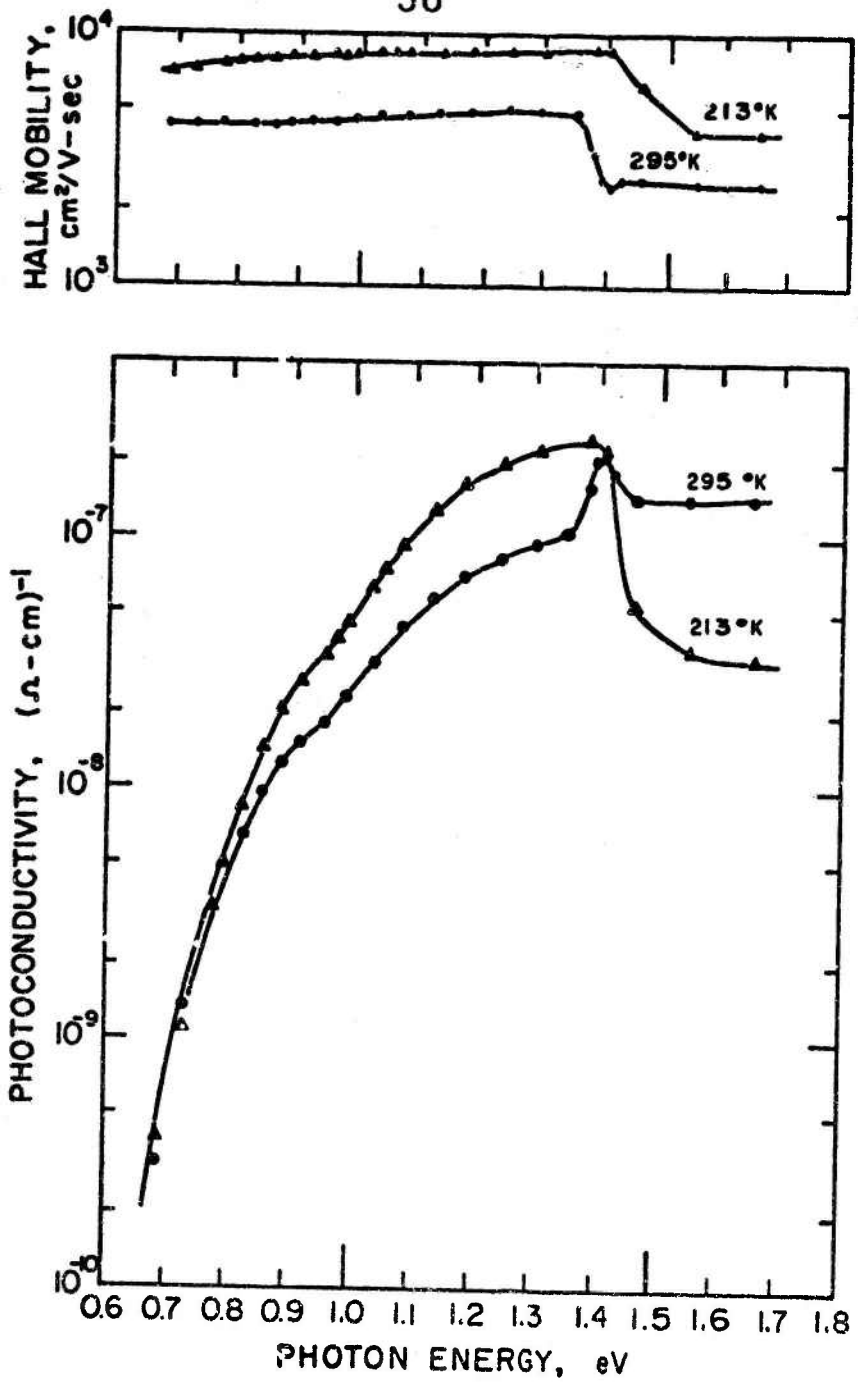

Figure IV-1 Photoconductivity spectral response and variation of photo-Hall mobility with photon energy at 295° and 213°K for GaAs:O crystal.

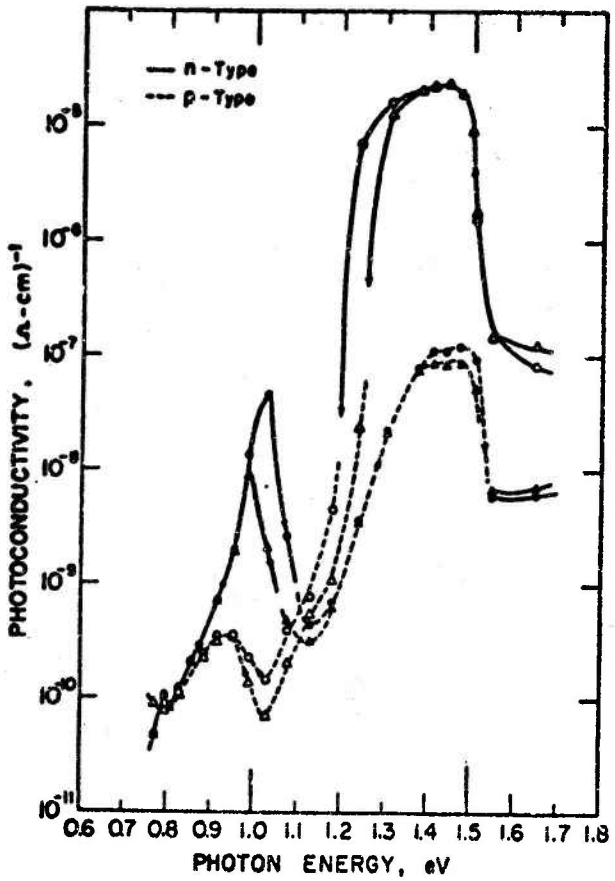

Figure IV-2(a) Photoconductivity spectral response curves at 82°K for GaAs:O crystal: measured from high to low photon energies, reading after 3 min (o), and after 15 min (Δ); measured from low to high photon energies, reading after 3 min (•), and after 15 min (▲).

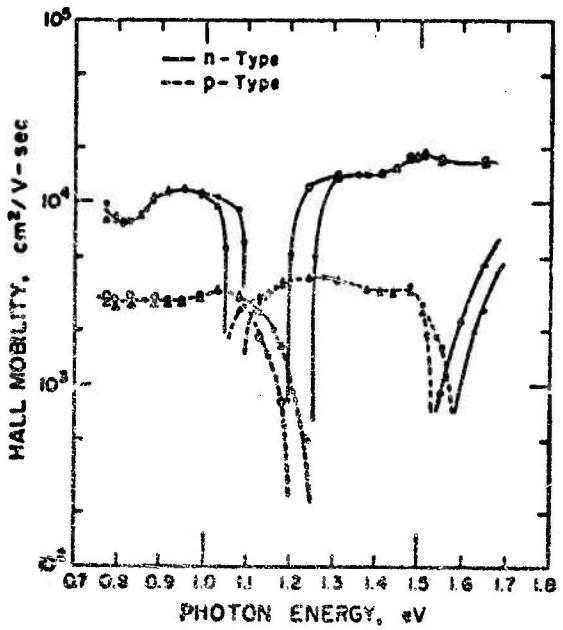

Figure IV-2(b) Photo-Hall mobility vs. photon energy for GaAs:O crystal at 82°K: measured from high to low photon energies, reading after 3 min (o), and after 15 min (Δ); measured from low to high photon energies, reading after 3 min (•), and after 15 min (▲).

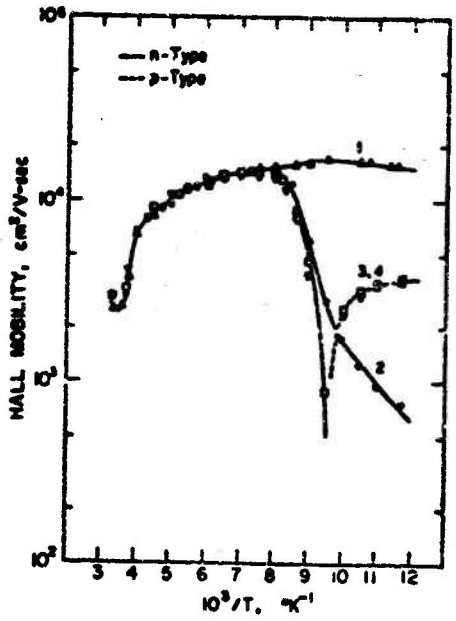

Figure IV-3(a) Temperature dependence of photoconductivity for GaAs:O crystal, for intrinsic photoexcitation (Δ); for intrinsic photoexcitation after quenching 1 hr with 1.08 eV (o) or 1.18 eV (□) at 82°K, measured while warming; and for simultaneous intrinsic and extrinsic (1.18 eV) photoexcited (▽).

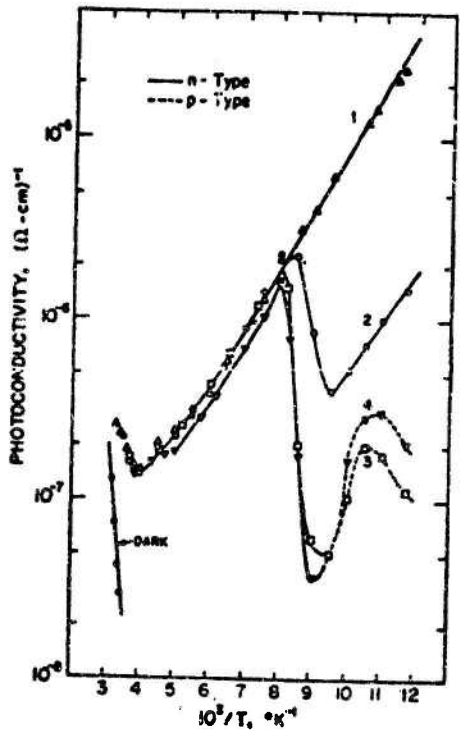

Figure IV-3(b) Temperature dependence of photo-Hall mobility in GaAs:O crystal, for intrinsic photoexcitation (Δ); for intrinsic photoexcitation after quenching 1 hr with 1.08 eV (o) or 1.18 eV (□) at 82°K, measured while warming, corresponding to curves of Fig. IV-3(a); and for simultaneous intrinsic and extrinsic (1.18 eV) photoexcitation (▽).

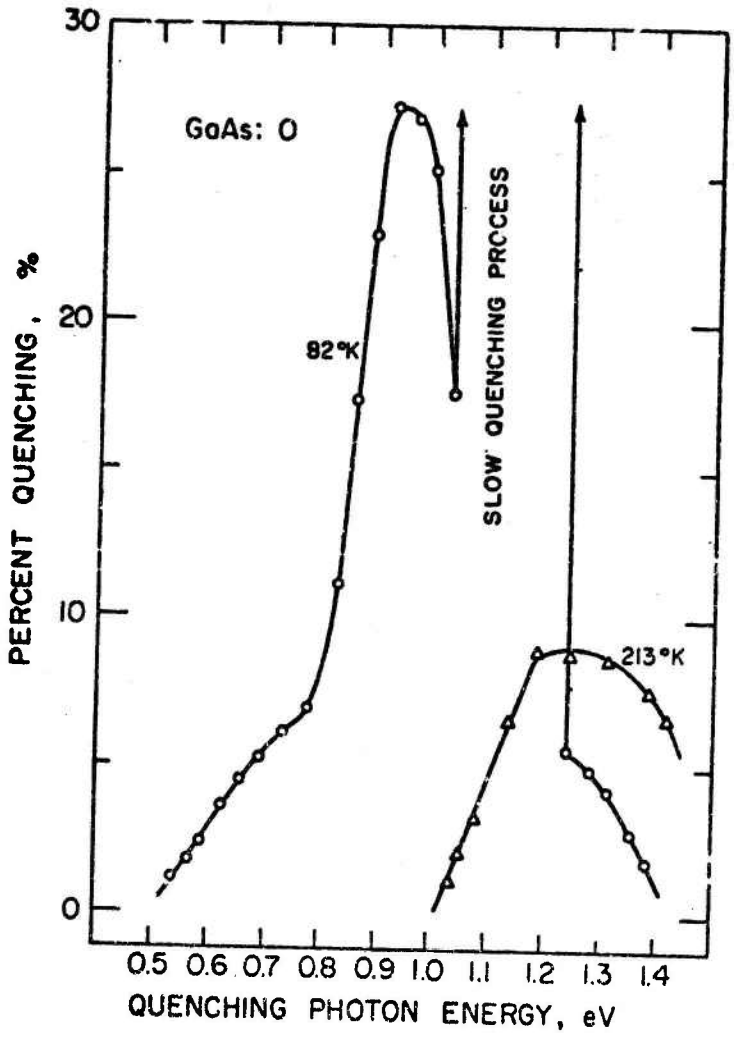

Figure IV-4(a) Optical quenching spectra for GaAs:O crystal at 213°K and at 82°K.

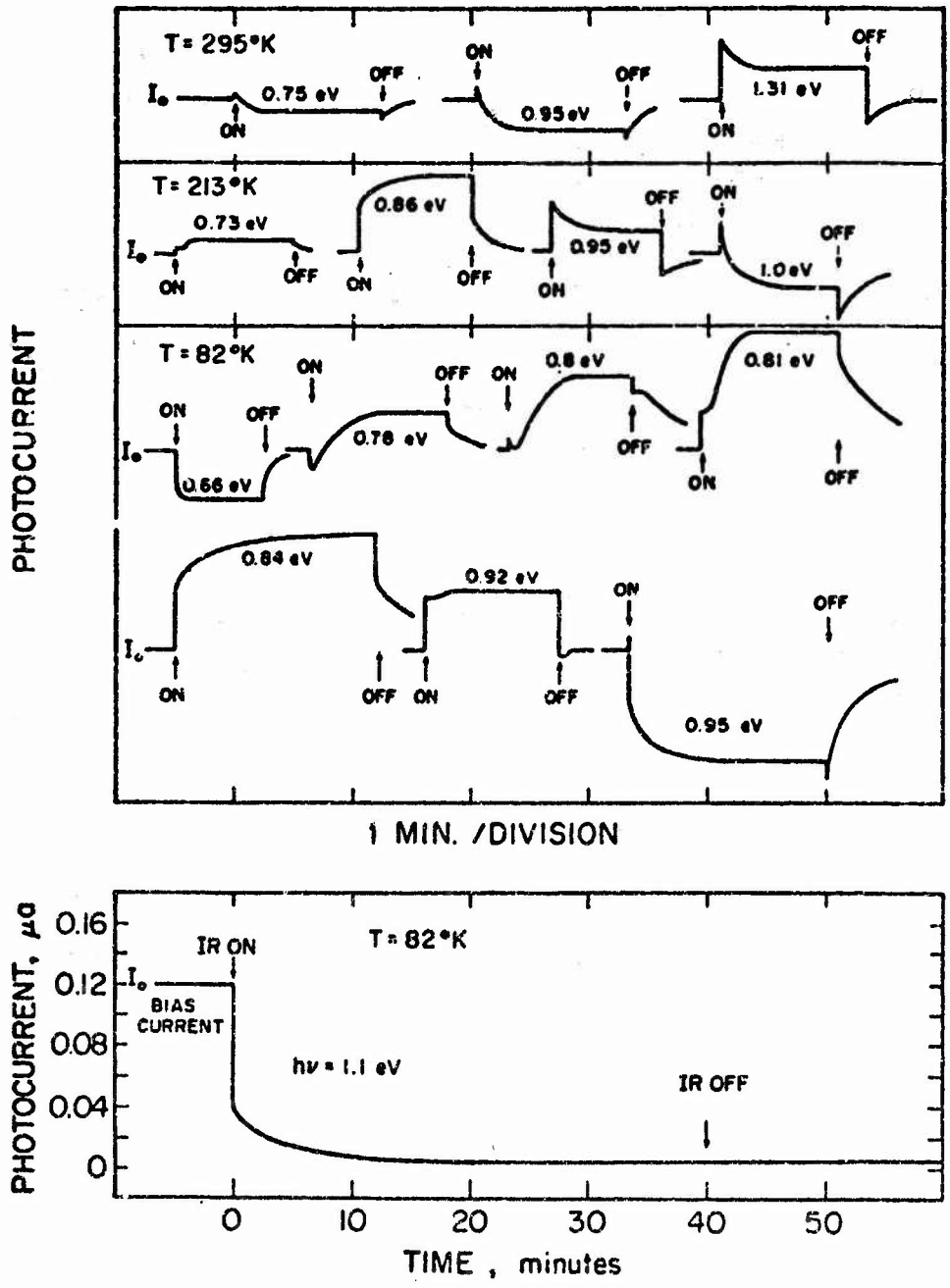

Figure IV-4(b) Transient curves of optical quenching for various photon energies of secondary radiation for GaAs:O crystal excited by 1.48 eV primary radiation.

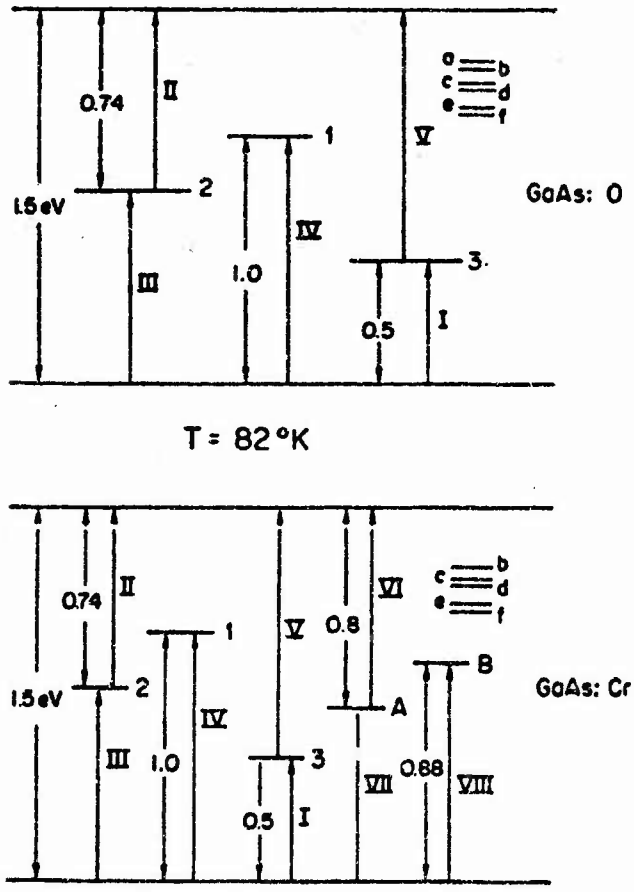

Figure IV-5 Proposed energy level schemes for high-resistivity GaAs:O and GaAs:Cr.

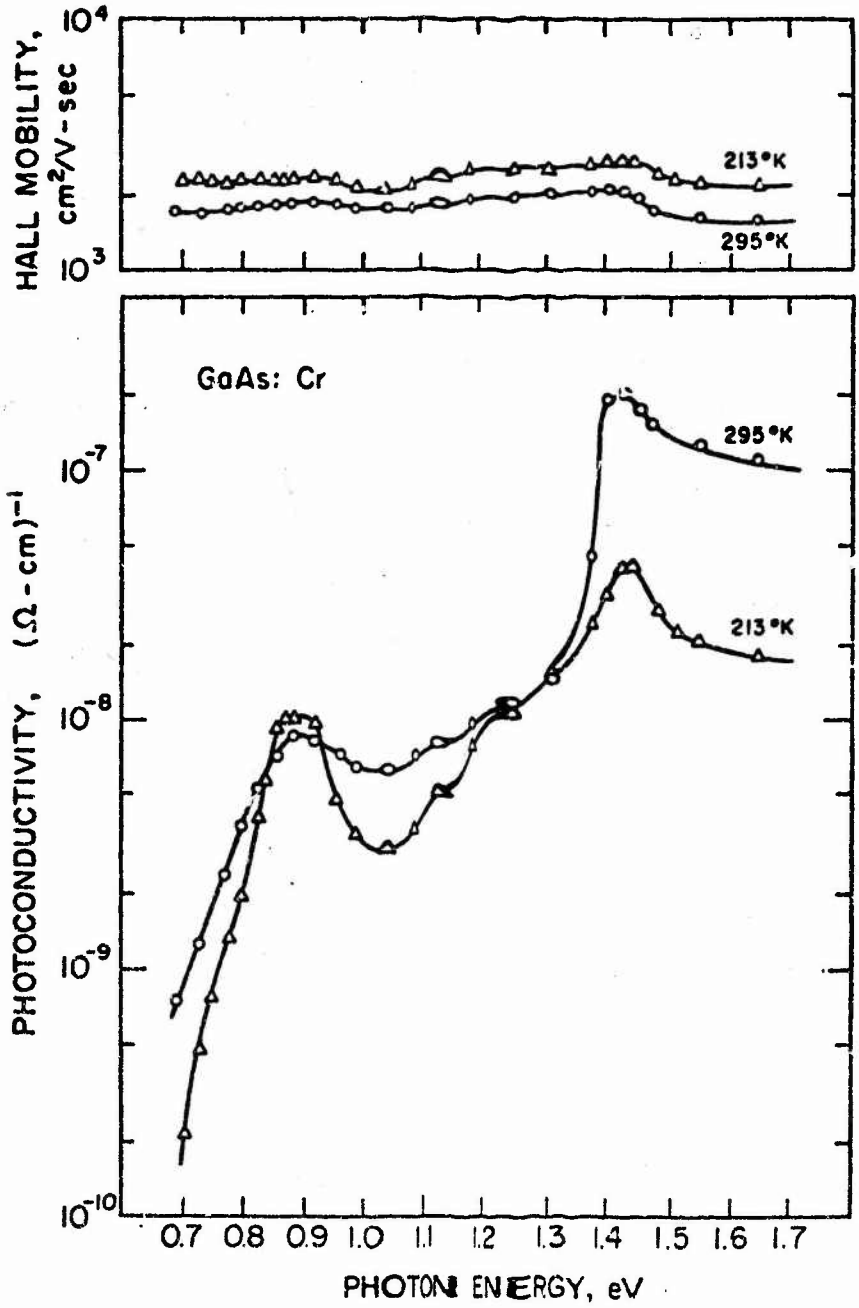

Figure IV-6 Photoconductivity spectral response and variation of photo-Hall mobility with photon energy at 295° and 213°K for GaAs:Cr crystal.

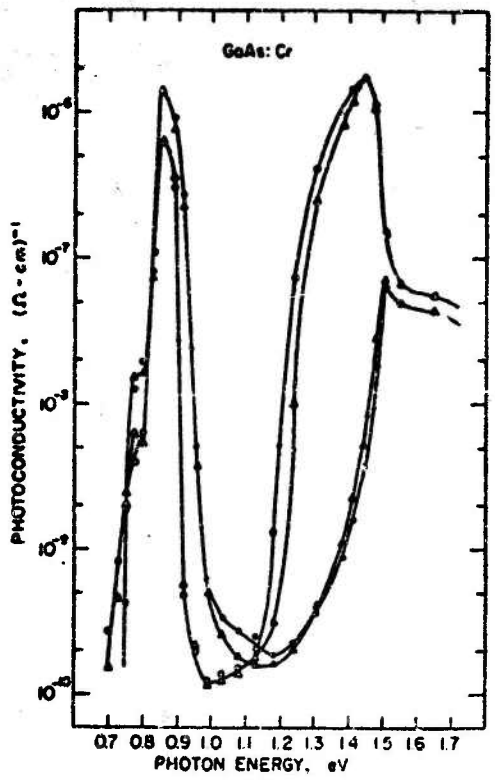

Figure IV-7(a) Photoconductivity spectral response curves at 82°K for GaAs:Cr crystal: measured from high to low photon energies, reading after 3 min (o), and after 15 min (Δ); measured from low to high photon energies, reading after 3 min (•), and after 15 min (▲).

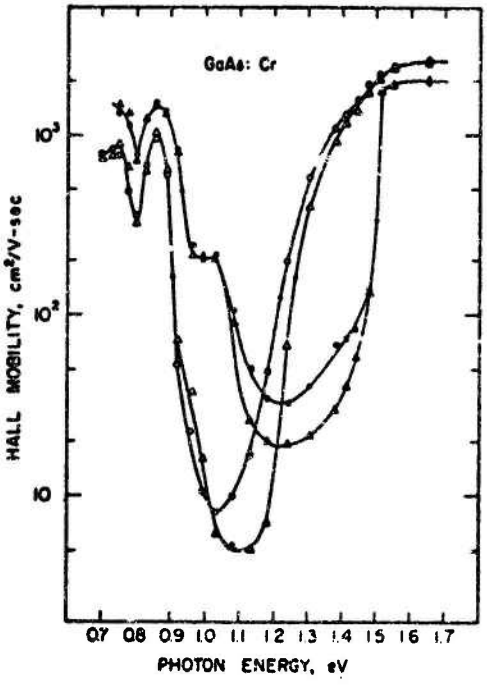

Figure IV-7(b) Photo-Hall mobility vs. photon energy for GaAs:Cr crystal at 82°K: measured from high to low photon energies, reading after 3 min (o), and after 15 min (Δ); measured from low to high photon energies, reading after 3 min (•), and after 15 min (▲).

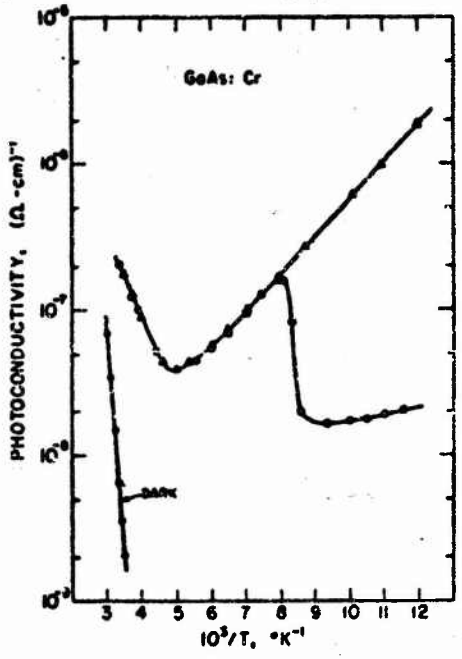

Figure IV-8(a) Temperature dependence of photoconductivity for GaAs:Cr crystal, for intrinsic photoexcitation (Δ); and for intrinsic photoexcitation after quenching with 1.08 eV photons for 1 hr at 82°K (o), measured while warming.

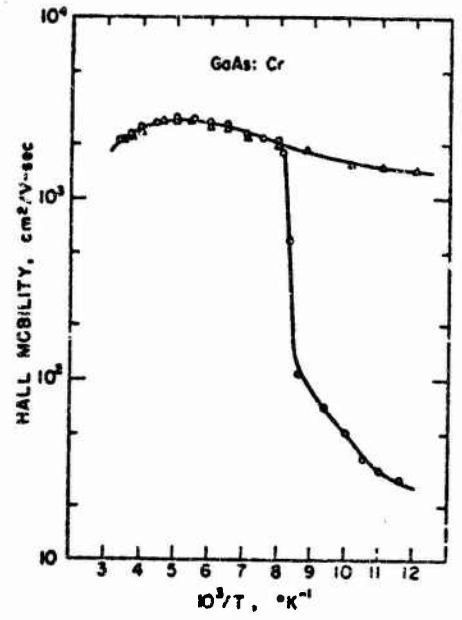

Figure IV-8(b) Temperature dependence of photo-Hall mobility for GaAs:Cr crystal, for intrinsic photoexcitation (Δ); and for intrinsic photoexcitation after quenching with 1.08 eV photons for 1 hr at 82°K (o), measured while warming, corresponding to curves of Figure IV-8(a).

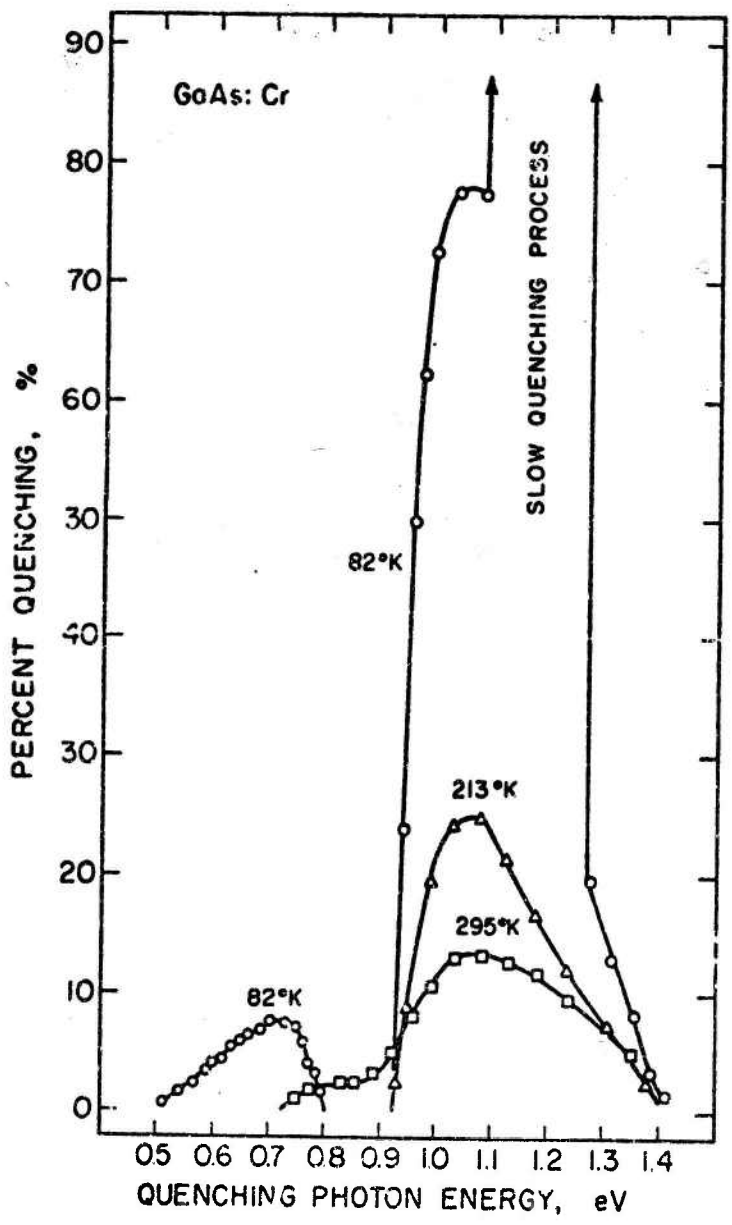

Figure IV-9(a) Optical quenching spectra for GaAs:Cr crystal at 295°, 213° and 82°K.

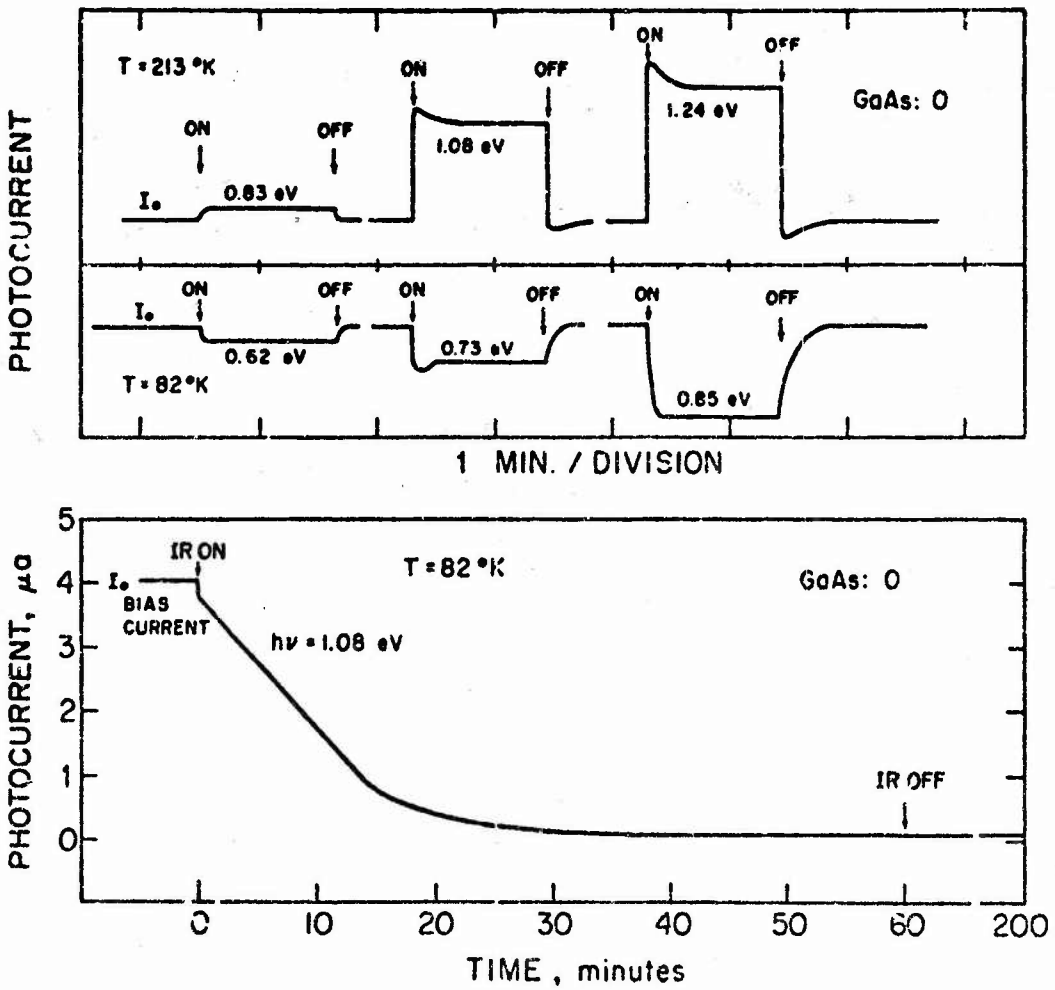

Figure IV-9(b) Transient curves of optical quenching by various photon energies of secondary radiation for GaAs:Cr crystal excited by 1.48 eV primary radiation.

V. SCIENTIFIC ASPECTS OF GALLIUM ARSENIDE CRYSTAL PREPARATION

W. A. Tiller and H. S. Kim

A. PROGRAM OBJECTIVES

The objective of this investigation was to develop an understanding of the important interfacial parameters that govern the growth of GaAs crystals. The study included both the structures and energies of the solid-liquid interfaces in the Ga-As system as a function of (i) the concentration of the liquid solution and (ii) the orientation of the GaAs crystal.

B. PROGRESS TO DATE AND PRESENT STATUS

The previous studies included the following: (i) Methods of evaluation of energetics associated with the formation of the solid-liquid interfaces have been developed by utilizing a recent atomistic treatment of interfaces. (ii) Atomic interaction energy functions have been formulated by using a parametric method. In the first period, single but rough functions were obtained by a simple parametric method. Later, more suitable functions were formulated by a modified parametric method by applying the nonlinear least squares method with newer additional data. Thermodynamic analysis of the Ga-As liquid solution has been performed to obtain better energy values for the solution. (iii) The basic energy contributions to the formation of (unrelaxed) interfaces, quasi-chemical terms, have been evaluated. It has been shown that these energy terms have large positive values and the two first layers in both phases contribute dominantly to the energy terms.

In the current period, two energetic contributions due to the two types of atomic rearrangements at the interfaces [(i) lattice relaxation

and (ii) solute atom redistribution] have been evaluated by a more refined treatment and with the more suitable interaction energy functions.

The atomic rearrangements occur due to the influence of interfacial fields and proceed in such a way that the final arrangement yields the lowest total free energy configuration. Thus, this problem can be solved by the method of minimization of total free energy for the system. The layer model of interfaces has been used for the calculation of the energetic contributions.

(1) The atomic rearrangement via variation of the concentration in the relaxing interface originates from the difference which the influence of the interfacial field has on each component of the system. At a given location relative to the interface dividing plane, one component will be more stable than the other component in the system if the energy resulting from the interaction between the interfacial field and the first component atom is more negative than that for the second component atom. Then the first component has a higher probability of spatial occupancy at that location than the second one. This type of atomic rearrangement can lower the total energy. However, the total energy includes other energy terms which could also vary with the atomic rearrangement, so the total accounting is generally much more complicated.

The total energy change associated with the phenomenon of concentration redistribution can be written as

$$\Delta G_{SR} = \Delta E_{SL} + \Delta G_{chem} \qquad (1)$$

where ΔE_{SL} = the change of interphase interaction energy and ΔG_{chem} = the chemical free energy change, which can be expressed, respectively, as

$$\Delta E_{SL} = \sum_i N_{L_i} \sum_c \left\{ X_c^F \varepsilon_{SL,c}^F - X_c^I \varepsilon_{SL,c}^I \right\}_i \qquad (2)$$

and

$$\Delta G_{chem} = \sum_i N_{L_i} \sum_c \left\{ X_c^F \mu_c^F - X_c^I \mu_c^I \right\}_i \qquad (3)$$

where N_{L_i} = number of atoms in liquid layer i per unit area, $\varepsilon_{SL,c}$ = interphase interaction energy per atom of component, c, X_c = atomic fraction of component c, μ_c = chemical potential of component c, F, I = final or initial state, i = order of liquid layers from the interface dividing plane, and c = component c (c = A or B). However, ΔG_{chem} comprises the sum of both an ideal mixing term, ΔG^{IM} and an excess energy of mixing term, ΔG^X. The former can always be calculated for a given concentration because it depends only on the concentration. However, the latter term cannot be calculated in a simple way because it is a function of activity coefficients which are usually not known for the atoms in the interface region. The activity coefficient at the interface is no longer the bulk value but is altered by the influence of the interfacial field and the nonuniform concentration distribution. But, if the excess entropy of mixing can be assumed to have a negligible change compared with other terms during the atom rearrangement, then ΔG^X mainly depends on the change of the energy of interaction, which consists of two parts; the energy interaction between layers, ΔE_{LB}, and the energy of interaction inside a layer, ΔE_{LI}. Thus, Eq. (1) can be written as

$$\Delta G_{SR} = \Delta E_{SL} + \Delta G^{IM} + \Delta E_{LB} + \Delta E_{LI} , \qquad (4)$$

which also can be written in the summation form for each layer as

$$\Delta G_{SR}(X_1,X_2,\ldots,X_i) = \sum_{i=1} \left\{ \Delta E_{SL_i}(X_i) + \Delta G_i^{IM}(X_i) + \Delta E_{LB_i}(X_i,X_i,) + \Delta E_{LI_i}(X_i) \right\} \qquad (5)$$

Now, all the interaction energy terms in Eq. (5) can be calculated because they can be expressed in terms of interatomic interaction energy functions utilizing the layer sum method. We can find the solution by minimizing ΔG_{SR} with respect to all the X_i, simultaneously. Because of the complication of the functional expressions for the energy terms in Eq. (5), this problem is best solved by numerical analysis, such as the plotting method using computer calculation.

In the calculation, we assumed that the concentration in each layer is uniform. The conservation condition and $\partial X_i/\partial r_i = 0$ for i = large number (i.e., far from the interface) are always satisfied.

ΔG_{SR} obtained are listed in Table V-1 and the energy of formation of solid-liquid interfaces, relaxed through the solute redistribution, $E_{SL}^{x'}$, is plotted in Fig. V-1 as a function of concentration (along the liquidus line). Concentration distributions after the relaxation are shown in Figs. V-2(a), V-2(b), V-2(c), V-2(d) and V-2(e).

Generally, ΔG_{SR} are large negative values so that the energy of formation of the relaxed interface, $E_{SL}^{x'}$, is much lower than that of the unrelaxed interface. The concentration distributions after the relaxation process are very similar among all the different orientation interfaces but differ depending on the initial concentrations of the liquid solution. In most cases, the first layer is fully enriched by As atoms. The second, third and fourth layers are also somewhat enriched for the

case of the initial concentration which equals 0.5 atomic fraction of As, while depletion of As concentration is shown in the second, third, and fourth layers for the cases of lower initial concentrations. There is almost no change of concentration in the further layers.

(2) At the interface region, when two semi-infinite bulk phases are joined at the dividing plane, the atomic plane parallel to the dividing plane can experience a net force in the normal direction on either side of the atomic plane due to the asymmetrical interaction field imposed by the other phase across the interface dividing plane. By changing the interlayer spacings, the force could be balanced at some proper spacings called the equilibrium spacings.

We considered only the relaxation of the first layer spacing between the two phases, d_I, because the first layers should be influenced most by the asymmetric interactions at the interface.

The total interaction energy can be expressed in cerms of interatomic interaction energy functions by the layer sum method and, therefore, it can be expressed as a function of the layer spacings.

The relaxed spacing, d_I^*, and the energy change associated with the relaxation, ΔE_{LR}, can be obtained by minimizing the total interaction energy with respect to the spacing. Because of the complexity of the energy expression, this has been solved by a similar numerical method to that used before.

The energy contribution, ΔE_{LR}, and the relaxed layer spacing, d_I^*, are given in Tables V-2 and V-3, respectively. The energy of formation of the solid-liquid interfaces, relaxed through the lattice relaxation, are plotted in Fig. V-3 as a function of the concentration along the liquidus.

The spacings of the (100)/Liquid interfaces are expanded, while contracted at the (111)/L. interfaces. On the other hand, (110)/L. interfaces have only a very small change in the spacing.

Generally, we found that $|\Delta G_{SR}| > |\Delta E_{LR}|$. The data inside parentheses in Tables V-2 and V-3 and the dotted lines in Fig. V-2 are values calculated under the restrictions that the first layer spacing should not be smaller than the layer spacing in the solid.

C. CONCLUSIONS

The three contributions to the formation of the solid-liquid interfaces of the Ga-As system, which we investigated, are as follows: (i) The quasi-chemical contributions, the formation energy of the unrelaxed interfaces of our system in various orientations and concentrations, are large positive values. The orientation dependence of the terms appeared as (111B)/L. < (111A)/L. < (110)/L. < (100)/L. for all concentrations of the liquid solution. The dependence seems to result mainly from the influence of the orientation dependence of the solid-solid interaction energies. (ii) The contributions of two atomic rearrangements calculated independently are negative values. The concentration of the solute redistribution is generally larger in magnitude than that of the lattice relaxation.

The final solute distributions closely resemble one another for the different orientation interfaces, but the distributions show some dependence on the initial concentration of the liquid solution. In all the cases, the first layer of the liquid solution is strongly enriched with As atoms. The solute redistribution in the first layer dominates the contribution, ΔG_{SR}. The monolayer theory seems to be approximately

valid in this case. The strong As enrichment might suggest that the As atom is "interface active" in the system.

The variation of the layer spacing between two phases, due to the lattice relaxation, is nearly independent of the initial concentration of the liquid solution, but strongly depends on the orientation; layer expansions at (100)/L. interfaces, contractions at (111)/L. interfaces, and almost no change at (110)/L. interfaces.

The orientation dependence of the overall contribution, approximated by summing those three contributions, can be shown as (111B)/L. < (111A)/L. < (110)/L. < (100)/L.

Some brief connections of some of the consequences of this study to the kinetic aspects of crystal growth are as follows:

(i) The constitutional dependence of the excess energy of the interfaces might indicate that the rate of nucleation of the solid from the liquid solution (both homogeneous and heterogeneous nucleation) would decrease with decreasing initial concentration of the liquid solution.

(ii) The strongly anisotropic nature of the excess energies would be related to the formation of facets on the growing crystal from the liquid solution.

(iii) The As enrichment at the interfaces should decrease the kinetic process of molecular attachment at the growing interfaces.

Extension of this type of study to the other orientations could provide a γ-plot for this system, which is very useful for many growth problems such as interface stability analysis, ledge height analysis and ledge dynamic problems, etc. Another extension of this study to the system with a third element as impurity could develop an understanding

of the impurity adsorption or trapping at interfaces.

The method of this study is also very useful for a study of the wetability of two given phases, which is important for heteroepitaxial layer growth.

TABLE 1

Energy Change Due to the Solute Redistribution

Liquidus		$\Delta G_{SR}(erg/cm^2)$				
X_{As}	T°K	(111A)/L	(111B)/L	(110)/L	(100A)/L	(100B)/L
0.50	1511	-248	-531	-621	-682	-1584
0.20	1365	-484	-1011	-1065	-1004	-2163
0.10	1244	-550	-1253	-1313	-1274	-2703
0.05	1154	-601	-1351	-1414	-1409	-3035

TABLE 2

Energy Change Due to the Lattice Relaxation

Liquidus	$E_{LR}(erg/cm^2)$				
X_{As}	(111A)/L	(111B)/L	(110)/L	(100A)/L	(100B)/L
0.50	-266.6 (-240.9)	-638.3 (-381.5)	-38.2	-459.3	-228.0
0.20	-228.7 (-213.1)	-579.0 (-356.4)	-24.0	-529.8	-272.2
0.10	-216.5 (-202.9)	-553.2 (-340.0)	-17.4	-570.1	-314.1
0.05	-211.2 (-198.4)	-542.5 (-331.7)	-14.2	-595.4	-341.9

TABLE 3

Relaxed Layer Spacing

Liquidus X_{As}	d_I^* (Å) (111A)/L	(111B)/L	(110)/L	(100A)/L	(100B)/L
0.50	2.3930 (2.4667)	2.2756 (2.4667)	2.3760	2.4521	2.2791
0.20	2.4036 (2.4613)	2.2627 (2.4613)	2.3837	2.4628	2.2858
0.10	2.4056 (2.4596)	2.2851 (2.4596)	2.3863	2.4653	2.2883
0.05	2.4060 (2.4583)	2,2854 (2.4583)	2.3868	2.4658	2.2886

FIGURE CAPTIONS

Figure V-1 Variation of energy of formation of solid-liquid interfaces, relaxed through the solute redistribution, with the concentration along the liquidus line of the Ga-As system.

Figure V-2 (a) At the (110)/Liquid Interface. Concentration distribution in the liquid solution at the solid-liquid interface due to the relaxation process by the solute redistribution. The initial concentration of the liquid and its concentration far from the interface after redistribution are noted.

(b) At the (111A)/Liquid Interface. Concentration distribution in the liquid solution at the solid-liquid interface due to the relaxation process by the solute redistribution. The initial concentration of the liquid and its concentration far from the interface after redistribution are noted.

(c) At the (111B)/Liquid Interface. Concentration distribution in the liquid solution at the solid-liquid interface due to the relaxation process by the solute redistribution. The initial concentration of the liquid and its concentration far from the interface after redistribution are noted.

(d) At the (100A)/Liquid Interface. Concentration distribution in the liquid solution at the solid-liquid interface due to the relaxation process by the solute redistribution. The initial concentration of the liquid and its concentration far from the interface after redistribution are noted.

(e) At the (100B)/Liquid Interface. Concentration distribution in the liquid solution at the solid-liquid interface due to the relaxation process by the solute redistribution. The initial concentration of the liquid and its concentration far from the interface after redistribution are noted.

Figure V-3 Variation of energy of formation of solid-liquid interface relaxed through the lattice relaxation, with the concentration along the liquidus line of the Ga-As system.

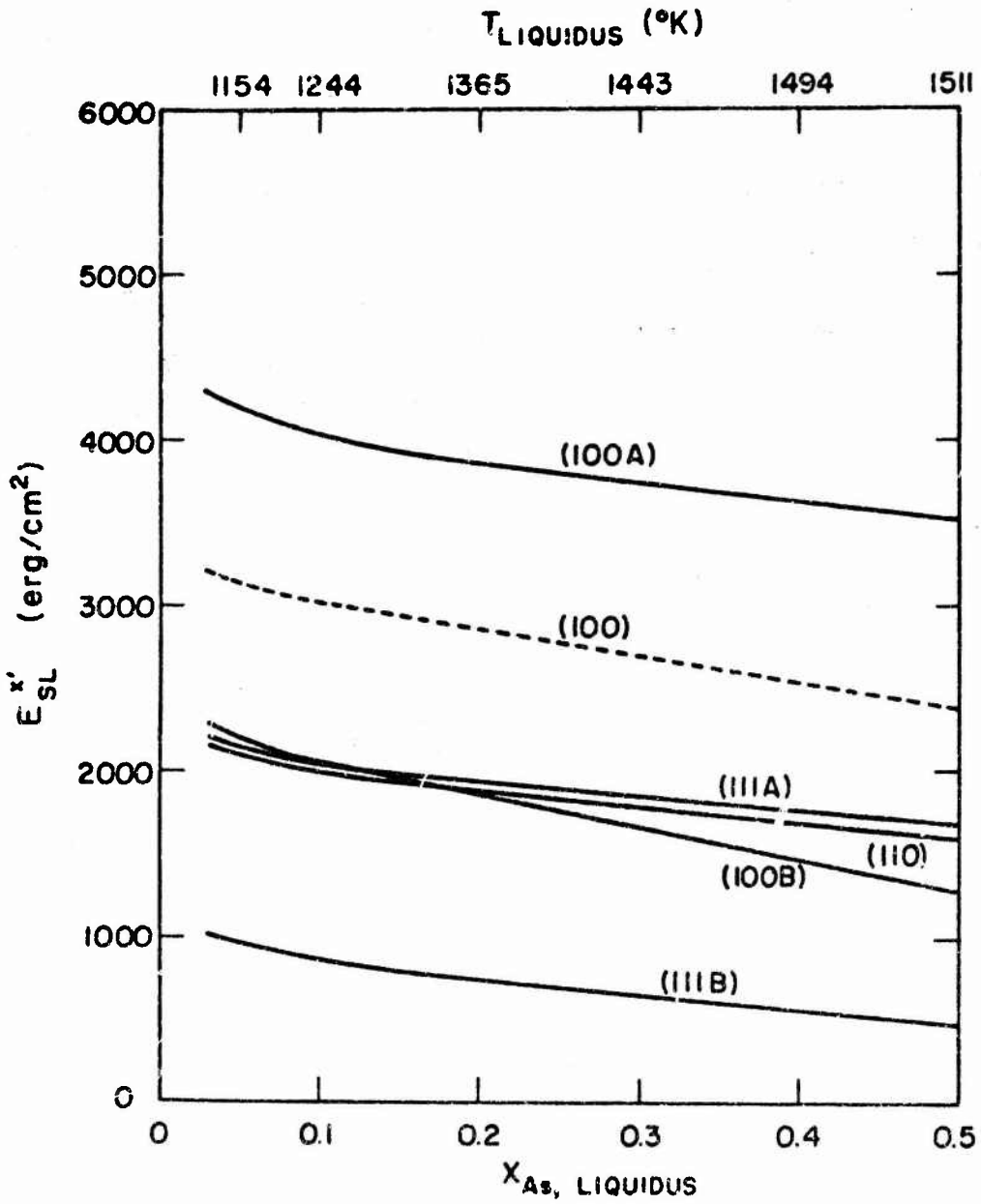

Figure V-1 Variation of energy of formation of solid-liquid interfaces, relaxed through the solute redistribution, with the concentration along the liquidus line of the Ga-As system.

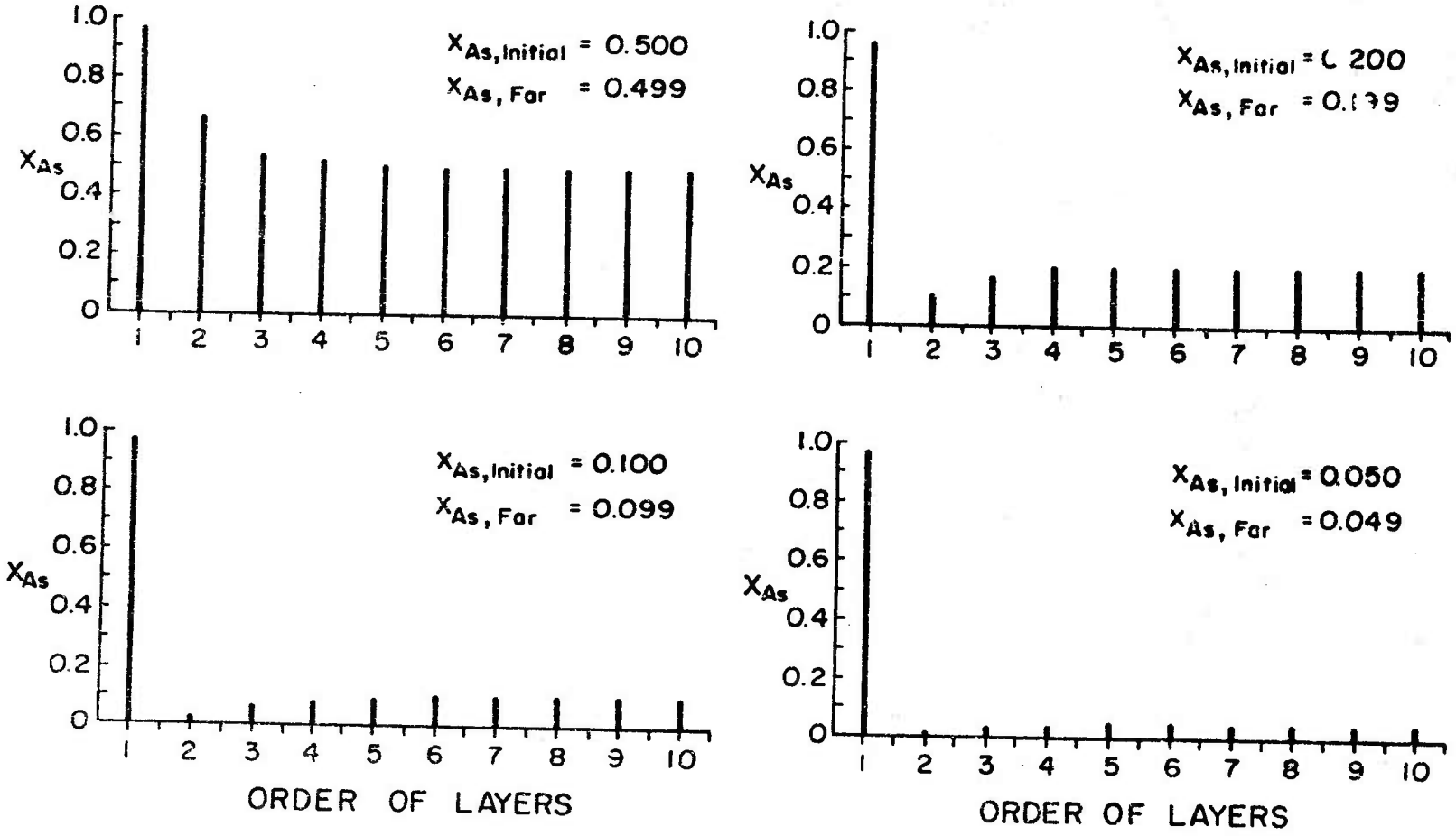

Figure V-2 (a) At the (110)/Liquid Interface. Concentration distribution in the liquid solution at the solid-liquid interface due to the relaxation process by the solute redistribution. The initial concentration of the liquid and its concentration far from the interface after redistribution are noted.

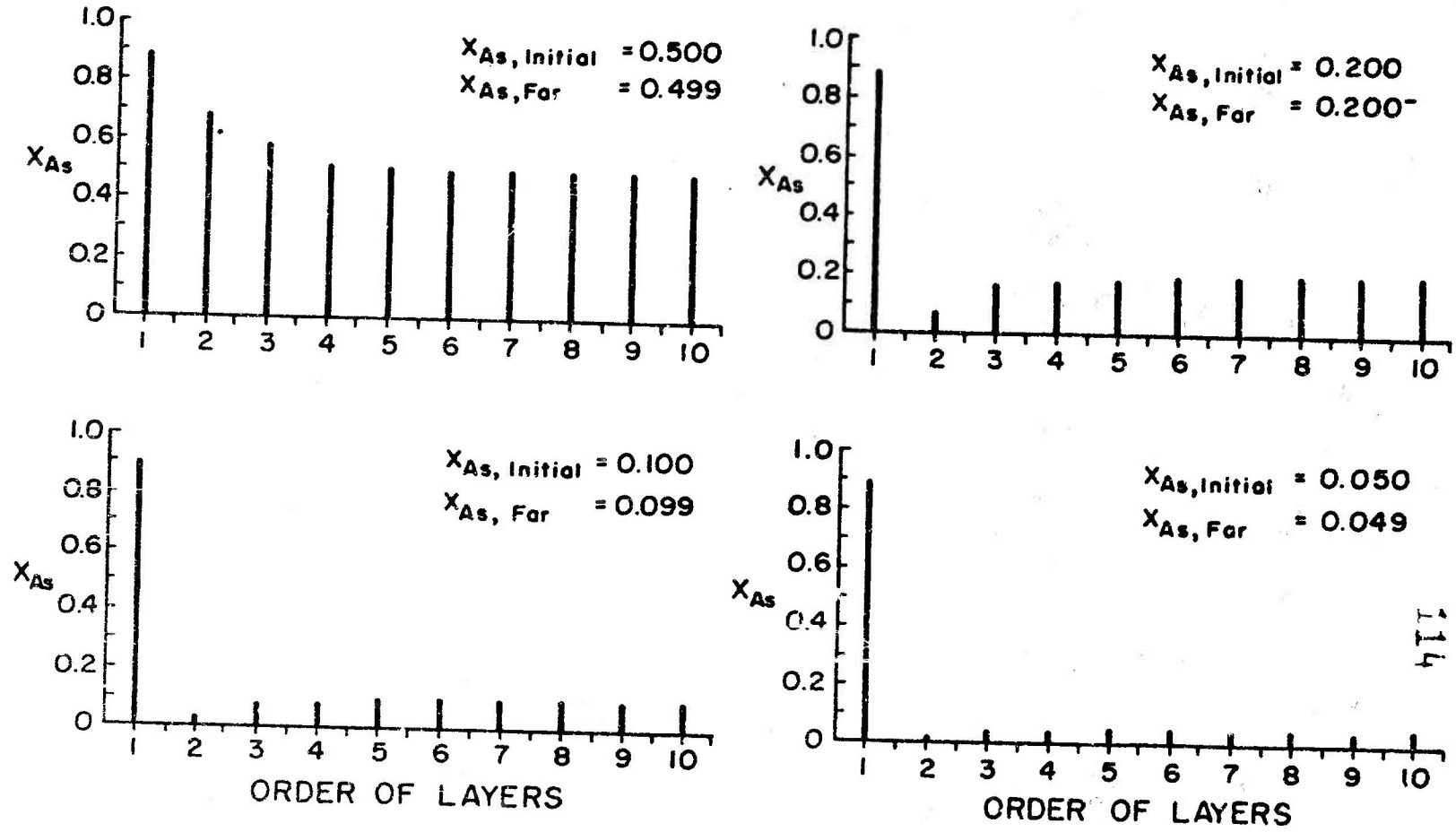

Figure V-2 (b) At the (111A)/Liquid Interface. Concentration distribution in the liquid solution at the solid-liquid interface due to the relaxation process by the solute redistribution. The initial concentration of the liquid and its concentration far from the interface after redistribution are noted.

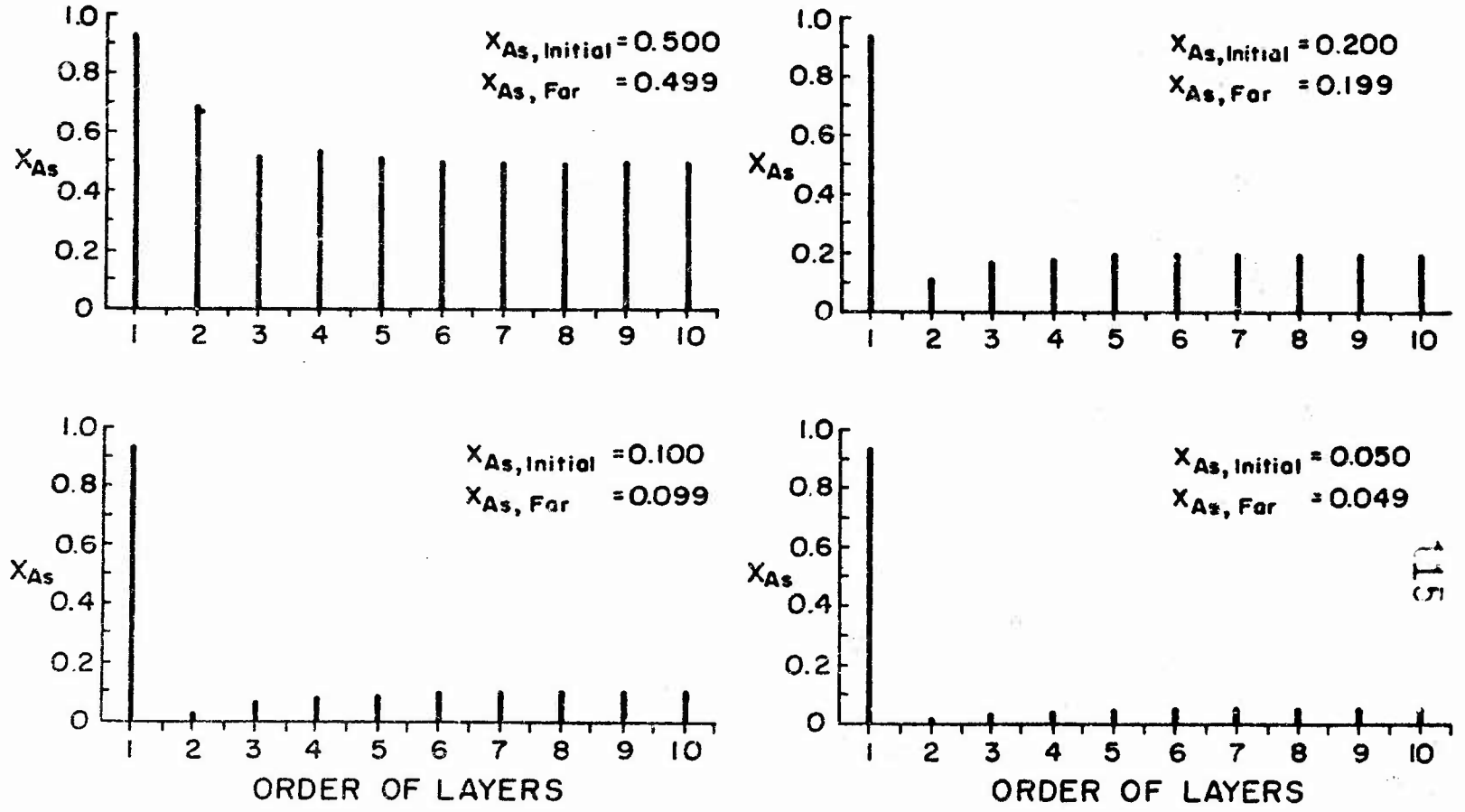

Figure V-2 (c) At the (111B)/Liquid Interface. Concentration distribution in the liquid solution at the solid-liquid interface due to the relaxation process by the solute redistribution. The initial concentration of the liquid and its concentration far from the interface after redistribution are noted.

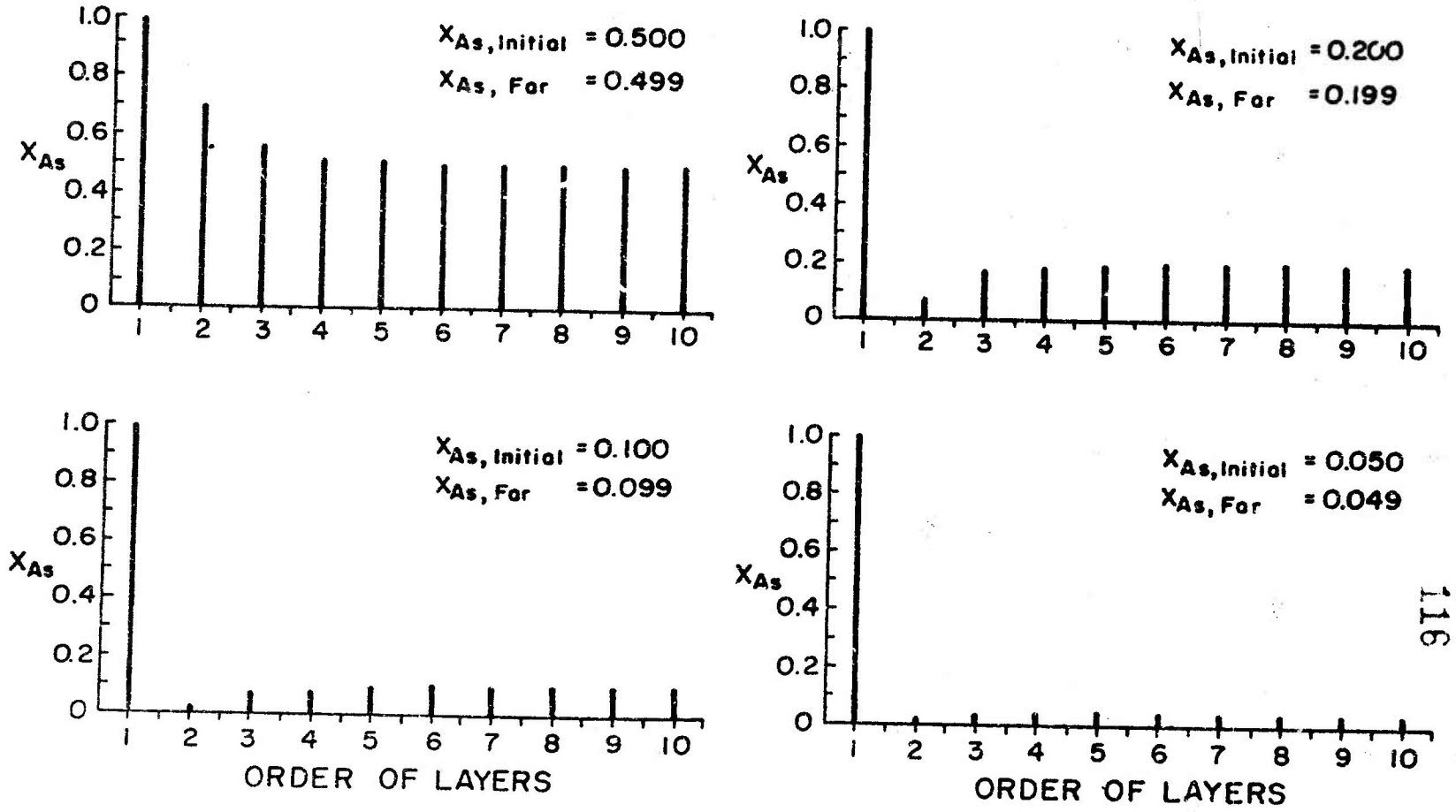

Figure V-2 (d) At the (100A)/Liquid Interface. Concentration distribution in the liquid solution at the solid-liquid interface due to the relaxation process by the solute redistribution. The initial concentration of the liquid and its concentration far from the interface after redistribution are noted.

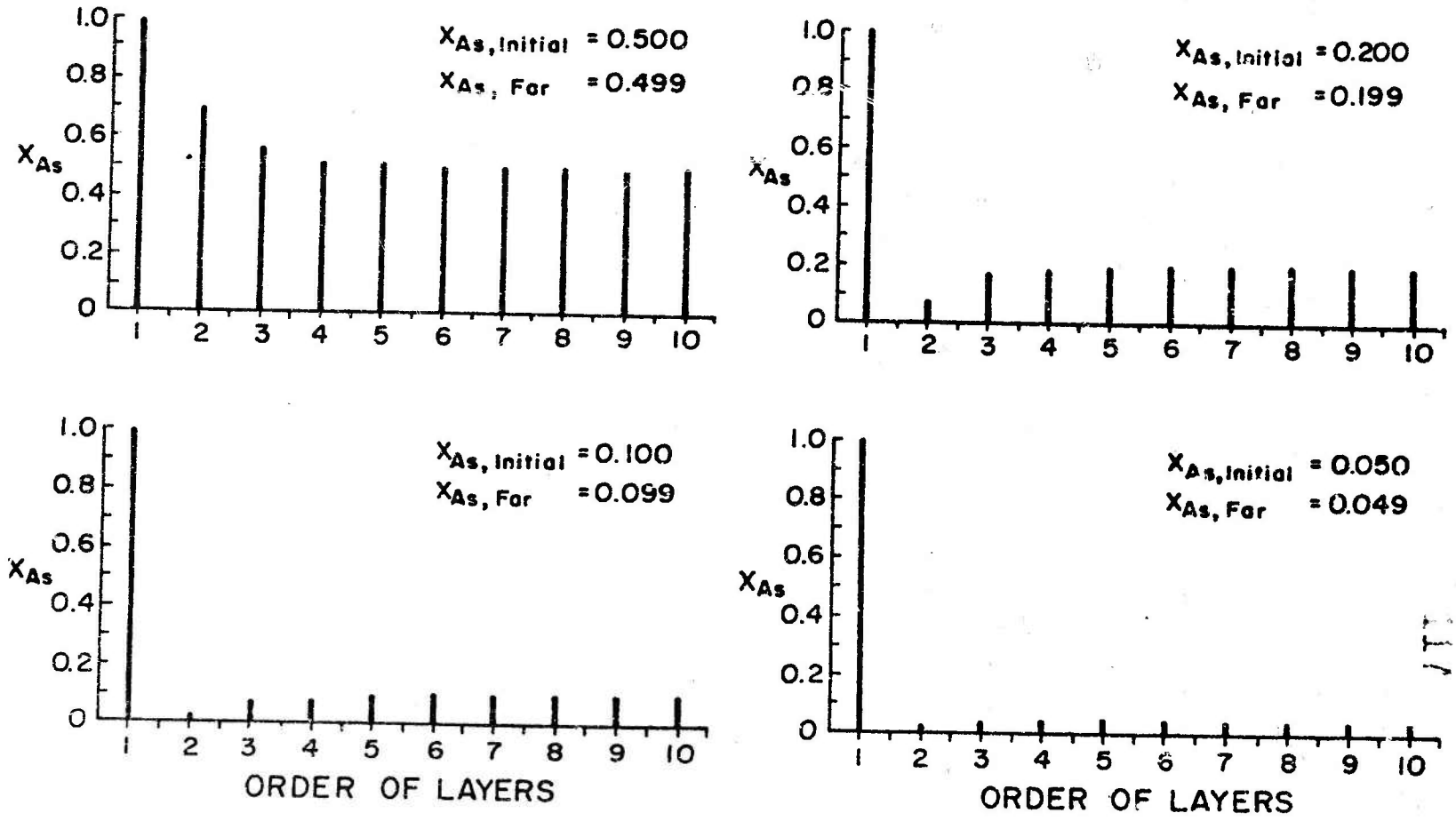

Figure V-2 (e) At the (100B)/Liquid Interface. Concentration distribution in the liquid solution at the solid-liquid interface due to the relaxation process by the solute redistribution. The initial concentration of the liquid and its concentration far from the interface after redistribution are noted.

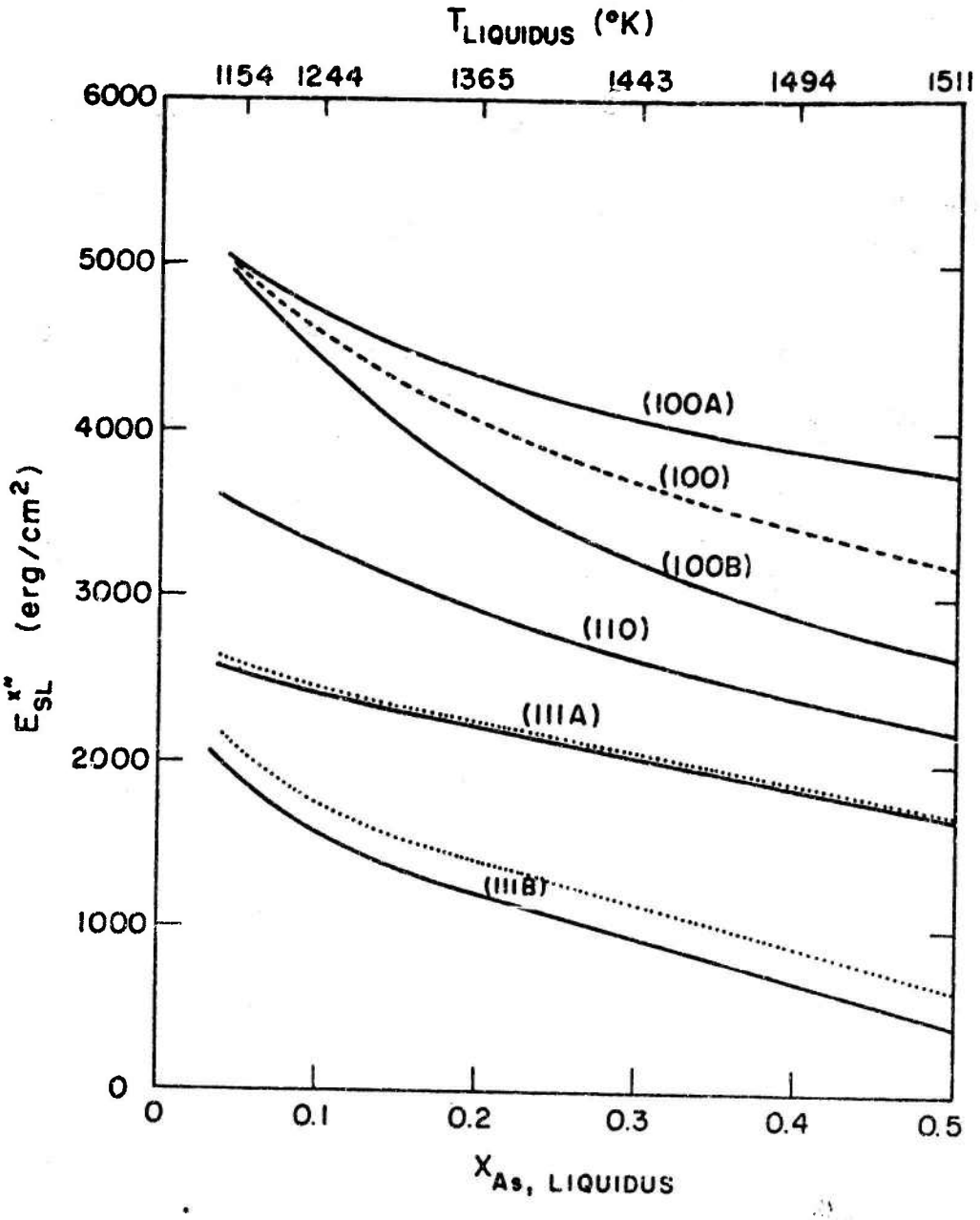

Figure V-3 Variation of energy of formation of solid-liquid interface relaxed through the lattice relaxation, with the concentration along the liquidus line of the Ga-As system.

VI. THE SYNTHESIS, CHARACTERIZATION AND DEVICE APPLICATION OF GALLIUM NITRIDE: PREPARATION OF GaN LIGHT-EMITTING DIODES

D. A. Stevenson, H. P. Maruska and W. L. Larson

A. PROGRAM OBJECTIVE AND APPROACH

In the quest for optoelectronic devices operating in the higher energy spectrum (the visible green to the ultraviolet), semiconducting materials with larger band gaps (>2.2 eV) are under study. Recently, Gallium Nitride (GaN) has attracted attention because of its possible application to electroluminescent devices emitting radiation in this spectral range. The objective of this program is to study the growth of films of GaN and to study the characteristics of these films as a function of their growth parameters. In addition, junction structures are fabricated and evaluated for their application as light emitting devices.

Gallium Nitride is a III-V compound with a band gap of 3.4 eV. The compound may not be synthesized by direct reaction of the elements even at fairly high temperatures (~2000°C), because it spontaneously decomposes into the component elements. As a consequence, techniques for its synthesis employ the reaction of a source of Ga with a source of nitrogen having a high thermodynamic activity of nitrogen (such as ammonia, or elemental nitrogen synthesized from an electric discharge). The former reactant, with GaCl(G), is used in the present study employing a vapor growth technique, in accord with the reaction below:

$$GaCl(G) + NH_3(G) = GaN(S) + HCl(G) + H_2(G)$$

Undoped GaN always occurs highly n-type ($n > 10^{18}$ cm^{-3}) and, thus far, has not been made conducting p-type. However, deep acceptors may

be used to compensate the donors and produce insulating (i) crystals. It is found that diffusion processes are not practical for incorporating dopants into GaN. For the present study, a provision is made for introducing dopants during the synthesis and growth of GaN layers. Major interest has been focused on the dopant Mg, because of its application to the fabrication of i-n junction devices showing electroluminescence in the violet portion of the spectrum.

To date, the most efficient electroluminescent devices have been made from p-n junctions. These junctions, however, have been successfully synthesized only from semiconductors with lower gaps (<2.2 eV) and are consequently limited in the lower portion of the visible spectrum. In the present case of GaN, p-type material has not been produced. Another type of electroluminescent device, much less investigated with respect to its fabrication and theory of operation, is a metal, insulator, n-type (m-i-n) junction device. The fabrication and evaluation of such a device using GaN is the major area of interest in the present investigation.

B. PROGRESS

Devices have been synthesized using the structure, sapphire substrate GaN (undoped n-type, $> 10^{18}$ cm^{-3}) GaN:Mg (insulating). Metal contacts are made to the two regions to form a junction device.

Electroluminescence was obtained both with "forward" (i layer biased positive) and "reverse" bias, although the forward-bias luminescence was more efficient. In the forward direction, substantial conduction began at about 10V, and violet light, readily seen in a well-lit room, was obtained at 20V. Under reverse bias, conduction occurred in the 40-

to 60-V range and produced green light. Emission under forward-bias electroluminescence peaked in the region 2.86--2.98 eV in various samples. The spectral width at half-maximum is about 400 meV. The peak has been found to shift to shorter wavelengths with increasing voltage until a saturation value is reached. The light output increases superlinearly with voltage, but linearly with power input. In reverse bias, a broad peak centered at 2.5 eV and about 750 meV wide at half-maximum is obtained.

The current drawn by a particular sample is dependent on the contact area, but since the emitted light shows a very nonuniform pattern, it is not possible to ascertain the density. With forward bias, $I \propto V^3$ in the region $10 < V < 30V$ where the light is emitted. A steeper dependence is found at smaller voltages. At a given voltage, the reverse current is about two orders of magnitude smaller.

The power efficiency increases with increased forward-bias up to 15V, beyond which it is nearly constant at a value of 10^{-5}. The reverse-bias efficiency is an order of magnitude lower. The diodes operate continuously at room temperature.

Photoluminescence of Mg-doped GaN was excited with a He-Cd laser which emits at 3250Å, and the resulting spectrum was found to peak at 2.925 eV at 77°K and does not shift with temperature. This indicates that the Mg complex forms a level about 0.5 eV above the valence band in GaN. In the case of Zn in GaN, it has been suggested that Zn first forms a shallow acceptor level when present in small quantities and with increased doping results in a deep Zn-donor complex, which compensates the native donors present and is responsible then for the resistivity increase and sample color changes which are observed. It is reasonable to assume

that the same process holds for Mg doping. The forward-bias electroluminescence corresponds well to the photoluminescence data, and the same level is apparently involved.

The foregoing results show that it is possible to obtain electroluminescence in Mg-doped GaN diodes which require about 20V for operation and which can emit at shorter wavelengths than Zn-doped GaN diodes. The luminescence is readily seen in a well-lit room, in spite of the eye's decreased sensitivity in the violet region of the spectrum.

This research is being continued in an effort to further elucidate the mechanisms responsible for the light generation and to learn more about the properties of the magnesium center.